

Dark-technicolour at colliders

Gauhar Abbas^{a1}, Vartika Singh^{a2}, Neelam Singh^{a3}

^a Department of Physics, Indian Institute of Technology (BHU), Varanasi 221005, India

Abstract

By employing the extended most attractive channel hypothesis, we show that QCD-like gauge dynamics is possible in the dark-technicolour paradigm. The dark-technicolour paradigm can produce the mass of the Higgs boson, and at the same time, the S -parameter is also satisfied. Moreover, the dark-technicolour paradigm can provide a solution of the flavour problem by accommodating the standard HVM or the Froggatt-Nielsen mechanism within its framework. We present the inclusive collider signatures, such as $t\bar{t}$ and $\gamma\gamma$, of the lowest lying scalars and pseudoscalars of the dark-technicolour paradigm, for the scenarios, when the standard HVM or the Froggatt-Nielsen mechanism are implemented within its framework. The collider signatures are investigated at the high-luminosity Large Hadron Collider, the high-energy Large Hadron Collider, and a 100 TeV future hadron collider. Several signatures are within the reach of the high-luminosity Large Hadron Collider. Additionally, one of the dark-Higgs of the model can address 95.4 GeV excess reported by the ATLAS and CMS experiments. Furthermore, one of the dark-Higgs can act like a new class of chirality-dependent dark-matter particles.

arXiv:2504.21593v1 [hep-ph] 30 Apr 2025

¹email: gauhar.phy@iitbhu.ac.in

²email: vartikasinh.rs.phy19@itbhu.ac.in

³email: neelamsingh.rs.phy19@itbhu.ac.in

1 Introduction

The origin of mass is one of the most fundamental questions that emerged during scientific evolution. This question is addressed through the celebrated Higgs mechanism in the Standard Model (SM), where an elementary-order parameter born out of a Higgs doublet is the source of all masses. However, the origin of this elementary-order parameter, called the Higgs VEV, remains obscure in the SM.

A similar scenario arises in the Ginzburg-Landau macroscopic theory of superconductivity [1], where the mysterious phenomenological order parameter is eventually accounted for by the Cooper pair condensate of a microscopic theory of Bardeen-Cooper-Schrieffer (BCS) [2, 3], formed by short-range attractive forces.

Remarkably, a similar phenomenon occurs in hadron physics where the low-energy phenomena can be well described by the Gell-Mann and Levy's (GML) σ model [4]. The underlying dynamics of the σ model is given by the Nambu and Jona-Lasinio model (NJL) [5, 6], which is an analog of the BCS theory. At the most fundamental level, the origin of the NJL model lies in QCD where the GML's order parameter $\langle\sigma\rangle = f_\pi = 95$ MeV turns out to be the quark-antiquark pair condensate $\bar{q}q = \mathcal{O}(f_\pi^3)$ formed by the short-range colour force, and is analogous to the Cooper pair condensate. This is a prime example of dynamical symmetry breaking originating through a local composite order parameter.

Thus, nature repeats the idea of breaking symmetry through the local composite order parameter from low to higher energies in complex scenarios such as superconductivity and hadron physics. Therefore, there is no reason to believe that we may not find its repetition again at higher energies. Hence, this may be a possible direction that may lead to the physics beyond the SM.

Technicolour (TC) models are such scenarios in which electroweak symmetry breaking can emerge naturally from dynamical symmetry breaking [7, 8]. For a review of TC models, see [9]. In addition to providing an elegant origin of the electroweak symmetry breaking, TC dynamics can also address the question of naturalness in the context of scalars. If scalars are composite objects of a TC type dynamics, the radiative contribution to them is additive, and only of the order Λ_{TC} , the scale of the TC dynamics [9].

It turns out that in QCD-like TC theories, the extended technicolour (ETC) scale goes approximately 10^6 GeV due to the presence of large flavour-changing neutral currents (FCNCs) [9]. This is the root cause of the failure of TC models based on QCD-like dynamics. This can be understood by noting that in TC models, the mass of an SM fermion is given by

$$m_f \approx \frac{\Lambda_{\text{TC}}^3}{\Lambda_{\text{ETC}}^2}, \quad (1)$$

where Λ_{ETC} is the scale of extended-TC symmetry.

This cannot produce realistic fermion masses due to $\Lambda_{\text{ETC}} \geq 10^6$ GeV, thus, leading to the failure of QCD-type TC models. Moreover, QCD-like TC models are also in conflict with the electroweak precision observables. Walking TC models with non-QCD-like dynamics may provide a way out of these issues [10]-[16].

We notice that the problem of origin of the flavour, the flavour problem of the SM, is also closely associated with the origin of mass. The flavour problem arises due to the inefficiency of the SM in explaining its flavour structure and flavour mixing, including neutrino masses and mixing. For a review of the flavour problem, see [17, 18].

In this work, we investigate the so-called dark-technicolour (DTC) paradigm based on the symmetry $\mathcal{G}_{\text{DTC}} \equiv \text{SU}(N_{\text{TC}}) \times \text{SU}(N_{\text{DTC}}) \times \text{SU}(N_{\text{D}})$ [19], where TC represents technicolour, DTC denotes dark-technicolour, and D represents dark-QCD (DQCD). The main feature of the DTC paradigm is that it does not deviate from QCD-like behaviour. This is achieved by disentangling the problem of fermion masses and the problem of large FCNCs. In the DTC paradigm, we keep the ETC scale high of the order 10^6 GeV, and fermionic masses and mixing, including that of leptons, arise from the DTC dynamics [19]. Moreover, we shall show that the DTC paradigm can produce the mass of the SM Higgs boson by exploiting the extended-most-attractive channel hypothesis (EMAC) [20, 21, 22]. Furthermore, again using the EMAC hypothesis, we shall show that the DTC paradigm is compatible with the electroweak precision observables.

One of the possible low-energy effective limits of the DTC paradigm is the hierarchical VEV model (HVM), where hierarchical multifermion condensates can address the flavour problem of the SM [23]. At low energy, these hierarchical multifermion condensates play the role of hierarchical VEVs of six gauge singlet scalar fields [19]. A standard version of the HVM (SHVM) is discussed in reference [24], which can predict very precise

leptonic mixing observables. Another possible low-energy limit of the DTC paradigm is the Froggatt-Nielsen (FN) mechanism [25] based on the $\mathcal{Z}_N \times \mathcal{Z}_M$ flavour symmetry [26].

In this work, we show explicitly that both the SHVM and the FN mechanism can be accommodated within the framework of the DTC paradigm, thus, resulting a solution of the flavour problem of the SM. Moreover, collider signatures of the DTC paradigm will be investigated at the High Luminosity Large Hadron Collider (HL-LHC), the High-Energy LHC (HE-LHC) [27], and a future high-luminosity 100 TeV hadron collider, such as FCC-hh [28], by accommodating the SHVM and the FN mechanism within the framework of the DTC paradigm.

Additionally, the dark-Higgs of the scenario, when the FN mechanism is implemented within the framework of the DTC paradigm, can address 95.4 GeV excess reported by the LHC. Furthermore, the dark-Higgs, corresponding to the scenario where the SHVM is accommodated within the DTC paradigm, becomes a new class of the chirality-dependent dark-matter particles.

This paper is organized as follows: In section 2, we briefly discuss the DTC paradigm. This is followed by a concise review of the EMAC hypothesis in section 3. In section 4, we present effective low-energy limits of the DTC paradigm, and show how to accommodate them explicitly within the framework of the DTC paradigm. We discuss the minimal version of the DTC paradigm in section 5, and show that it is not a preferred framework. The mass spectrum of the DTC paradigm is investigated through the scaling relations in section 7. We discuss the experimental constraints on the DTC paradigm in section 6. The collider-phenomenology of the DTC paradigm is investigated in section 8. The 95.4 GeV excess is interpreted through the dark-Higgs corresponding to the scenario, where the FN mechanism is built upon the framework of the DTC paradigm, in section 9. We introduce a new class of chirality-dependent dark matter in section 10, where the dark-Higgs, corresponding to the scenario when the SHVM is embedded within the framework of the DTC paradigm, acts like a dark-matter candidate. We summarize this work in section 11.

2 Dark-technicolour paradigm

We now discuss the dark-technicolour paradigm, which can give rise to the SHVM and the FN mechanism at low energies [19]. The DTC paradigm is based on symmetry $\mathcal{G} \equiv \text{SU}(N_{\text{TC}}) \times \text{SU}(N_{\text{DTC}}) \times \text{SU}(N_{\text{D}})$. The TC dynamics is defined by the TC fermions obeying the following transformations under the $\text{SU}(3)_c \times \text{SU}(2)_L \times \text{U}(1)_Y \times \mathcal{G}$ as [19],

$$T \equiv \begin{pmatrix} T \\ B \end{pmatrix}_L : (1, 2, 0, N_{\text{TC}}, 1, 1), \quad T_R^i : (1, 1, 1, N_{\text{TC}}, 1, 1), \quad B_R^i : (1, 1, -1, N_{\text{TC}}, 1, 1), \quad (2)$$

where $i = 1, 2, 3 \dots$, and electric charges are $Q_T = +\frac{1}{2}$ and $Q_B = -\frac{1}{2}$. For collider investigation, we assume only one TC fermion doublet, i.e. only two flavours.

The fermions of the DTC symmetry $\text{SU}(N_{\text{DTC}})$ transform under $\text{SU}(3)_c \times \text{SU}(2)_L \times \text{U}(1)_Y \times \mathcal{G}$ as,

$$D^i \equiv C_{L,R}^i : (1, 1, 1, 1, N_{\text{DTC}}, 1), \quad S_{L,R}^i : (1, 1, -1, 1, N_{\text{DTC}}, 1), \quad (3)$$

where $i = 1, 2, 3 \dots$, and electric charge of C is $+\frac{1}{2}$ and that of S is $-\frac{1}{2}$.

The DQCD symmetry $\text{SU}(N_{\text{D}})$ contains fermions transforming under $\text{SU}(3)_c \times \text{SU}(2)_L \times \text{U}(1)_Y \times \mathcal{G}$ as,

$$F_{L,R} \equiv U_{L,R}^i : (3, 1, \frac{4}{3}, 1, 1, N_{\text{D}}), \quad D_{L,R}^i : (3, 1, -\frac{2}{3}, 1, 1, N_{\text{D}}), \quad (4)$$

$$N_{L,R}^i : (1, 1, 0, 1, 1, N_{\text{D}}), \quad E_{L,R}^i : (1, 1, -2, 1, 1, N_{\text{D}}),$$

where $i = 1, 2, 3 \dots$.

We further assume that the TC fermions, the left-handed SM fermions, and the F_R fermions are accommodated in an extended TC (ETC) symmetry. On the other hand, there exists an extended DTC (EDTC) symmetry containing the DTC fermions, the right-handed SM fermions, and the F_L fermions. It is important to note that the $\text{SU}(N_{\text{D}})$ symmetry is a connecting bridge between the TC and DTC dynamics. This results in a suppression of the mixing between the dynamics of the TC and the DTC by the factor $1/\Lambda$, where Λ is the scale of the DQCD.

We notice that the symmetry \mathcal{G} gives rise to three global anomalous $U(1)_A$ symmetries denoted by $U(1)_A^{\text{TC}}$, $U(1)_A^{\text{DTC}}$ and $U(1)_A^{\text{D}}$ in the DTC paradigm. In general, a global axial symmetry $U(1)_A$ can be broken by instantons. This breaking provides a $2K$ -fermion operator with a non-vanishing VEV, and $2K$ conserved quantum numbers [29]. This can be written as,

$$U(1)_A \rightarrow \mathcal{Z}_{2K}, \quad (5)$$

where K denotes the massless flavours of the $SU(N)$ gauge dynamics in the N -dimensional representation.

Thus, the DTC paradigm creates a generic $\mathcal{Z}_N \times \mathcal{Z}_M \times \mathcal{Z}_P$ flavour symmetry, where $N = 2K_{\text{TC}}$, $M = 2K_{\text{DTC}}$, and $P = 2K_{\text{D}}$. This results in certain conserved axial charges modulo $2K$ [29].

3 Extended most attractive channel hypothesis

In a series of papers by Aoki and Bando (AB) [20, 21, 22], it was shown that a $2n$ -body multifermion state $(\bar{\psi}_L \psi_R)^n$ becomes more attractive as n increases. This fact can be parametrized in terms of the spin and chiral structure of multifermion systems [22]. We briefly review the details before addressing the experimental constraints on the DTC paradigm.

For the sake of demonstration [20, 21, 22], we first consider a two-fermion system in a non-Abelian colour gauge theory. The potential between fermions, assuming one-gauge boson exchange, can be written as,

$$V = g^2 F(i_1 i_2 i'_1 i'_2) \langle \lambda^a(1) \lambda^a(2) \rangle, \quad (6)$$

where $\lambda^a(n)$ show the generators of the gauge group $SU(N)$ for fermion n , g denotes the gauge coupling constant, and $i_n^{(\prime)}$ stands for all degrees of freedom such as momentum, spin, and chirality, excluding colour.

In the hypothesis of ‘‘most attractive channel’’ (MAC) [30], the factor F is common among fermions that live in different representations of the gauge group $SU(N)$, and condensation can be realized only in $\psi_L \psi_L$ or $\bar{\psi}_L \psi_R$ channels. Thus, the factor F behaves trivially within the MAC framework.

In the EMAC hypothesis [20, 21, 22], the factor F exhibits a non-trivially chiral dependence through the number of fermions present in the chiral condensate. The argument of AB goes as follows: since the potential given in equation 6 is attractive, any chiral condensate occurs with the scale μ satisfying the equation

$$-V(g^2(\mu^2)) \sim 1, \quad (7)$$

where the coupling constant $g^2(\mu^2)$ runs as,

$$g^2(\mu^2) = \frac{1}{\beta_0 \log \mu^2 / \Lambda^2}. \quad (8)$$

The solution of the running coupling can be written as,

$$\mu^2 \sim \Lambda^2 \exp(-F \langle \lambda \lambda \rangle / \beta_0). \quad (9)$$

We observe from this solution that the chiral difference among various channels is exponentialized due to the chiral degrees of freedom, which are parametrized inside F . However, the full structure of F is not known.

AB used $j = 1/2$ modes as a trial wave function for all left- and right-handed fermions to determine the dependence of F on the fermionic body number. This is achieved by defining an effective Hamiltonian of a multi-fermion system, which is obtained by summing up all combinations of two-fermions. The effective Hamiltonian can be written as the sum of the electric and magnetic parts. For the electric part of the interaction energy, all colour singlet states of the n -body system are degenerate. However, it turns out that the magnetic interaction energy is attractive for a colour singlet and spin-zero system with maximum chirality $(\bar{\psi}_R \psi_L)^{n/2}$ for even n . For the case of a two-body system, the most attractive channels are $\bar{\psi}_R \psi_L$ and $\psi_L \psi_L$ for spin-zero states, which are in agreement with the MAC hypothesis. In the case of a colour singlet and spin one, the most attractive channel with maximum chirality is $\bar{\psi}_L \psi_L$ for a two-body system. For more details, see [20, 21, 22].

In general, a n -body colour singlet and spin-zero multifermion condensate $(\bar{\psi}_R \psi_L)^{n/2}$ with maximum chirality for even n can be defined in terms of its energy as [20, 21, 22],

$$\bar{E}(n) = \frac{1}{n} E(\bar{\psi}_R^{n/2} \psi_L^{n/2}) \lesssim V_E^{LL} \frac{N^2 - 1}{N} - V_M^{LL} \frac{N - 1}{N} (n + 3N + 1), \quad (10)$$

where V_E^{LL} and V_M^{LL} show the electric and magnetic part of the Hamiltonian of two fermions.

We observe from the above result that $\bar{E}(n)$ has a linear decrease in n , resulting in more attractive multi-fermion systems. Thus, the larger values of n result in the hierarchical structure for the multifermion chiral condensations in the pattern

$$\langle \bar{\psi}_R \psi_L \rangle \ll \langle \bar{\psi}_R \bar{\psi}_R \psi_L \psi_L \rangle \ll \langle \bar{\psi}_R \bar{\psi}_R \bar{\psi}_R \psi_L \psi_L \psi_L \rangle \ll \dots \quad (11)$$

The above series is terminated by n_{\max} , which is equal to or less than the types of fermions present in theory [20, 21, 22].

Thus, the dependence of F on the fermionic body number n , turns out to be,

$$F \propto \Delta\chi, \quad (12)$$

where $\Delta\chi$ is the chirality of a multifermion operator. The hierarchy of a chiral multifermion condensate can be parametrized as [22],

$$\langle (\bar{\psi}_R \psi_L)^n \rangle \sim (\Lambda \exp(k\Delta\chi))^{3n}, \quad (13)$$

where k stands for a constant, and Λ denotes the scale of the underlying gauge dynamics.

As discussed earlier, a $U(1)_A$ symmetry is broken by instantons of strong dynamics, resulting in a $2K$ -fermion operator having $X_{\text{DTC}} = 2K$ quantum number [29]. It turns out that this operator is devoid of any other quantum number such as colour or flavour, producing the breaking of $U(1)_A$ axial symmetry to the \mathcal{Z}_{2K} conserved subgroup, and resulting in conserved axial quantum numbers X_A modulo $2K$ [29]. Using equations 11 and 13 along with the above observation, we conclude that the breaking of the $U(1)_A$ axial symmetry occurs in the following steps [22],

$$U(1)_A \rightarrow \mathcal{Z}_{2K} \cdots \mathcal{Z}_{24} \rightarrow \mathcal{Z}_{22} \rightarrow \mathcal{Z}_{20} \rightarrow \mathcal{Z}_{18} \rightarrow \mathcal{Z}_{16} \rightarrow \mathcal{Z}_{12} \rightarrow \mathcal{Z}_{10} \rightarrow \mathcal{Z}_8 \rightarrow \mathcal{Z}_6 \rightarrow \mathcal{Z}_4 \rightarrow \mathcal{Z}_2, \quad (14)$$

where the first breaking is produced due to the instanton effects.

4 Effective low energy limits of the DTC paradigm

The DTC paradigm can be mapped onto the SHVM and the FN mechanism based on the $\mathcal{Z}_N \times \mathcal{Z}_M$ symmetry at low energies, as shown in figure 1. In this section, we discuss how to achieve their effective low-energy manifestations.

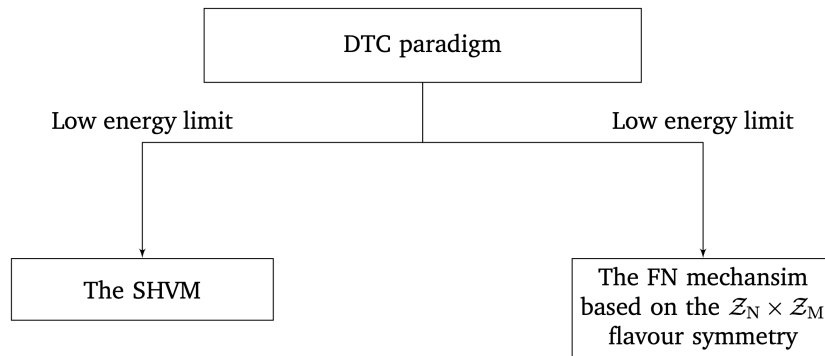


Figure 1: At low energies, the DTC paradigm may effectively reduce to either the SHVM or the FN mechanism.

4.1 Standard HVM

One of the possible low energy limits of the DTC paradigm is the SHVM, where the flavour problem is solved by introducing six gauge singlet scalar fields χ_r coupled to the charged fermions and the singlet scalar field χ_7 coupled only to the neutrino sector [23, 19, 24, 31]. In the SHVM, it is assumed that the gauge singlet scalar fields χ_r are multifermions chiral condensates of the DTC paradigm. In this section, we briefly review the details of the SHVM.

The gauge singlet scalar fields χ_r transform under the SM symmetry $\mathcal{G}_{\text{SM}} \equiv \text{SU}(3)_c \times \text{SU}(2)_L \times \text{U}(1)_Y$ as,

$$\chi_r : (1, 1, 0), \quad (15)$$

where $r = 1 - 6$.

The masses of the charged fermions originate from the following dimension-5 Lagrangian,

$$\mathcal{L} = \frac{1}{\Lambda} \left[y_{ij}^u \bar{\psi}_{L_i}^q \tilde{\varphi} \psi_{R_i}^u \chi_r + y_{ij}^d \bar{\psi}_{L_i}^q \varphi \psi_{R_i}^d \chi_r + y_{ij}^\ell \bar{\psi}_{L_i}^\ell \varphi \psi_{R_i}^\ell \chi_r \right] + \text{H.c.}, \quad (16)$$

i and j stand for family indices, ψ_L^q, ψ_L^ℓ denote the quark and leptonic doublets, $\psi_R^u, \psi_R^d, \psi_R^\ell$ are the right-handed up, down-type quarks and leptons, φ and $\tilde{\varphi} = -i\sigma_2 \varphi^*$ show the SM Higgs field, and its conjugate, where σ_2 is the second Pauli matrix.

The charged fermion mass pattern and quark mixing is obtained by assigning the following generic charges under the $\mathcal{Z}_N \times \mathcal{Z}_M \times \mathcal{Z}_P$ flavour symmetry,

$$\begin{aligned} \psi_{L_1}^q &: (+, 1, \omega_{14}^{P-1}), \quad \psi_{L_2}^q : (+, 1, \omega_{14}), \quad \psi_{L_3}^q : (+, 1, \omega_{14}^2), \\ u_R &: (-, 1, \omega_{14}^{P-3}), \quad c_R : (+, 1, \omega_{14}^6), \quad t_R : (+, 1, \omega_{14}^4), \\ d_R &: (-, 1, \omega_{14}^{12}), \quad s_R : (+, 1, \omega_{14}^{12}), \quad b_R : (+, 1, \omega_{14}^{12}), \\ \psi_{L_1}^\ell &: (+, \omega_4^3, \omega_{14}^{12}), \quad \psi_{L_2}^\ell : (+, \omega_4^3, \omega_{14}^{10}), \quad \psi_{L_3}^\ell : (+, \omega_4^3, \omega_{14}^6), \\ e_R &: (-, \omega_4^3, \omega_{14}^{10}), \quad \mu_R : (+, \omega_4^3, \omega_{14}^{P-1}), \quad \tau_R : (+, \omega_4^3, \omega_{14}), \\ \chi_1 &: (-, 1, \omega_{14}^2), \quad \chi_2 : (+, 1, \omega_{14}^5), \quad \chi_3 : (+, 1, \omega_{14}^2), \\ \chi_4 &: (+, 1, \omega_{14}^{13}), \quad \chi_5 : (+, 1, \omega_{14}^{11}), \quad \chi_6 : (+, 1, \omega_{14}^{10}), \end{aligned} \quad (17)$$

where ω_4 denotes the fourth and ω_{14} is the fourteenth root of unity corresponding to the symmetries \mathcal{Z}_4 and \mathcal{Z}_{14} , respectively. Moreover, we need $N = 2$, $M \geq 4$, and $P \geq 14$ for producing the charged flavour pattern. We observe that the desired flavour structure of the charged fermions requires $N = 2$.

We recover the neutrino masses by adding three right-handed neutrinos $\nu_{eR}, \nu_{\mu R}, \nu_{\tau R}$ and the singlet scalar field χ_7 to the SM, and by writing the dimension-6 operators as,

$$-\mathcal{L}_{\text{Yukawa}}^\nu = y_{ij}^\nu \bar{\psi}_{L_i}^\ell \tilde{\varphi} \nu_{fR} \left[\frac{\chi_r \chi_7 (\text{or } \chi_r \chi_7^\dagger)}{\Lambda^2} \right] + \text{H.c.} \quad (18)$$

It is remarkable that to produce the normal ordered neutrino masses and the observables of leptonic mixing, we must have $P = 14$ for the symmetry \mathcal{Z}_P , which makes $P = 14$ a magic number. For instance, we assign charges to different fermionic and scalar fields under the $\mathcal{Z}_2 \times \mathcal{Z}_4 \times \mathcal{Z}_{14}$ flavour symmetry as shown in table 1.

The masses of charged fermions are now produced by the Lagrangian,

$$\begin{aligned} \mathcal{L}_f &= \frac{1}{\Lambda} \left[y_{11}^u \bar{\psi}_{L_1}^q \tilde{\varphi} \psi_{R_1}^u \chi_1 + y_{13}^u \bar{\psi}_{L_1}^q \tilde{\varphi} \psi_{R_3}^u \chi_2^\dagger + y_{22}^u \bar{\psi}_{L_2}^q \tilde{\varphi} \psi_{R_2}^u \chi_2^\dagger + y_{23}^u \bar{\psi}_{L_2}^q \tilde{\varphi} \psi_{R_3}^u \chi_5 + y_{32}^u \bar{\psi}_{L_3}^q \tilde{\varphi} \psi_{R_2}^u \chi_6 \right. \\ &+ y_{33}^u \bar{\psi}_{L_3}^q \tilde{\varphi} \psi_{R_3}^u \chi_3^\dagger + y_{11}^d \bar{\psi}_{L_1}^q \varphi \psi_{R_1}^d \chi_4^\dagger + y_{12}^d \bar{\psi}_{L_1}^q \varphi \psi_{R_2}^d \chi_4^\dagger + y_{13}^d \bar{\psi}_{L_1}^q \varphi \psi_{R_3}^d \chi_4^\dagger + y_{21}^d \bar{\psi}_{L_2}^q \varphi \psi_{R_1}^d \chi_5^\dagger \\ &+ y_{22}^d \bar{\psi}_{L_2}^q \varphi \psi_{R_2}^d \chi_5^\dagger + y_{23}^d \bar{\psi}_{L_2}^q \varphi \psi_{R_3}^d \chi_5^\dagger + y_{31}^d \bar{\psi}_{L_3}^q \varphi \psi_{R_1}^d \chi_6^\dagger + y_{32}^d \bar{\psi}_{L_3}^q \varphi \psi_{R_2}^d \chi_6^\dagger + y_{33}^d \bar{\psi}_{L_3}^q \varphi \psi_{R_3}^d \chi_6^\dagger \\ &+ y_{11}^\ell \bar{\psi}_{L_1}^\ell \varphi \psi_{R_1}^\ell \chi_1 + y_{12}^\ell \bar{\psi}_{L_1}^\ell \varphi \psi_{R_2}^\ell \chi_4 + y_{13}^\ell \bar{\psi}_{L_1}^\ell \varphi \psi_{R_3}^\ell \chi_5 + y_{22}^\ell \bar{\psi}_{L_2}^\ell \varphi \psi_{R_2}^\ell \chi_5 + y_{23}^\ell \bar{\psi}_{L_2}^\ell \varphi \psi_{R_3}^\ell \chi_2^\dagger \\ &\left. + y_{33}^\ell \bar{\psi}_{L_3}^\ell \varphi \psi_{R_3}^\ell \chi_2 + \text{H.c.} \right]. \quad (19) \end{aligned}$$

Fields	\mathcal{Z}_2	\mathcal{Z}_4	\mathcal{Z}_{14}	Fields	\mathcal{Z}_2	\mathcal{Z}_4	\mathcal{Z}_{14}	Fields	\mathcal{Z}_2	\mathcal{Z}_4	\mathcal{Z}_{14}	Fields	\mathcal{Z}_2	\mathcal{Z}_4	\mathcal{Z}_{14}
u_R	-	1	ω_{14}^{11}	d_R, s_R, b_R	+	1	ω_{14}^{12}	$\psi_{L_3}^q$	+	1	ω_{14}^2	τ_R	+	ω_4^3	ω_{14}
c_R	+	1	ω_{14}^6	χ_4	+	1	ω_{14}^{13}	$\psi_{L_1}^\ell$	+	ω_4^3	ω_{14}^{12}	ν_{e_R}	+	ω_4	ω_{14}^8
t_R	+	1	ω_{14}^4	χ_5	+	1	ω_{14}^{11}	$\psi_{L_2}^\ell$	+	ω_4^3	ω_{14}^{10}	ν_{μ_R}	-	ω_4	ω_{14}^3
χ_1	-	1	ω_{14}^2	χ_6	+	1	ω_{14}^{10}	$\psi_{L_3}^\ell$	+	ω_4^3	ω_{14}^6	ν_{τ_R}	-	ω_4	ω_{14}^3
χ_2	+	1	ω_{14}^5	$\psi_{L_1}^q$	+	1	ω_{14}^{13}	e_R	-	ω_4^3	ω_{14}^{10}	χ_7	-	ω_4^2	ω_{14}^8
χ_3	+	1	ω_{14}^2	$\psi_{L_2}^q$	+	1	ω_{14}	μ_R	+	ω_4^3	ω_{14}^{13}	φ	+	1	1

Table 1: The transformation charges of left- and right-handed fermions, as well as scalar fields, under the \mathcal{Z}_2 , \mathcal{Z}_4 , and \mathcal{Z}_{14} symmetries for the normal mass ordering are presented. Here, ω_4 and ω_{14} represent the fourth and fourteenth roots of unity associated with the \mathcal{Z}_4 and \mathcal{Z}_{14} symmetries, respectively.

The fermionic mass pattern can be explained in terms of the VEVs pattern $\langle \chi_4 \rangle > \langle \chi_1 \rangle, \langle \chi_2 \rangle \gg \langle \chi_5 \rangle, \langle \chi_3 \rangle \gg \langle \chi_6 \rangle, \langle \chi_3 \rangle \gg \langle \chi_2 \rangle \gg \langle \chi_1 \rangle$, and $\langle \chi_6 \rangle \gg \langle \chi_5 \rangle \gg \langle \chi_4 \rangle$.

The mass matrices of up, down-type quarks and leptons read as,

$$\mathcal{M}_U = \frac{v}{\sqrt{2}} \begin{pmatrix} y_{11}^u \epsilon_1 & 0 & y_{13}^u \epsilon_2 \\ 0 & y_{22}^u \epsilon_2 & y_{23}^u \epsilon_5 \\ 0 & y_{32}^u \epsilon_6 & y_{33}^u \epsilon_3 \end{pmatrix}, \mathcal{M}_D = \frac{v}{\sqrt{2}} \begin{pmatrix} y_{11}^d \epsilon_4 & y_{12}^d \epsilon_4 & y_{13}^d \epsilon_4 \\ y_{21}^d \epsilon_5 & y_{22}^d \epsilon_5 & y_{23}^d \epsilon_5 \\ y_{31}^d \epsilon_6 & y_{32}^d \epsilon_6 & y_{33}^d \epsilon_6 \end{pmatrix}, \mathcal{M}_\ell = \frac{v}{\sqrt{2}} \begin{pmatrix} y_{11}^\ell \epsilon_1 & y_{12}^\ell \epsilon_4 & y_{13}^\ell \epsilon_5 \\ 0 & y_{22}^\ell \epsilon_5 & y_{23}^\ell \epsilon_2 \\ 0 & 0 & y_{33}^\ell \epsilon_2 \end{pmatrix}, \quad (20)$$

where $\epsilon_r = \frac{\langle \chi_r \rangle}{\Lambda}$ and $\epsilon_r < 1$.

The masses of charged fermions can be written as,

$$\begin{aligned} m_t &= |y_{33}^u| \epsilon_3 v / \sqrt{2}, \quad m_c = \left| y_{22}^u \epsilon_2 - \frac{y_{23}^u y_{32}^u \epsilon_5 \epsilon_6}{y_{33}^u \epsilon_3} \right| v / \sqrt{2}, \quad m_u = |y_{11}^u| \epsilon_1 v / \sqrt{2}, \\ m_b &\approx |y_{33}^d| \epsilon_6 v / \sqrt{2}, \quad m_s \approx \left| y_{22}^d - \frac{y_{23}^d y_{32}^d}{y_{33}^d} \right| \epsilon_5 v / \sqrt{2}, \\ m_d &\approx \left| y_{11}^d - \frac{y_{12}^d y_{21}^d}{y_{22}^d - \frac{y_{23}^d y_{32}^d}{y_{33}^d}} - \frac{y_{13}^d (y_{31}^d y_{22}^d - y_{21}^d y_{32}^d) - y_{31}^d y_{12}^d y_{23}^d}{(y_{22}^d - \frac{y_{23}^d y_{32}^d}{y_{33}^d}) y_{33}^d} \right| \epsilon_4 v / \sqrt{2}, \\ m_\tau &\approx |y_{33}^\ell| \epsilon_2 v / \sqrt{2}, \quad m_\mu \approx |y_{22}^\ell| \epsilon_5 v / \sqrt{2}, \quad m_e = |y_{11}^\ell| \epsilon_1 v / \sqrt{2}. \end{aligned} \quad (21)$$

The quark mixing angles are given by,

$$\sin \theta_{12} \simeq \left| \frac{y_{12}^d \epsilon_4}{y_{22}^d \epsilon_5} \right| = \frac{\epsilon_4}{\epsilon_5}, \quad \sin \theta_{23} \simeq \left| \frac{y_{23}^d \epsilon_5}{y_{33}^d \epsilon_6} - \frac{y_{23}^u \epsilon_5}{y_{33}^u \epsilon_3} \right|, \quad \sin \theta_{13} \simeq \left| \frac{y_{13}^d \epsilon_4}{y_{33}^d \epsilon_6} - \frac{y_{13}^u \epsilon_2}{y_{33}^u \epsilon_3} \right|. \quad (22)$$

Assuming all $|y_{ij}^d| = 1$, the quark mixing angles turn out to be,

$$\begin{aligned} \sin \theta_{12} &\simeq \frac{\epsilon_4}{\epsilon_5}, \\ \sin \theta_{23} &\simeq \frac{\epsilon_5}{\epsilon_6}, \\ \sin \theta_{13} &\simeq \frac{\epsilon_4}{\epsilon_6} - \left| \frac{y_{13}^u}{y_{33}^u} \right| \frac{\epsilon_2}{\epsilon_3}. \end{aligned} \quad (23)$$

This provides the prediction of the quark mixing angle θ_{13} as,

$$\sin \theta_{13} \simeq \sin \theta_{12} \sin \theta_{23} - \frac{\epsilon_2}{\epsilon_3}, \quad (24)$$

assuming $|y_{ij}^u| = 1$. The quark mixing angle $\sin \theta_{13}$ can be predicted for an allowed value $\epsilon_3 = 0.55$.

In general, the ϵ_r parameters are [24],

$$\epsilon_1 = 3.16 \times 10^{-6}, \quad \epsilon_2 = 0.0031, \quad \epsilon_3 = 0.87, \quad \epsilon_4 = 0.000061, \quad \epsilon_5 = 0.000270, \quad \epsilon_6 = 0.0054, \quad \epsilon_7 = 7.18 \times 10^{-10}. \quad (25)$$

The SHVM allows only Dirac-type neutrinos. The mass matrix for neutrinos is given by,

$$\mathcal{M}_{\mathcal{N}} = \frac{v}{\sqrt{2}} \begin{pmatrix} y_{11}' \epsilon_1 \epsilon_7 & y_{12}' \epsilon_4 \epsilon_7 & y_{13}' \epsilon_4 \epsilon_7 \\ 0 & y_{22}' \epsilon_4 \epsilon_7 & y_{23}' \epsilon_4 \epsilon_7 \\ 0 & y_{32}' \epsilon_5 \epsilon_7 & y_{33}' \epsilon_5 \epsilon_7 \end{pmatrix}. \quad (26)$$

The neutrino masses can be written as,

$$m_3 \approx |y_{33}'| \epsilon_5 \epsilon_7 v / \sqrt{2}, \quad m_2 \approx |y_{22}' - \frac{y_{23}' y_{32}'}{y_{33}'}| \epsilon_4 \epsilon_7 v / \sqrt{2}, \quad m_1 \approx |y_{11}'| \epsilon_1 \epsilon_7 v / \sqrt{2}, \quad (27)$$

The masses of neutrinos are of the order $\{m_3, m_2, m_1\} = \{5.05 \times 10^{-2}, 8.67 \times 10^{-3}, 2.67 \times 10^{-4}\}$ eV [24].

The neutrino mixing angles are the main predictions of the SHVM, and are given by,

$$\sin \theta_{12}^\ell \simeq \left| \frac{y_{12}^\ell \epsilon_4}{y_{22}^\ell \epsilon_5} - \frac{y_{12}'}{y_{22}'} + \frac{y_{23}^{\ell*} y_{13}' \epsilon_4}{y_{33}^\ell y_{33}' \epsilon_5} \right|, \quad \sin \theta_{23}^\ell \simeq \left| \frac{y_{23}^\ell}{y_{33}^\ell} - \frac{y_{23}' \epsilon_4}{y_{33}' \epsilon_5} \right|, \quad \sin \theta_{13}^\ell \simeq \left| \frac{y_{13}^\ell \epsilon_5}{y_{33}^\ell \epsilon_2} - \frac{y_{13}' \epsilon_4}{y_{33}' \epsilon_5} \right|. \quad (28)$$

We assume all the couplings of the order one, and write,

$$\begin{aligned} \sin \theta_{12}^\ell &\simeq \left| \frac{y_{12}'}{y_{22}'} + \frac{y_{12}^\ell \epsilon_4}{y_{22}^\ell \epsilon_5} + \frac{y_{23}^{\ell*} y_{13}' \epsilon_4}{y_{33}^\ell y_{33}' \epsilon_5} \right| \geq \left| \frac{y_{12}'}{y_{22}'} \right| - \left| \frac{y_{12}^\ell}{y_{22}^\ell} + \frac{y_{23}^{\ell*} y_{13}'}{y_{33}^\ell y_{33}'} \right| \frac{\epsilon_4}{\epsilon_5} \approx 1 - 2 \sin \theta_{12}, \quad (29) \\ \sin \theta_{23}^\ell &\simeq \left| \frac{y_{23}^\ell}{y_{33}^\ell} - \frac{y_{23}' \epsilon_4}{y_{33}' \epsilon_5} \right| \geq \left| \frac{y_{23}^\ell}{y_{33}^\ell} \right| - \left| \frac{y_{23}'}{y_{33}'} \right| \frac{\epsilon_4}{\epsilon_5} \approx 1 - \sin \theta_{12}, \\ \sin \theta_{13}^\ell &\simeq \left| \frac{y_{13}' \epsilon_4}{y_{33}' \epsilon_5} + \frac{y_{13}^\ell \epsilon_5}{y_{33}^\ell \epsilon_2} \right| \geq \left| \frac{y_{13}'}{y_{33}'} \right| \frac{\epsilon_4}{\epsilon_5} - \left| \frac{y_{13}^\ell}{y_{33}^\ell} \right| \frac{\epsilon_5}{\epsilon_2} \approx \sin \theta_{12} - \frac{m_s}{m_c}, \end{aligned}$$

where $m_s/m_c = \epsilon_5/\epsilon_2$. This result shows that the leptonic mixing angles can be predicted in terms of the Cabibbo angle and masses of strange and charm quarks. Moreover, notable result are the prediction of correct and precise order of mixing angles, and the pattern $\sin \theta_{23}^\ell > \sin \theta_{12}^\ell \gg \sin \theta_{13}^\ell$. Flavour bounds and collider signatures of the SHVM are discussed in the reference [31].

4.2 The SHVM within the DTC-paradigm

The SHVM is one of the possible low-energy limits of the DTC paradigm. In this section, we show how to accommodate the SHVM within the framework of the DTC paradigm. The DTC paradigm provides the interactions responsible for creating the charged fermion mass matrix in the SHVM as shown in the upper part of figure 2. We show the formation of chiral TC condensates, which play the role of the Higgs VEV, and the DTC multifermion chiral condensates denoted by $\langle \chi_r \rangle$ in the lower part of figure 2.

The chiral condensate for a QCD-like theory, using equation 13, is given by [32],

$$\begin{aligned} \langle \bar{T}T \rangle_{\Lambda_{\text{ETC}}} &\approx - \frac{N_{\text{TC}}}{4\pi^2} [\Lambda_{\text{TC}} \exp(k_{\text{TC}} \Delta \chi_{\text{TC}})]^3, \quad (30) \\ \langle \bar{D}D \rangle_{\Lambda_{\text{EDTC}}} &\approx - \frac{N_{\text{DTC}}}{4\pi^2} [\Lambda_{\text{DTC}} \exp(k_{\text{DTC}} \Delta \chi_{\text{DTC}})]^3, \end{aligned}$$

$$\langle \bar{F}F \rangle_{\Lambda_{\text{GUT}}} \approx -\frac{N_{\text{D}}}{4\pi^2} [\Lambda \exp(k_{\text{D}} \Delta\chi_{\text{D}})]^3.$$

The mass matrices of the charged fermions in equation 20 are now approximately given by,

$$\mathcal{M}_{U,D,\ell} \propto N_{\text{D}}^n \left[\frac{g_{\text{ETC}}^2}{\Lambda_{\text{ETC}}^2} \langle \bar{T}T \rangle_{\Lambda_{\text{ETC}}} \right] \frac{1}{\Lambda} \left[\frac{g_{\text{EDTC}}^{2n}}{\Lambda_{\text{EDTC}}^{3n-1}} (\langle \bar{D}D \rangle_{\Lambda_{\text{EDTC}}})^n \right]. \quad (31)$$

where $n = 1, 2, 3 \dots$ and $f = u, d, \ell$.

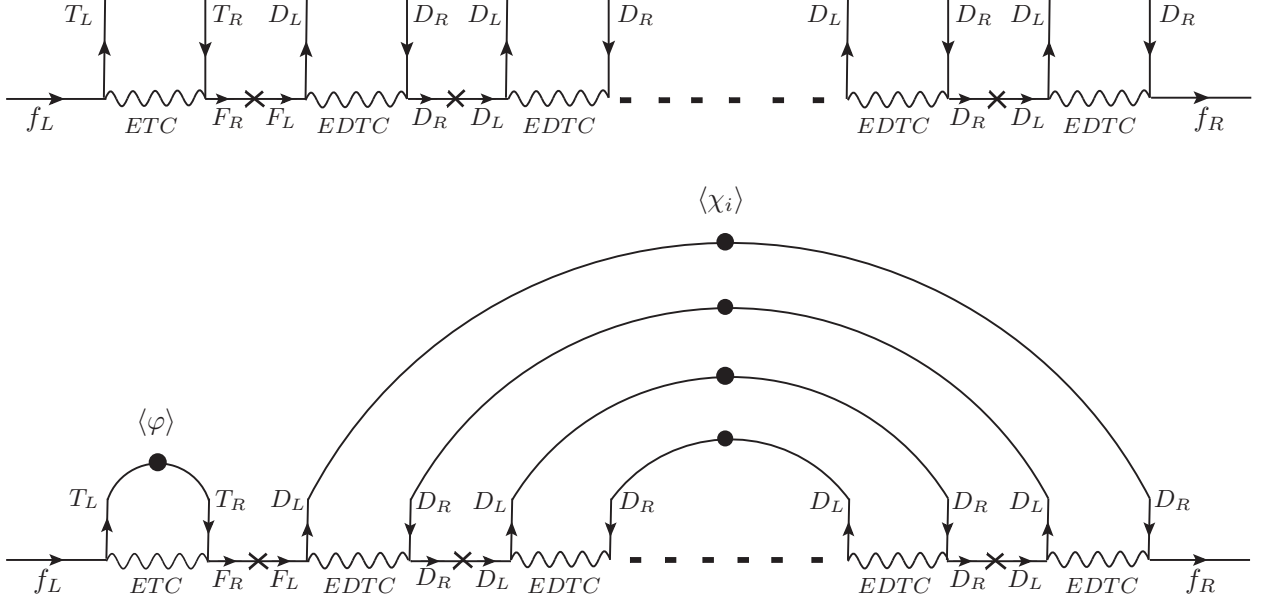


Figure 2: The Feynman diagrams for the masses of charged fermions in the DTC paradigm. The top part shows the generic interactions of the SM, TC, DQCD and DTC fermions. In the lower part of figure, the formations of the TC chiral condensates, $\langle \varphi \rangle$ (circular blob), a generic multifermion chiral condensates $\langle \chi_r \rangle$ (collection of circular blobs), and the resulting mass of the SM charged fermion is depicted.

Using equation 30, the mass matrices can further be written as,

$$\mathcal{M}_{U,D,\ell} = y_{ij}^f N_{\text{D}}^{n_i/2} \frac{N_{\text{TC}}}{4\pi^2} \frac{\Lambda_{\text{TC}}^3}{\Lambda_{\text{ETC}}^2} \exp(6k_{\text{TC}}) \frac{1}{\Lambda} \left[\frac{N_{\text{DTC}}}{4\pi^2} \right]^{n_i} \frac{\Lambda_{\text{DTC}}^{n_i+1}}{\Lambda_{\text{EDTC}}^{n_i}} [\exp(3n_i k_{\text{DTC}})]^{n_i/2}, \quad (32)$$

where we have assumed that the TC chiral condensate is of the type $\langle \bar{T}_R T_L \rangle$ and $\Delta\chi_{\text{TC}} = 2$. Moreover, $g_{\text{ETC}} = g_{\text{EDTC}} = (1 - 4\pi)$, and $k_{\text{TC}} > 0$ are assumed. Furthermore, $n_i = 2, 4, 6, \dots, 2n$ are the number of fermions in a multifermion chiral DTC condensate that plays the role of the VEV $\langle \chi_r \rangle$ [19], and Λ_{TC} , Λ_{DTC} , and Λ denote the scale of the TC, DTC, and DQCD dynamics respectively.

We conclude from equation 32 that

$$\epsilon_r \propto \frac{1}{\Lambda} \left[\frac{N_{\text{DTC}}}{4\pi^2} \right]^{n_i} \frac{\Lambda_{\text{DTC}}^{n_i+1}}{\Lambda_{\text{EDTC}}^{n_i}} [\exp(3n_i k_{\text{DTC}})]^{n_i/2}. \quad (33)$$

Thus, the masses of charged fermions given in equation 21 can be written in terms of equation 33, and at the leading order, the mass of a charged fermion is,

$$m_f \approx |y_{11}^f| N_{\text{D}}^{n_i/2} \frac{N_{\text{TC}}}{4\pi^2} \frac{\Lambda_{\text{TC}}^3}{\Lambda_{\text{ETC}}^2} \exp(6k_{\text{TC}}) \frac{1}{\Lambda} \left[\frac{N_{\text{DTC}}}{4\pi^2} \right]^{n_i} \frac{\Lambda_{\text{DTC}}^{n_i+1}}{\Lambda_{\text{EDTC}}^{n_i}} [\exp(3n_i k_{\text{DTC}})]^{n_i/2}. \quad (34)$$

For obtaining neutrino masses, we assume that the ETC and EDTC symmetries further unify in a GUT theory, leading to dimension-6 operators given in equation 18 from which the neutrino masses originate. The resulting interactions are shown in the upper part of Figure 3, which are mediated by the GUT gauge bosons among the F_L and F_R fermions. The chiral condensate $\langle \bar{F}_L F_R \rangle$ (circular blob) acts like the VEV $\langle \chi_7 \rangle$. A generic formation of the neutrino mass term is shown in the lower part of the figure 3.

The neutrino mass matrix given in equation 26 is recovered as,

$$\mathcal{M}_{\mathcal{N}} = y_{ij}^{\nu} N_D^{(n_i+2)/2} \frac{N_{\text{TC}}}{4\pi^2} \frac{\Lambda_{\text{TC}}^3}{\Lambda_{\text{ETC}}^2} \exp(6k_{\text{TC}}) \frac{1}{\Lambda} \left[\frac{N_{\text{DTC}}}{4\pi^2} \right]^{n_i} \frac{\Lambda_{\text{DTC}}^{n_i+1}}{\Lambda_{\text{EDTC}}^{n_i}} [\exp(n_i k_{\text{DTC}})]^{n_i/2} \frac{1}{\Lambda} \frac{N_D}{4\pi^2} \frac{\Lambda^3}{\Lambda_{\text{GUT}}^2} \exp(6k_D), \quad (35)$$

where,

$$\epsilon_7 \propto \frac{1}{\Lambda} \frac{N_D}{4\pi^2} \frac{\Lambda^3}{\Lambda_{\text{GUT}}^2} \exp(6k_D). \quad (36)$$

The masses of neutrinos at the leading order turn out to be,

$$m_{\nu} = |y_{11}^{\nu}| N_D^{(n_i+2)/2} \frac{N_{\text{TC}}}{4\pi^2} \frac{\Lambda_{\text{TC}}^3}{\Lambda_{\text{ETC}}^2} \exp(6k_{\text{TC}}) \frac{1}{\Lambda} \left[\frac{N_{\text{DTC}}}{4\pi^2} \right]^{n_i} \frac{\Lambda_{\text{DTC}}^{n_i+1}}{\Lambda_{\text{EDTC}}^{n_i}} [\exp(3n_i k_{\text{DTC}})]^{n_i/2} \frac{1}{\Lambda} \frac{N_D}{4\pi^2} \frac{\Lambda^3}{\Lambda_{\text{GUT}}^2} \exp(6k_D). \quad (37)$$

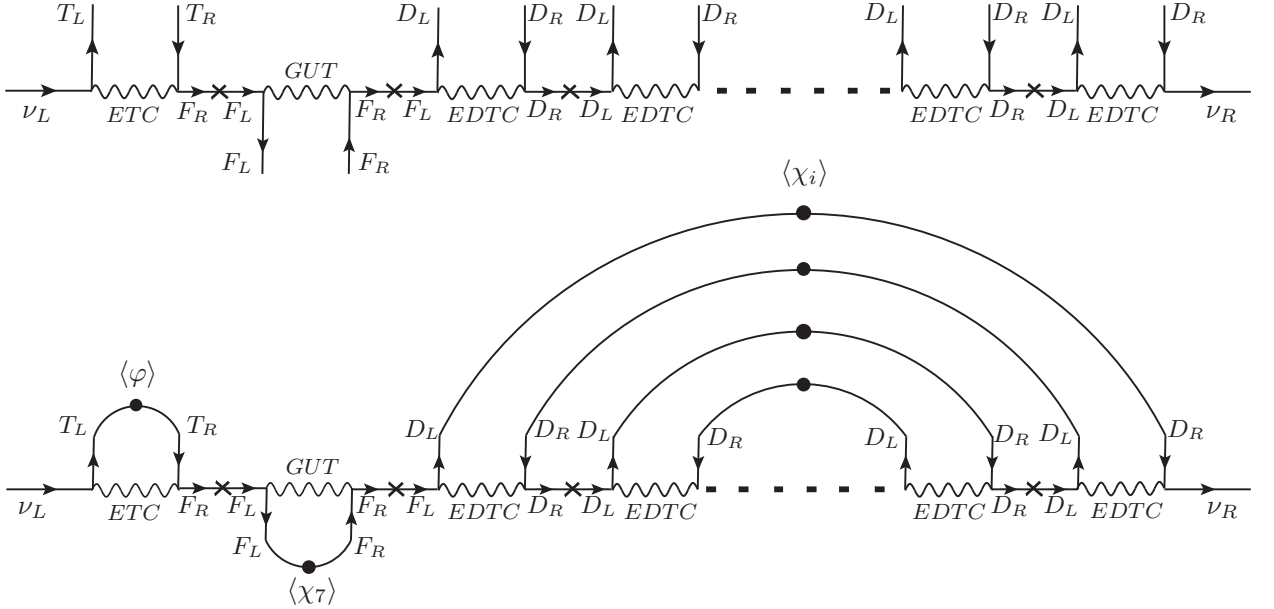


Figure 3: The Feynman diagrams for the masses of neutrinos in the DTC paradigm. On the top, there are generic interactions involving the SM, TC, DQCD and DTC gauge sectors mediated by ETC, EDTC and GUT gauge bosons. In the bottom, we show the generic Feynman diagram after the formation of the fermionic condensates.

For fitting fermion masses and mixing, we map the fermionic mass matrices, given in equations 20 and equation 26, onto equation 32 and equation 35, respectively. The numerical values of fermion masses are used at 1 TeV given in reference [33],

$$\begin{aligned} \{m_t, m_c, m_u\} &\simeq \{150.7 \pm 3.4, 0.532_{-0.073}^{+0.074}, (1.10_{-0.37}^{+0.43}) \times 10^{-3}\} \text{ GeV}, \\ \{m_b, m_s, m_d\} &\simeq \{2.43 \pm 0.08, 4.7_{-1.3}^{+1.4} \times 10^{-2}, 2.50_{-1.03}^{+1.08} \times 10^{-3}\} \text{ GeV}, \\ \{m_{\tau}, m_{\mu}, m_e\} &\simeq \{1.78 \pm 0.2, 0.105_{-9.3 \times 10^{-9}}^{+9.4 \times 10^{-9}}, 4.96 \pm 0.00000043 \times 10^{-4}\} \text{ GeV}. \end{aligned} \quad (38)$$

The magnitudes and phases of the CKM mixing elements are [34],

$$|V_{ud}| = 0.97370 \pm 0.00014, |V_{cb}| = 0.0410 \pm 0.0014, |V_{ub}| = 0.00382 \pm 0.00024, \delta = 1.196_{-0.043}^{+0.045}. \quad (39)$$

The values of the mass square parameters and leptonic mixing angles for the normal mass ordering are taken from the global fit [35],

$$\begin{aligned} \Delta m_{21}^2 &= (7.50_{-0.56}^{+0.64}) \times 10^{-5} \text{eV}^2, |\Delta m_{31}^2| = (2.55 \pm 0.08) \times 10^{-3} \text{eV}^2, \\ \sin \theta_{12}^\ell &= (0.564_{-0.043}^{+0.044}), \sin \theta_{23}^\ell = (0.758_{-0.099}^{+0.023}), \sin \theta_{13}^\ell = (0.1483_{-0.0069}^{+0.0067}), \end{aligned} \quad (40)$$

where the errors are in 3σ range.

We fit fermion masses and mixing by defining the χ^2 as,

$$\begin{aligned} \chi^2 &= \frac{(m_q - m_q^{\text{model}})^2}{\sigma_{m_q}^2} + \frac{(\sin \theta_{ij} - \sin \theta_{ij}^{\text{model}})^2}{\sigma_{\sin \theta_{ij}}^2} + \frac{(m_\ell - m_\ell^{\text{model}})^2}{\sigma_{m_\ell}^2} + \frac{(\Delta m_{21}^2 - \Delta m_{21}^{2,\text{model}})^2}{\sigma_{\Delta m_{21}^2}^2} \\ &+ \frac{(\Delta m_{31}^2 - \Delta m_{31}^{2,\text{model}})^2}{\sigma_{\Delta m_{31}^2}^2} + \frac{(\sin \theta_{ij}^\ell - \sin \theta_{ij}^{\ell,\text{model}})^2}{\sigma_{\sin \theta_{ij}^\ell}^2}, \end{aligned} \quad (41)$$

where $q = \{u, d, c, s, t, b\}$, $\ell = \{e, \mu, \tau\}$, and $i, j = 1, 2, 3$.

The dimensionless coefficients $y_{ij}^{u,d} = |y_{ij}^{u,d}| e^{i\phi_{ij}^q}$ are scanned in the range $|y_{ij}^{u,d}| \in [0.3, 4\pi]$ and $\phi_{ij}^q \in [0, 2\pi]$. The fitting is performed for three different scenarios.

4.2.1 $\Lambda \approx \Lambda_{\text{DTC}}$

In the scenario where $\{n_1, n_2, n_3, n_4, n_5, n_6, n_7\} = \{2, 4, 6, 2, 2, 4, 2\}$, the fit results are,

$$\begin{aligned} N_{\text{TC}} = 16, N_{\text{DTC}} = 17, N_{\text{D}} = 17, \Lambda_{\text{TC}} = 618.5 \text{ GeV}, \Lambda_{\text{ETC}} = 10^7 \text{ GeV}, \Lambda_{\text{DTC}} = 500 \text{ GeV}, \Lambda_{\text{EDTC}} = 510 \text{ GeV}, \\ \Lambda = 500 \text{ GeV}, \Lambda_{\text{GUT}} = 2 \times 10^{16} \text{ GeV}, k_{\text{TC}} = 1.15, k_{\text{DTC}} = 0.069, k_{\text{D}} = 6.51. \end{aligned} \quad (42)$$

The dimensionless couplings $y_{ij}^{u,d}$ are,

$$y_{ij}^u = \begin{pmatrix} -0.09 + 0.05i & 0 & -0.51 + 0.82i \\ 0 & 2.95 + 0.12i & -11.10 + 4.57i \\ 0 & 2.92 - 6.53i & 3.54 + 0.i \end{pmatrix}, \quad (43)$$

$$y_{ij}^d = \begin{pmatrix} -2.91 - 3.18i & 1.99 + 0.39i & 1.12 - 0.40i \\ -10.80 - 2.53i & 7.10 - 5.45i & -10.24 - 6.25i \\ 1.26 + 0.39i & -1.78 - 2.86i & -9.91 + 6.71i \end{pmatrix}, \quad (44)$$

The dimensionless couplings $y_{ij}^{\ell,\nu}$ are,

$$y_{ij}^\ell = \begin{pmatrix} 0.82 - 0.58i & 1 & 1 \\ 0 & -1.09 - 0.17i & 1 \\ 0 & 0 & -1.09 + 0.16i \end{pmatrix}, \quad (45)$$

$$y_{ij}^\nu = \begin{pmatrix} -0.90 - 0.10i & 0 & 0 \\ 0 & 0.92 - 0.02i & -7.24 + 5.03i \\ 0 & 1.93 - 1.27i & 11.99 - 0.26i \end{pmatrix}, \quad (46)$$

These results are obtained for $\chi_{\text{min}}^2 = 28.5$.

For the scenario in which, $\{n_1, n_2, n_3, n_4, n_5, n_6, n_7\} = \{4, 6, 8, 4, 4, 6, 2\}$, the fit results are as follows,

$$\begin{aligned} N_{\text{TC}} = 9, N_{\text{DTC}} = 9, N_{\text{D}} = 9, \Lambda_{\text{TC}} = 547.6 \text{ GeV}, \Lambda_{\text{ETC}} = 9 \times 10^6 \text{ GeV}, \Lambda_{\text{DTC}} = 500 \text{ GeV}, \Lambda_{\text{EDTC}} = 510 \text{ GeV}, \\ \Lambda = 500 \text{ GeV}, \Lambda_{\text{GUT}} = 2 \times 10^{16} \text{ GeV}, k_{\text{TC}} = 1.08, k_{\text{DTC}} = 0.089, k_{\text{D}} = 6.68. \end{aligned} \quad (47)$$

The dimensionless couplings $y_{ij}^{u,d}$ are,

$$y_{ij}^u = \begin{pmatrix} 0.09 + 0.06i & 0 & -0.81 - 0.63i \\ 0 & -0.93 - 0.98i & 7.06 - 4.41i \\ 0 & 8.89 - 7.17i & -1.73 + 6.86i \end{pmatrix}, \quad (48)$$

$$y_{ij}^d = \begin{pmatrix} -2.35 - 8.50i & 1.94 + 1.70i & 0.49 + 1.09i \\ 8.50 - 1.55i & -8.16 - 7.96i & 7.80 - 4.65i \\ -8.52 + 0.11i & -5.59 - 4.43i & 4.33 - 6.72i \end{pmatrix}, \quad (49)$$

The dimensionless couplings $y_{ij}^{\ell,\nu}$ are,

$$y_{ij}^\ell = \begin{pmatrix} 1 + 7.48 \times 10^{-8}i & 1 & 1 \\ 0 & -1.0 - 0.45i & 1 \\ 0 & 0 & -1.10 - 0.06i \end{pmatrix}, \quad (50)$$

$$y_{ij}^\nu = \begin{pmatrix} 1.33 - 1.22i & 0 & 0 \\ 0 & -0.32 + 0.90i & -0.85 + 1.90i \\ 0 & -4.82 + 10.99i & 11.95 - 0.84i \end{pmatrix}, \quad (51)$$

In this case, we have $\chi_{\min}^2 = 18.0$.

For the case, where the number of fermions in the multifermion DTC condensates are $\{n_1, n_2, n_3, n_4, n_5, n_6, n_7\} = \{6, 8, 10, 6, 6, 8, 2\}$, the obtained fit results are as follows,

$$\begin{aligned} N_{\text{TC}} = 2, N_{\text{DTC}} = 2, N_{\text{D}} = 3, \Lambda_{\text{TC}} = 529.12 \text{ GeV}, \Lambda_{\text{ETC}} = 1.21 \times 10^6 \text{ GeV}, \Lambda_{\text{DTC}} = 500 \text{ GeV}, \Lambda_{\text{EDTC}} = 510 \text{ GeV}, \\ \Lambda = 500 \text{ GeV}, \Lambda_{\text{GUT}} = 2 \times 10^{16} \text{ GeV}, k_{\text{TC}} = 1.07, k_{\text{DTC}} = 0.12, k_{\text{D}} = 7.17. \end{aligned} \quad (52)$$

The dimensionless couplings $y_{ij}^{u,d}$ are,

$$y_{ij}^u = \begin{pmatrix} -0.13 - 0.05i & 0 & 1.21 + 2.13i \\ 0 & 2.72 + 1.93i & 0.01 + 4.30i \\ 0 & -9.41 + 1.33i & 4.15 + 3.51i \end{pmatrix}, \quad (53)$$

$$y_{ij}^d = \begin{pmatrix} 3.11 - 0.62i & 0.86 - 2.38i & 0.83 + 0.23i \\ -3.13 + 3.48i & -3.0 + 10.75i & 3.18 - 11.29i \\ 2.98 + 2.42i & -0.49 + 5.15i & 3.70 - 9.80i \end{pmatrix}, \quad (54)$$

The dimensionless couplings $y_{ij}^{\ell,\nu}$ are,

$$y_{ij}^\ell = \begin{pmatrix} -0.54 - 0.84i & 1 & 1 \\ 0 & 0.35 + 1.05i & 1 \\ 0 & 0 & -0.37 + 1.03i \end{pmatrix}, \quad (55)$$

$$y_{ij}^\nu = \begin{pmatrix} 0.23 + 0.92i & 0 & 0 \\ 0 & 0.92 - 0.02i & 0.93 - 0.01i \\ 0 & 11.06 + 4.66i & 0.41 - 8.96i \end{pmatrix}, \quad (56)$$

and $\chi_{\min}^2 = 11.7$.

4.2.2 $\Lambda > \Lambda_{\text{DTC}}$

In this case, we have set the values of scales as follows,

$$\Lambda_{\text{ETC}} = 10^7 \text{ GeV}, \Lambda_{\text{DTC}} = 500 \text{ GeV}, \Lambda_{\text{EDTC}} = 510 \text{ GeV}, \Lambda = 1 \text{ TeV}. \quad (57)$$

In the scenario where $\{n_1, n_2, n_3, n_4, n_5, n_6, n_7\} = \{2, 4, 6, 2, 2, 4, 2\}$, the fit results are,

$$N_{\text{TC}} = 10, N_{\text{DTC}} = 18, N_{\text{D}} = 3, \Lambda_{\text{TC}} = 894 \text{ GeV}, \Lambda_{\text{GUT}} = 2 \times 10^{16} \text{ GeV}, k_{\text{TC}} = 1.33, \quad (58)$$

$$k_{\text{DTC}} = 0.16, k_{\text{D}} = 6.70. \quad (59)$$

The dimensionless couplings $y_{ij}^{u,d}$ are,

$$y_{ij}^u = \begin{pmatrix} 0.06 - 0.11i & 0 & -2.10 - 7.00i \\ 0 & -3.26 - 0.01i & 3.35 + 6.68i \\ 0 & -10.60 - 2.40i & 2.41 + 3.55i \end{pmatrix}, \quad (60)$$

$$y_{ij}^d = \begin{pmatrix} -0.86 + 1.93i & -1.48 - 0.95i & -0.89 - 1.57i \\ -6.21 + 1.04i & 4.00 + 6.66i & -10.33 - 1.34i \\ 5.17 - 3.90i & 2.50 - 3.44i & 8.69 + 6.63i \end{pmatrix}, \quad (61)$$

The dimensionless couplings $y_{ij}^{\ell,\nu}$ are,

$$y_{ij}^\ell = \begin{pmatrix} 1.0 + 0.i & 1 & 1 \\ 0 & 1.1 + 0.i & 1 \\ 0 & 0 & 1.1 - 2.69 \times 10^{-16}i \end{pmatrix}, \quad (62)$$

$$y_{ij}^\nu = \begin{pmatrix} 2.46 + 2.61i & 0 & 0 \\ 0 & -3.76 - 1.23i & -0.57 + 1.05i \\ 0 & -5.98 + 3.31i & 10.70 - 4.43i \end{pmatrix}, \quad (63)$$

and $\chi_{\text{min}}^2 = 7.7$.

For the scenario in which $\{n_1, n_2, n_3, n_4, n_5, n_6, n_7\} = \{4, 6, 8, 4, 4, 6, 2\}$, the fit results are as follows,

$$N_{\text{TC}} = 10, N_{\text{DTC}} = 18, N_{\text{D}} = 4, \Lambda_{\text{TC}} = 642 \text{ GeV}, \Lambda_{\text{GUT}} = 2 \times 10^{16} \text{ GeV}, k_{\text{TC}} = 1.17, \quad (64)$$

$$k_{\text{DTC}} = 0.09, k_{\text{D}} = 6.56. \quad (65)$$

The dimensionless couplings $y_{ij}^{u,d}$ are,

$$y_{ij}^u = \begin{pmatrix} -0.02 + 0.11i & 0 & 2.60 + 1.62i \\ 0 & 1.19 - 0.50i & 2.54 + 1.09i \\ 0 & 7.02 + 9.24i & 6.12 - 3.56i \end{pmatrix}, \quad (66)$$

$$y_{ij}^d = \begin{pmatrix} 0.26 + 3.88i & 1.43 - 0.58i & 1.69 - 0.59i \\ -7.87 + 8.50i & -2.63 + 6.28i & 8.23 + 4.17i \\ 10.39 + 5.39i & 1.31 + 1.96i & 3.99 - 7.13i \end{pmatrix}, \quad (67)$$

The dimensionless couplings $y_{ij}^{\ell,\nu}$ are,

$$y_{ij}^\ell = \begin{pmatrix} -0.73 - 0.69i & 1 & 1 \\ 0 & 1.1 - 1.02 \times 10^{-7}i & 1 \\ 0 & 0 & 1.1 - 7.76 \times 10^{-7}i \end{pmatrix}, \quad (68)$$

$$y_{ij}^\nu = \begin{pmatrix} -1.11 - 0.49i & 0 & 0 \\ 0 & -1.429 - 0.019i & 4.86 - 2.22i \\ 0 & -1.95 + 0.22i & -9.07 - 4.84i \end{pmatrix}, \quad (69)$$

for $\chi_{\text{min}}^2 = 20.6$.

In the case where the number of fermions in the multifermion DTC condensates are $\{n_1, n_2, n_3, n_4, n_5, n_6, n_7\} = \{6, 8, 10, 6, 6, 8, 2\}$, the obtained fit results are as follows,

$$N_{\text{TC}} = 12, N_{\text{DTC}} = 17, N_{\text{D}} = 15, \Lambda_{\text{TC}} = 296 \text{ GeV}, \Lambda_{\text{GUT}} = 2 \times 10^{16} \text{ GeV}, k_{\text{TC}} = 0.77, \quad (70)$$

$$k_{\text{DTC}} = 0.04, k_{\text{D}} = 6.87. \quad (71)$$

The dimensionless couplings $y_{ij}^{u,d}$ are,

$$y_{ij}^u = \begin{pmatrix} -0.05 + 0.12i & 0 & 0.68 + 0.49i \\ 0 & 0.04 + 2.41i & -3.25 - 1.57i \\ 0 & -7.53 + 8.46i & 7.06 - 8.37i \end{pmatrix}, \quad (72)$$

$$y_{ij}^d = \begin{pmatrix} 1.60 + 0.88i & -1.34 - 0.94i & -0.44 - 0.56i \\ 0.94 + 0.57i & -6.50 + 3.15i & -11.61 + 0.75i \\ 5.61 - 4.03i & 1.20 + 0.29i & 8.51 + 2.62i \end{pmatrix}, \quad (73)$$

The dimensionless couplings $y_{ij}^{\ell,\nu}$ are,

$$y_{ij}^\ell = \begin{pmatrix} 0.72 - 0.69i & 1 & 1 \\ 0 & 1.1 + 3.74 \times 10^{-8}i & 1 \\ 0 & 0 & 1.1 - 6.09 \times 10^{-7}i \end{pmatrix}, \quad (74)$$

$$y_{ij}^\nu = \begin{pmatrix} -1.32 + 0.94i & 0 & 0 \\ 0 & 4.71 - 2.10 \times 10^{-5}i & -5.66 - 2.43i \\ 0 & -4.01 + 5.28i & 5.01 - 8.30i \end{pmatrix}, \quad (75)$$

and $\chi_{\min}^2 = 6.4$.

4.2.3 $\Lambda < \Lambda_{DTC}$

For this case we have set the values of scales as follows,

$$\Lambda_{\text{ETC}} = 10^7 \text{ GeV}, \Lambda_{\text{DTC}} = 1 \text{ TeV}, \Lambda_{\text{EDTC}} = 1.1 \text{ TeV}, \Lambda = 500 \text{ GeV} \quad (76)$$

For the number of fermions in the multifermion DTC condensates $\{n_1, n_2, n_3, n_4, n_5, n_6, n_7\} = \{2, 4, 6, 2, 2, 4, 2\}$, the fit results are,

$$N_{\text{TC}} = 16, N_{\text{DTC}} = 12, N_{\text{D}} = 8, \Lambda_{\text{TC}} = 605.8 \text{ GeV}, \Lambda_{\text{GUT}} = 2 \times 10^{16} \text{ GeV}, k_{\text{TC}} = 1.14, \quad (77)$$

$$k_{\text{DTC}} = 0.16, k_{\text{D}} = 6.45. \quad (78)$$

The dimensionless couplings $y_{ij}^{u,d}$ are,

$$y_{ij}^u = \begin{pmatrix} -0.07 + 0.10i & 0 & 2.32 - 0.20i \\ 0 & 1.60 - 1.59i & 2.96 + 2.79i \\ 0 & 10.39 + 1.83i & 1.78 + 0.15i \end{pmatrix}, \quad (79)$$

$$y_{ij}^d = \begin{pmatrix} -0.76 + 3.63i & -2.63 + 0.01i & 0.79 + 0.44i \\ 0.42 - 2.88i & -10.93 + 3.87i & 10.61 + 2.22i \\ -4.40 - 10.14i & -3.20 + 2.52i & 7.13 - 0.86i \end{pmatrix}. \quad (80)$$

The dimensionless couplings $y_{ij}^{\ell,\nu}$ are,

$$y_{ij}^\ell = \begin{pmatrix} 0.27 - 0.96i & 1 & 1 \\ 0 & -0.16 - 1.09i & 1 \\ 0 & 0 & 0.68 - 0.86i \end{pmatrix}, \quad (81)$$

$$y_{ij}^\nu = \begin{pmatrix} 1.50 - 0.96i & 0 & 0 \\ 0 & 2.83 - 1.26i & 0.79 - 1.47i \\ 0 & 10.85 + 4.83i & 8.13 + 7.81i \end{pmatrix}. \quad (82)$$

These results are obtained for $\chi_{\min}^2 = 11.5$.

For the scenario in which $\{n_1, n_2, n_3, n_4, n_5, n_6, n_7\} = \{4, 6, 8, 4, 4, 6, 2\}$, the fit results are as follows,

$$N_{\text{TC}} = 14, N_{\text{DTC}} = 6, N_{\text{D}} = 12, \Lambda_{\text{TC}} = 513 \text{ GeV}, \Lambda_{\text{GUT}} = 2 \times 10^{16} \text{ GeV}, k_{\text{TC}} = 1.05, \quad (83)$$

$$k_{\text{DTC}} = 0.089, k_{\text{D}} = 6.21. \quad (84)$$

The dimensionless couplings $y_{ij}^{u,d}$ are,

$$y_{ij}^u = \begin{pmatrix} -0.01 + 0.11i & 0 & 0.72 - 4.34i \\ 0 & 1.97 - 2.36i & 1.70 - 2.44i \\ 0 & 6.61 - 7.88i & 1.83 + 10.60i \end{pmatrix}, \quad (85)$$

$$y_{ij}^d = \begin{pmatrix} -0.09 + 3.53i & -2.15 + 0.42i & 1.20 + 1.14i \\ -3.98 - 10.31i & 4.89 - 8.34i & 4.58 + 7.98i \\ 8.87 - 6.73i & 9.16 + 4.86i & -10.14 + 0.79i \end{pmatrix}. \quad (86)$$

The dimensionless couplings $y_{ij}^{\ell,\nu}$ are,

$$y_{ij}^{\ell} = \begin{pmatrix} -0.69 + 0.72i & 1 & 1 \\ 0 & -0.66 - 0.88i & 1 \\ 0 & 0 & -0.74 - 0.82i \end{pmatrix}, \quad (87)$$

$$y_{ij}^{\nu} = \begin{pmatrix} -0.74 - 0.52i & 0 & 0 \\ 0 & -0.66 - 1.05i & -1.31 + 8.58i \\ 0 & -2.11 + 1.56i & -0.64 + 11.98i \end{pmatrix}, \quad (88)$$

with $\chi_{\text{min}}^2 = 15.1$.

For the case where the number of fermions in the multifermion DTC condensates are $\{n_1, n_2, n_3, n_4, n_5, n_6, n_7\} = \{6, 8, 10, 6, 6, 8, 2\}$, the obtained fit results are as follows,

$$N_{\text{TC}} = 8, N_{\text{DTC}} = 4, N_{\text{D}} = 9, \Lambda_{\text{TC}} = 422 \text{ GeV}, \Lambda_{\text{GUT}} = 2 \times 10^{16} \text{ GeV}, k_{\text{TC}} = 0.95, \quad (89)$$

$$k_{\text{DTC}} = 0.10, k_{\text{D}} = 6.41. \quad (90)$$

The dimensionless couplings $y_{ij}^{u,d}$ are,

$$y_{ij}^u = \begin{pmatrix} -0.01 + 0.11i & 0 & 0.72 - 4.34i \\ 0 & 1.97 - 2.36i & 1.70 - 2.44i \\ 0 & 6.61 - 7.88i & 1.83 + 10.60i \end{pmatrix}, \quad (91)$$

$$y_{ij}^d = \begin{pmatrix} -0.09 + 3.53i & -2.15 + 0.425i & 1.20 + 1.14i \\ -3.98 - 10.31i & 4.89 - 8.34i & 4.58 + 7.98i \\ 8.87 - 6.73i & 9.16 + 4.86i & -10.14 + 0.79i \end{pmatrix}. \quad (92)$$

The dimensionless couplings $y_{ij}^{\ell,\nu}$ are,

$$y_{ij}^{\ell} = \begin{pmatrix} -0.99 + 0.10i & 1 & 1 \\ 0 & 0.51 - 0.98i & 1 \\ 0 & 0 & 1.1 - 9.67 \times 10^{-8}i \end{pmatrix}, \quad (93)$$

$$y_{ij}^{\nu} = \begin{pmatrix} 0.05 - 0.90i & 0 & 0 \\ 0 & 2.06 + 0.60i & 3.83 - 3.61i \\ 0 & 0.39 + 0.81i & 5.09 - 8.95i \end{pmatrix}. \quad (94)$$

where $\chi_{\text{min}}^2 = 10.1$. For all scenarios, we obtain quark and leptonic Dirac CP phases as $\delta_{\text{CP}}^q \approx 1.144$ and $\delta_{\text{CP}}^{\ell} \approx 3.14$.

4.3 The FN mechanism based on the $\mathcal{Z}_N \times \mathcal{Z}_M$ flavour symmetry

The other possible low-energy limit of the DTC paradigm could be the FN mechanism based on the $\mathcal{Z}_N \times \mathcal{Z}_M$ flavour symmetry [26]. This is extensively discussed in [36, 37, 38]. To show the FN mechanism based on the $\mathcal{Z}_N \times \mathcal{Z}_M$ flavour symmetry as a possible low energy limit of the DTC paradigm, we use a model which can provide a unified solution to the flavour problem and dark matter through the emergence of flavonic dark matter, a new class of scalar dark matter [37].

This model is based on the $\mathcal{Z}_8 \times \mathcal{Z}_{22}$ flavour symmetry, where the mass of the top quark arises through the dimension-5 operator. As will be shown in the next subsection, this model can be easily accommodated within the DTC paradigm. We show the transformation of the SM and the flavon field, χ , under the $\mathcal{Z}_8 \times \mathcal{Z}_{22}$ flavour symmetry in table 2.

Fields	\mathcal{Z}_8	\mathcal{Z}_{22}	Fields	\mathcal{Z}_8	\mathcal{Z}_{22}	Fields	\mathcal{Z}_8	\mathcal{Z}_{22}	Fields	\mathcal{Z}_8	\mathcal{Z}_{22}	Fields	\mathcal{Z}_8	\mathcal{Z}_{22}
u_R	ω^2	ω'^2	c_R	ω^5	ω'^5	t_R	ω^6	ω'^6	d_R	ω^3	ω'^3	s_R	ω^4	ω'^4
b_R	ω^4	ω'^4	$\psi_{L,1}^q$	ω^2	ω'^{10}	$\psi_{L,2}^q$	ω	ω'^9	$\psi_{L,3}^q$	ω^7	ω'^7	$\psi_{L,1}^\ell$	ω^3	ω'^3
$\psi_{L,2}^\ell$	ω^2	ω'^2	$\psi_{L,3}^\ell$	ω^2	ω'^2	e_R	ω^2	ω'^{16}	μ_R	ω^5	ω'^{19}	τ_R	ω^7	ω'^{21}
ν_{e_R}	ω^2	1	ν_{μ_R}	ω^5	ω'^3	ν_{τ_R}	ω^6	ω'^4	χ	ω	ω'	φ	1	1

Table 2: The charges of the SM as well as the flavon field under the $\mathcal{Z}_8 \times \mathcal{Z}_{22}$ symmetry, where ω denotes the 8th, and ω' denotes the 22th root of unity respectively.

The mass Lagrangian for the charged fermions originate from the Lagrangian produced by the $\mathcal{Z}_8 \times \mathcal{Z}_{22}$ flavour symmetry,

$$\begin{aligned}
-\mathcal{L}_{\text{Yukawa}} = & \left(\frac{\chi}{\Lambda}\right)^8 y_{11}^u \bar{\psi}_{L_1}^q \tilde{\varphi} u_R + \left(\frac{\chi}{\Lambda}\right)^5 y_{12}^u \bar{\psi}_{L_1}^q \tilde{\varphi} c_R + \left(\frac{\chi}{\Lambda}\right)^4 y_{13}^u \bar{\psi}_{L_1}^q \tilde{\varphi} t_R + \left(\frac{\chi}{\Lambda}\right)^7 y_{21}^u \bar{\psi}_{L_2}^q \tilde{\varphi} u_R \\
& + \left(\frac{\chi}{\Lambda}\right)^4 y_{22}^u \bar{\psi}_{L_2}^q \tilde{\varphi} c_R + \left(\frac{\chi}{\Lambda}\right)^3 y_{23}^u \bar{\psi}_{L_2}^q \tilde{\varphi} t_R + \left(\frac{\chi}{\Lambda}\right)^5 y_{31}^u \bar{\psi}_{L_3}^q \tilde{\varphi} u_R + \left(\frac{\chi}{\Lambda}\right)^2 y_{32}^u \bar{\psi}_{L_3}^q \tilde{\varphi} c_R \\
& + \left(\frac{\chi}{\Lambda}\right) y_{33}^u \bar{\psi}_{L_3}^q \tilde{\varphi} t_R + \left(\frac{\chi}{\Lambda}\right)^7 y_{11}^d \bar{\psi}_{L_1}^q \varphi d_R + \left(\frac{\chi}{\Lambda}\right)^6 y_{12}^d \bar{\psi}_{L_1}^q \varphi s_R + \left(\frac{\chi}{\Lambda}\right)^6 y_{13}^d \bar{\psi}_{L_1}^q \varphi b_R + \left(\frac{\chi}{\Lambda}\right)^6 y_{21}^d \bar{\psi}_{L_2}^q \varphi d_R \\
& + \left(\frac{\chi}{\Lambda}\right)^5 y_{22}^d \bar{\psi}_{L_2}^q \varphi s_R + \left(\frac{\chi}{\Lambda}\right)^5 y_{23}^d \bar{\psi}_{L_2}^q \varphi b_R + \left(\frac{\chi}{\Lambda}\right)^4 y_{31}^d \bar{\psi}_{L_3}^q \varphi d_R + \left(\frac{\chi}{\Lambda}\right)^3 y_{32}^d \bar{\psi}_{L_3}^q \varphi s_R \\
& + \left(\frac{\chi}{\Lambda}\right)^3 y_{33}^d \bar{\psi}_{L_3}^q \varphi b_R + \left(\frac{\chi}{\Lambda}\right)^9 y_{11}^\ell \bar{\psi}_{L_1}^\ell \varphi e_R + \left(\frac{\chi}{\Lambda}\right)^6 y_{12}^\ell \bar{\psi}_{L_1}^\ell \varphi \mu_R + \left(\frac{\chi}{\Lambda}\right)^4 y_{13}^\ell \bar{\psi}_{L_1}^\ell \varphi \tau_R \\
& + \left(\frac{\chi}{\Lambda}\right)^8 y_{21}^\ell \bar{\psi}_{L_2}^\ell \varphi e_R + \left(\frac{\chi}{\Lambda}\right)^5 y_{22}^\ell \bar{\psi}_{L_2}^\ell \varphi \mu_R + \left(\frac{\chi}{\Lambda}\right)^3 y_{23}^\ell \bar{\psi}_{L_2}^\ell \varphi \tau_R + \left(\frac{\chi}{\Lambda}\right)^8 y_{31}^\ell \bar{\psi}_{L_3}^\ell \varphi e_R \\
& + \left(\frac{\chi}{\Lambda}\right)^5 y_{32}^\ell \bar{\psi}_{L_3}^\ell \varphi \mu_R + \left(\frac{\chi}{\Lambda}\right)^3 y_{33}^\ell \bar{\psi}_{L_3}^\ell \varphi \tau_R + \text{H.c.},
\end{aligned}$$

where $\epsilon = \langle \chi \rangle / \Lambda < 1$.

The mass matrices of the charged fermions are given as,

$$\mathcal{M}_u = \frac{v}{\sqrt{2}} \begin{pmatrix} y_{11}^u \epsilon^8 & y_{12}^u \epsilon^5 & y_{13}^u \epsilon^4 \\ y_{21}^u \epsilon^7 & y_{22}^u \epsilon^4 & y_{23}^u \epsilon^3 \\ y_{31}^u \epsilon^5 & y_{32}^u \epsilon^2 & y_{33}^u \epsilon \end{pmatrix}, \mathcal{M}_d = \frac{v}{\sqrt{2}} \begin{pmatrix} y_{11}^d \epsilon^7 & y_{12}^d \epsilon^6 & y_{13}^d \epsilon^6 \\ y_{21}^d \epsilon^6 & y_{22}^d \epsilon^5 & y_{23}^d \epsilon^5 \\ y_{31}^d \epsilon^4 & y_{32}^d \epsilon^3 & y_{33}^d \epsilon^3 \end{pmatrix}, \mathcal{M}_\ell = \frac{v}{\sqrt{2}} \begin{pmatrix} y_{11}^\ell \epsilon^9 & y_{12}^\ell \epsilon^4 & y_{13}^\ell \epsilon^4 \\ y_{21}^\ell \epsilon^{10} & y_{22}^\ell \epsilon^5 & y_{23}^\ell \epsilon^3 \\ y_{31}^\ell \epsilon^8 & y_{32}^\ell \epsilon^5 & y_{33}^\ell \epsilon^3 \end{pmatrix}. \quad (95)$$

The masses of charged fermions can be written as,

$$\{m_t, m_c, m_u\} \simeq \{|y_{33}^u| \epsilon, \left| y_{22}^u - \frac{y_{23}^u y_{32}^u}{y_{33}^u} \right| \epsilon^4, \quad (96)$$

$$\left| y_{11}^u - \frac{y_{12}^u y_{21}^u}{y_{22}^u - y_{23}^u y_{32}^u / y_{33}^u} - \frac{y_{13}^u (y_{31}^u y_{22}^u - y_{21}^u y_{32}^u) - y_{31}^u y_{12}^u y_{23}^u}{(y_{22}^u - y_{23}^u y_{32}^u / y_{33}^u) y_{33}^u} \right| \epsilon^8 \} v / \sqrt{2},$$

$$\{m_b, m_s, m_d\} \simeq \{ |y_{33}^d| \epsilon^3, \left| y_{22}^d - \frac{y_{23}^d y_{32}^d}{y_{33}^d} \right| \epsilon^5, \quad (97)$$

$$\left| y_{11}^d - \frac{y_{12}^d y_{21}^d}{y_{22}^d - y_{23}^d y_{32}^d / y_{33}^d} - \frac{y_{13}^d (y_{31}^d y_{22}^d - y_{21}^d y_{32}^d) - y_{31}^d y_{12}^d y_{23}^d}{(y_{22}^d - y_{23}^d y_{32}^d / y_{33}^d) y_{33}^d} \right| \epsilon^7 \} v / \sqrt{2},$$

$$\{m_\tau, m_\mu, m_e\} \simeq \{ |y_{33}^l| \epsilon^3, \left| y_{22}^l - \frac{y_{23}^l y_{32}^l}{y_{33}^l} \right| \epsilon^5,$$

$$\left| y_{11}^l - \frac{y_{12}^l y_{21}^l}{y_{22}^l - y_{23}^l y_{32}^l / y_{33}^l} - \frac{y_{13}^l (y_{31}^l y_{22}^l - y_{21}^l y_{32}^l) - y_{31}^l y_{12}^l y_{23}^l}{(y_{22}^l - y_{23}^l y_{32}^l / y_{33}^l) y_{33}^l} \right| \epsilon^9 \} v / \sqrt{2}. \quad (98)$$

The quark mixing angles are,

$$\sin \theta_{12} \simeq |V_{us}| \simeq \left| \frac{y_{12}^d}{y_{22}^d} - \frac{y_{12}^u}{y_{22}^u} \right| \epsilon, \quad \sin \theta_{23} \simeq |V_{cb}| \simeq \left| \frac{y_{23}^d}{y_{33}^d} - \frac{y_{23}^u}{y_{33}^u} \right| \epsilon^2, \quad \sin \theta_{13} \simeq |V_{ub}| \simeq \left| \frac{y_{13}^d}{y_{33}^d} - \frac{y_{12}^u y_{23}^d}{y_{22}^u y_{33}^d} - \frac{y_{13}^u}{y_{33}^u} \right| \epsilon^3. \quad (99)$$

We obtain Dirac neutrino masses by adding three right handed neutrinos $\nu_{eR}, \nu_{\mu R}, \nu_{\tau R}$ to the SM, and writing the Lagrangian,

$$-\mathcal{L}_{\text{Yukawa}}^\nu = y_{ij}^\nu \bar{\psi}_{L_i}^\ell \tilde{H} \nu_{R_j} \left[\frac{\chi}{\Lambda} \right]^{n_{ij}^\nu} + \text{H.c.} \quad (100)$$

The Dirac mass matrix for neutrinos is given as,

$$\mathcal{M}_{\mathcal{D}} = \frac{v}{\sqrt{2}} \begin{pmatrix} y_{11}^\nu \epsilon^{25} & y_{12}^\nu \epsilon^{22} & y_{13}^\nu \epsilon^{21} \\ y_{21}^\nu \epsilon^{24} & y_{22}^\nu \epsilon^{21} & y_{23}^\nu \epsilon^{20} \\ y_{31}^\nu \epsilon^{24} & y_{32}^\nu \epsilon^{21} & y_{33}^\nu \epsilon^{20} \end{pmatrix}. \quad (101)$$

We obtain the masses with normal hierarchy,

$$\{m_3, m_2, m_1\} \simeq \{ |y_{33}^\nu| \epsilon^{20}, \left| y_{22}^\nu - \frac{y_{23}^\nu y_{32}^\nu}{y_{33}^\nu} \right| \epsilon^{21}, \quad (102)$$

$$\left| y_{11}^\nu - \frac{y_{12}^\nu y_{21}^\nu}{y_{22}^\nu - y_{23}^\nu y_{32}^\nu / y_{33}^\nu} - \frac{y_{13}^\nu (y_{31}^\nu y_{22}^\nu - y_{21}^\nu y_{32}^\nu) - y_{31}^\nu y_{12}^\nu y_{23}^\nu}{(y_{22}^\nu - y_{23}^\nu y_{32}^\nu / y_{33}^\nu) y_{33}^\nu} \right| \epsilon^{25} \} v / \sqrt{2}.$$

The leptonic mixing angles turn out to be,

$$\sin \theta_{12} \simeq \left| \frac{y_{12}^\ell}{y_{22}^\ell} - \frac{y_{12}^\nu}{y_{22}^\nu} \right| \epsilon, \quad \sin \theta_{23} \simeq \left| \frac{y_{23}^\ell}{y_{33}^\ell} - \frac{y_{23}^\nu}{y_{33}^\nu} \right|, \quad \sin \theta_{13} \simeq \left| \frac{y_{13}^\ell}{y_{33}^\ell} - \frac{y_{12}^\nu y_{23}^\ell}{y_{22}^\nu y_{33}^\ell} - \frac{y_{13}^\nu}{y_{33}^\nu} \right| \epsilon. \quad (103)$$

4.4 The FN mechanism based on the $\mathcal{Z}_N \times \mathcal{Z}_M$ flavour symmetry within the DTC-paradigm

The FN mechanism based on the $\mathcal{Z}_N \times \mathcal{Z}_M$ flavour symmetry can be implemented within the framework of the DTC paradigm. The interactions required to generate charged fermion mass matrices are shown in the upper part of figure 4. In the lower part of the figure, we show the generic FN mechanism of generating fermion masses, where $\langle \varphi \rangle$ and $\langle \chi \rangle$ are the chiral condensates acting like the VEVs of the Higgs and flavon fields.

The mass matrices corresponding to equations 95 and 101 in the FN mechanism can be recovered from

$$\mathcal{M}_f = |y_{ij}^f| \frac{N_{\text{TC}}}{2\pi^2} \frac{\Lambda_{\text{TC}}^2}{\Lambda_{\text{ETC}}} \left(\frac{1}{\Lambda} \frac{N_{\text{DTC}}}{4\pi^2} \frac{\Lambda_{\text{DTC}}^3}{\Lambda_{\text{EDTC}}^2} \exp(2k) \right)^{n_{ij}^f}, \quad (104)$$

where $f = u, d, \ell, \nu$, and the order parameter ϵ can be written as,

$$\epsilon \propto \frac{1}{\Lambda} \frac{N_{\text{DTC}}}{4\pi^2} \frac{\Lambda_{\text{DTC}}^3}{\Lambda_{\text{EDTC}}^2} \exp(2k), \quad (105)$$

and the SM Higgs VEV may be identified with,

$$\langle \varphi \rangle \propto \frac{N_{\text{TC}}}{2\pi^2} \frac{\Lambda_{\text{TC}}^2}{\Lambda_{\text{ETC}}}. \quad (106)$$

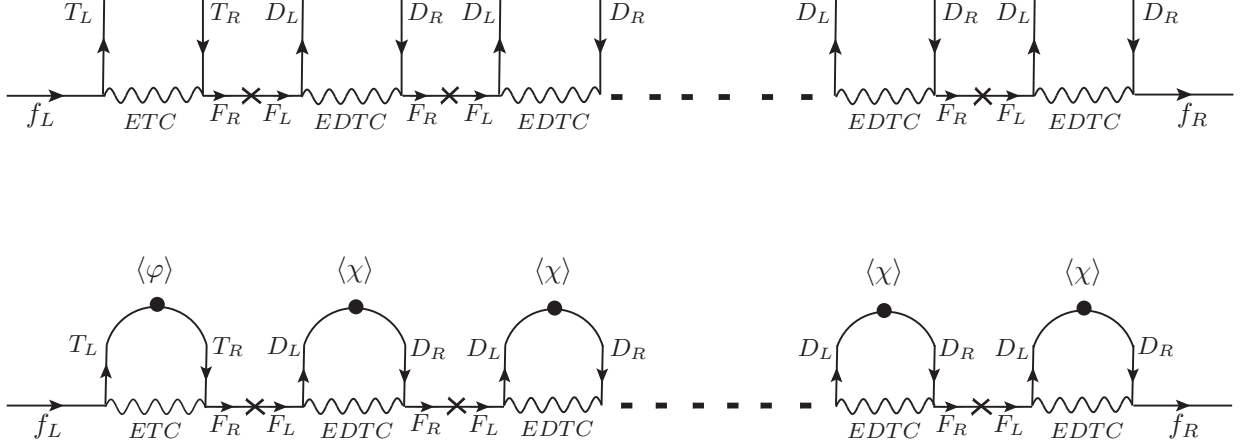


Figure 4: Feynman diagrams for the masses of the quarks and charged leptons in the DTC paradigm. On the top, the generic interactions of the SM, TC, DQCD and DTC fermions are shown. In the bottom, we see the formations of the condensate (circular blob), and the resulting masses of the SM fermions.

We perform the fitting of fermionic masses and mixing in three scenarios. Moreover, we are not able to reproduce the neutrino masses and mixing within the framework of the FN mechanism.

4.4.1 $\Lambda \approx \Lambda_{\text{DTC}}$

The dimensionless coefficients $y_{ij}^{u,d} = |y_{ij}^{u,d}| e^{i\phi_{ij}^q}$ are scanned in the range $|y_{ij}^{u,d}| \in [0.1, 4\pi]$ and $\phi_{ij}^q \in [0, 2\pi]$. The fit results are,

$$\begin{aligned} N_{\text{TC}} = 4, N_{\text{DTC}} = 3, N_{\text{D}} = 2, \Lambda_{\text{TC}} = 5.4 \text{ TeV}, \Lambda_{\text{ETC}} = 1 \times 10^7 \text{ GeV}, \Lambda_{\text{DTC}} = 500 \text{ GeV}, \Lambda_{\text{EDTC}} = 510 \text{ GeV}, \\ \Lambda = 500 \text{ GeV}, k_{\text{TC}} = 2.23, k_{\text{DTC}} = 0.004. \end{aligned} \quad (107)$$

The dimensionless couplings $y_{ij}^{u,d}$ are,

$$y_{ij}^u = \begin{pmatrix} -1.63 - 4.80i & -3.57 + 11.30i & 11.08 + 0.80i \\ 0.37 + 0.03i & 2.49 - 11.49i & 8.24 - 5.25i \\ 2.11 - 11.79i & -0.39 + 6.05i & 0.84 + 9.70i \end{pmatrix}, \quad (108)$$

$$y_{ij}^d = \begin{pmatrix} 0.16 - 0.01i & 0.61 - 7.18i & 8.65 + 8.25i \\ 8.67 + 1.25i & -3.83 + 1.98i & 0.68 - 7.26i \\ 3.94 + 0.34i & -2.34 + 2.62i & -6.45 + 2.74i \end{pmatrix}. \quad (109)$$

The dimensionless couplings $y_{ij}^{\ell,\nu}$ are,

$$y_{ij}^{\ell} = \begin{pmatrix} -1.03 - 0.10i & -0.88 - 0.56i & 0.72 - 0.73i \\ 0.98 - 0.20i & -0.81 - 0.75i & -0.09 - 1.10i \\ 1.10 - 5.26 \times 10^{-5}i & -0.81 + 0.75i & 1.1 + 0i \end{pmatrix}. \quad (110)$$

These results are obtained for $\chi_{\text{min}}^2 = 3.1$.

4.4.2 $\Lambda > \Lambda_{DTC}$

For this case we have set the values of scales as follows,

$$\Lambda_{ETC} = 10^7 \text{ GeV}, \Lambda_{DTC} = 500 \text{ GeV}, \Lambda_{EDTC} = 510 \text{ GeV}, \Lambda = 1 \text{ TeV} \quad (111)$$

The fit results are,

$$N_{TC} = 3, N_{DTC} = 5, N_D = 2, \Lambda_{TC} = 5.9 \text{ TeV}, k_{TC} = 2.27, k_{DTC} = 0.04. \quad (112)$$

The dimensionless couplings $y_{ij}^{u,d}$ are,

$$y_{ij}^u = \begin{pmatrix} 1.20 - 7.88i & -0.10 - 6.10i & 11.84 + 0.28i \\ -1.14 - 1.57i & -3.31 - 2.46i & -3.47 + 6.51i \\ 8.63 + 0.i & -9.27 + 6.91i & 7.56 + 1.67i \end{pmatrix}, \quad (113)$$

$$y_{ij}^d = \begin{pmatrix} -8.66 + 1.59i & 0.15 - 0.001i & 0.24 + 4.88i \\ -3.46 - 5.56i & -5.77 + 5.30i & 6.21 + 0.23i \\ -10.48 + 5.60i & 2.93 - 3.50i & -4.17 + 3.57i \end{pmatrix}. \quad (114)$$

The dimensionless couplings $y_{ij}^{\ell,\nu}$ are,

$$y_{ij}^{\ell} = \begin{pmatrix} 1.05 + 0.i & -0.91 - 0.62i & -0.11 - 1.06i \\ -0.62 - 0.81i & 0.95 + 0.56i & -0.32 + 1.05i \\ 1.06 - 4.87 \times 10^{-7}i & -0.89 - 0.65i & -0.43 + 1.01i \end{pmatrix} \quad (115)$$

These results are obtained for $\chi_{\min}^2 = 2.0$.

4.4.3 $\Lambda < \Lambda_{DTC}$

For this case we have set the values of scales as follows:

$$\Lambda_{ETC} = 10^7 \text{ GeV}, \Lambda_{DTC} = 1 \text{ TeV}, \Lambda_{EDTC} = 1.1 \text{ TeV}, \Lambda = 500 \text{ GeV} \quad (116)$$

The fit results are,

$$N_{TC} = 2, N_{DTC} = 3, N_D = 2, \Lambda_{TC} = 5.4 \text{ TeV}, k_{TC} = 2.23, k_{DTC} = 0. \quad (117)$$

The dimensionless couplings $y_{ij}^{u,d}$ are,

$$y_{ij}^u = \begin{pmatrix} 1.93 + 0.33i & -5.29 - 0.64i & 2.66 \times 10^{-4} + 1.16i \\ 0.58 - 0.10i & -0.70 - 4.23i & 1.56 - 2.47i \\ -7.93 - 7.01i & 0.29 - 0.03i & -3.05 - 11.61i \end{pmatrix}, \quad (118)$$

$$y_{ij}^d = \begin{pmatrix} -0.23 + 0.04i & 3.39 - 0.50i & -0.31 + 1.04i \\ 6.60 - 0.03i & 6.49 + 4.23i & -2.69 - 0.70i \\ 6.42 - 5.84i & 8.41 - 1.63i & -2.92 + 1.20i \end{pmatrix}. \quad (119)$$

The dimensionless couplings $y_{ij}^{\ell,\nu}$ are,

$$y_{ij}^{\ell} = \begin{pmatrix} -0.06 + 1.00i & -0.42 + 0.95i & -1.09 + 0.12i \\ 0.70 - 0.72i & 0.66 + 0.86i & -0.91 - 0.60i \\ -0.94 + 0.33i & 1.08 + 0.02i & 1.05 - 0.34i \end{pmatrix}, \quad (120)$$

where $\chi_{\min}^2 = 18.2$.

5 Why not the minimal form of the DTC-paradigm?

A minimal version of the DTC paradigm is discussed in reference [24], which is based on symmetry $\mathcal{G} = \text{SU}(N_{\text{TC}}) \times \text{SU}(N_{\text{D}})$. In this section, we discuss this minimal version of the DTC paradigm in detail and show that it is not theoretically consistent in explaining the flavour structure of the SM.

5.1 The multifermion chiral condensates $\langle \chi_r \rangle$ originate from the TC dynamics

In the first scenario, the multifermions chiral condensates, which play the role of the VEVs $\langle \chi_r \rangle$, are the TC multifermion chiral condensates. This can be done by introducing TC fermions under the $\text{SU}(3)_c \times \text{SU}(2)_L \times \text{U}(1)_Y \times \mathcal{G}$ symmetry as,

$$\begin{aligned} T^i &\equiv \begin{pmatrix} T \\ B \end{pmatrix}_L : (1, 2, 0, N_{\text{TC}}, 1), \quad T_R^i : (1, 1, 1, N_{\text{TC}}, 1), \quad B_R^i : (1, 1, -1, N_{\text{TC}}, 1), \\ D_{L,R} &\equiv C_{i,L,R} : (1, 1, 1, N_{\text{TC}}, 1), \quad S_{i,L,R} : (1, 1, -1, N_{\text{TC}}, 1), \end{aligned} \quad (121)$$

where $i = 1, 2, 3 \dots$, and electric charges $+\frac{1}{2}$ for T and C , and $-\frac{1}{2}$ for B and S .

The $\text{SU}(N_{\text{D}})$ dynamics has vector-like fermions transforming as,

$$\begin{aligned} F_{L,R} &\equiv U_{L,R}^i \equiv (3, 1, \frac{4}{3}, 1, N_{\text{D}}), \quad D_{L,R}^i \equiv (3, 1, -\frac{2}{3}, 1, N_{\text{D}}), \\ N_{L,R}^i &\equiv (1, 1, 0, 1, N_{\text{D}}), \quad E_{L,R}^i \equiv (1, 1, -2, 1, N_{\text{D}}). \end{aligned} \quad (122)$$

We assume that hierarchical VEVs $\langle \chi_r \rangle$ are chiral multifermion condensates of type $\bar{D}_R D_L \dots \bar{D}_R D_L$. For creating fermion masses, we have to assume that all TC fermions (T and D) are accommodated in a common ETC symmetry, and fermionic masses are generated, as shown in figure 5. However, this will allow the interactions between the right-handed SM fermions and the right-handed TC fermions to reduce to the original TC model based only on $\text{SU}(N_{\text{TC}})$ symmetry, which is already excluded by the experimental data.

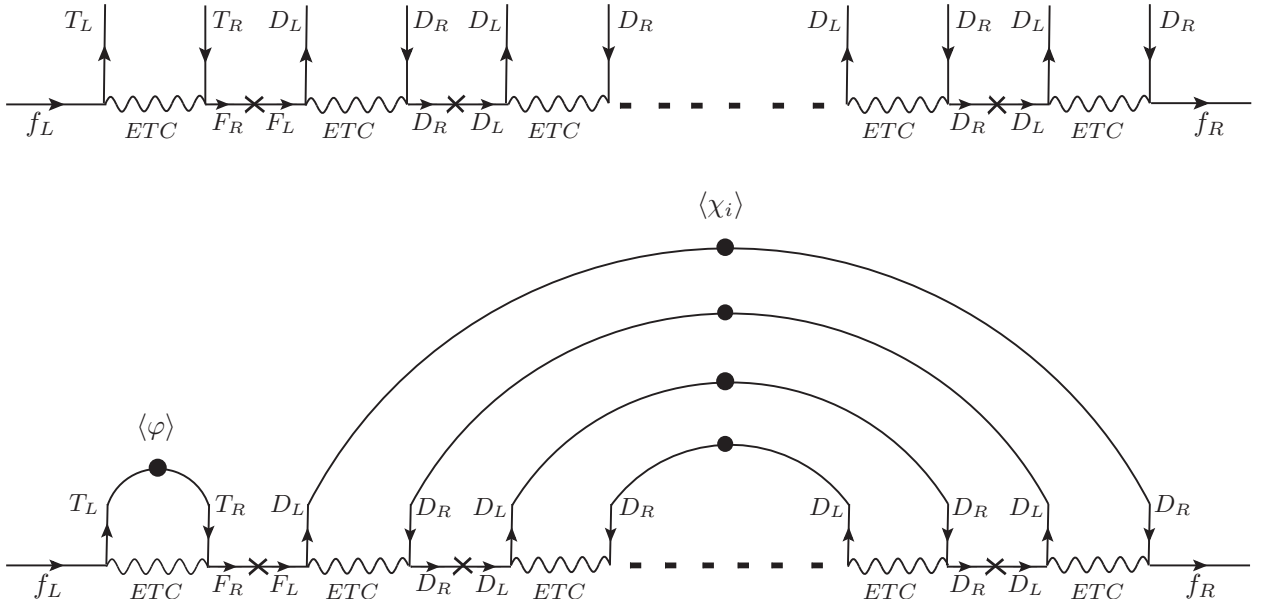


Figure 5: The Feynman diagrams for the masses of the charged fermions in the minimal version of the DTC-paradigm.

5.2 The multifermion chiral condensates $\langle\chi_r\rangle$ originate from the DQCD dynamics

In the second scenario, the multifermion chiral condensates $\langle\chi_r\rangle$ arise from the $SU(N_D)$ dynamics, that is, $\langle\chi_r\rangle = \bar{F}_R F_L \cdots \bar{F}_R F_L$. Apparently, this looks promising and attractive from the point of view of a minimal model.

However, in this scenario, the flavour structure of the SM can only be obtained if the left-handed SM fermions, TC fermions, and right-handed F_R fermions are accommodated in an ETC symmetry and the right-handed SM fermions f_R and left-handed F_L fermions are accommodated in a different EDTC symmetry. This will create interactions and fermion mass generations, as depicted in Figure 6.

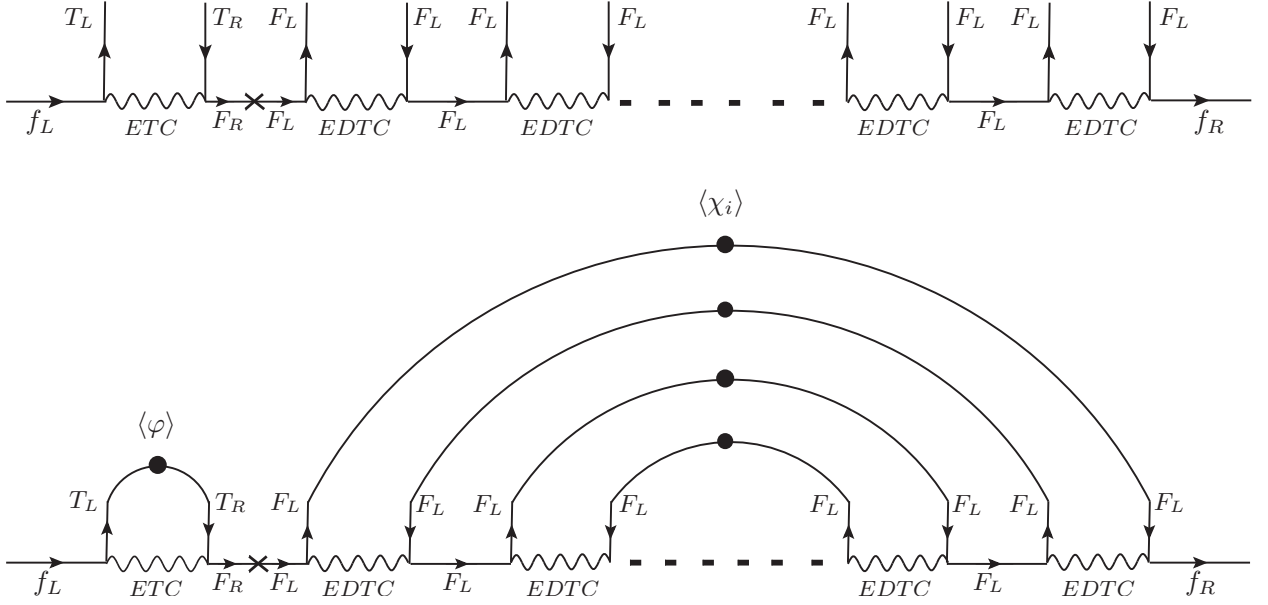


Figure 6: The Feynman diagrams for the masses of the charged fermions in the minimal version of the DTC-paradigm.

There are a few important observations in this scenario. First, multifermion chiral condensates $\langle\chi_r\rangle$ must be of the form $\langle\chi_r\rangle = \bar{F}_L F_L \cdots \bar{F}_L F_L$ with zero chirality. These are not the most attractive states for multifermion chiral spin-zero modes. Moreover, the chiral enhancement in this scenario is zero. Hence, they cannot explain the flavour problem of the SM. Furthermore, we observe that we have to eventually introduce an EDTC symmetry to obtain the fermionic mass spectrum. This symmetry is already an essential ingredient of the DTC paradigm. Thus, we can conclude that the minimal version of the DTC paradigm is not a preferred framework.

6 Experimental constraints on the DTC-paradigm

In this section, we discuss crucial experimental bounds on the DTC paradigm. We notice that the DTC paradigm is defined by a QCD-like dynamics. Therefore, the QCD spectrum plays an important role in defining the spectrum of the DTC paradigm. Moreover, we will use the EMAC hypothesis to address the DTC spectrum and its experimental limitations.

6.1 Higgs mass constraint

We notice that the lightest scalar in QCD, the σ meson, can be predicted as [39],

$$m_\sigma \approx 2m_{\text{dyn}}. \quad (123)$$

where m_{dyn} is a non-perturbative dynamically generated mass. Taking $m_{\text{dyn}} \approx \Lambda_{\text{QCD}} \approx 250$ MeV, we obtain $m_\sigma \approx 500$ MeV, which is in agreement with the experimental measurement [40].

Similarly, a composite Higgs boson in a QCD-like TC theory is predicted to be [41],

$$m_H \approx 2M_{\text{dyn,TC}}. \quad (124)$$

For the TC dynamics, even if we assume the $M_{\text{dyn,TC}} = 100$ GeV, which is the electroweak scale, the mass of the Higgs should be around 200 GeV. Thus, we see that QCD-like TC theories predict a heavy Higgs. This is a failure of QCD-like TC theories, given the fact that Higgs is discovered with a mass of 125 GeV [42, 43].

To solve this problem, we use the EMAC hypothesis and assume that breaking of $U(1)_A$ symmetry, thus the chirality, plays an important role in the suppression of the Higgs mass, although the scale Λ_{TC} may be at the TeV scale. Taking inspiration from equation 13, we assume that Higgs is a bound state dominated by a negative chirality. For instance, Higgs may be a composite state of fermions such as $\bar{T}_L \bar{B}_L$, which is a most attractive mode predicted by the EMAC hypothesis [30].

We notice that the non-perturbative mass $M_{\text{dyn}}^{\text{TC}}$ can be related to the chiral fermionic condensate [41],

$$-\langle \bar{T}T \rangle = \frac{N_{\text{TC}}}{4\pi^2} M_{\text{dyn,TC}}^3 \alpha_{\text{TC}}(\mu^2). \quad (125)$$

Now, using equation 30 and 125, we can write the Higgs mass as,

$$m_{\text{Higgs}} \approx 2M_{\text{dyn,TC}} \exp(k_{\text{TC}} \Delta\chi_{\text{TC}}), \quad (126)$$

where we assume $\Delta\chi_{\text{TC}} = -2$, $\alpha_{\text{TC}}(M_{\text{dyn,TC}}^2) = 1$, and k_{TC} to be positive. This means that even though $M_{\text{dyn,TC}}$ may be on the TeV scale, the Higgs mass can still be as low as 125 GeV because of the chiral suppression caused by the fermionic body number in the bound state of the Higgs boson. By proposing this, we extend the idea of EMAC to the chiral fermionic condensates, which are most attractive even with negative chirality.

6.2 S-parameter

The TC dynamics is bounded by the oblique parameters [44, 45]. In particular, the S parameter is highly sensitive to the TC models. The current values of the S and T parameters are [40],

$$S = -0.04 \pm 0.10, \quad T = 0.01 \pm 0.12. \quad (127)$$

For strongly coupled theories, these parameters at next-to-leading-order are derived in reference [46, 47], and can be written as,

$$S_{\text{NLO}} > \frac{4\pi v^2}{M_V^2} + \Delta S_{\text{NLO}}|_{\varphi\varphi, h\varphi} + \Delta S_{\text{NLO}}|_{\psi\bar{\psi}}, \quad (128)$$

where

$$\Delta S_{\text{NLO}}|_{\varphi\varphi, h\varphi} = \frac{1}{12\pi} \left[\left(1 - \kappa_W^2\right) \left(\log \frac{M_V^2}{m_h^2} - \frac{11}{6} \right) - \kappa_W^2 \left(\log \frac{M_A^2}{M_V^2} - 1 + \frac{M_A^2}{M_V^2} \right) \right], \quad (129)$$

$$\Delta S_{\text{NLO}}|_{\psi\bar{\psi}} = -\frac{F_V^2 \left(C_0^{V_3^1}\right)^2}{3\pi M_V^2} \left(1 - \frac{M_V^2}{M_A^2} + \log \frac{M_A^2}{M_V^2} \right). \quad (130)$$

$$T|_{\varphi\varphi, h\varphi} = \frac{3}{16\pi \cos^2 \theta_W} \left[\left(1 - \kappa_W^2\right) \left(1 - \log \frac{M_V^2}{m_h^2} \right) + \kappa_W^2 \log \frac{M_A^2}{M_V^2} \right],$$

where only the first Weinberg-Sum-Rule is assumed, and the $\kappa_W = \frac{M_V^2}{M_A^2}$ is the coupling of the lightest scalar (Higgs boson) to two gauge bosons (W^+W^- or ZZ).

For $\kappa_W = 1.023 \pm 0.026$, the bounds on the vector resonances in a QCD-like theory turn out to be [46],

$$M_A \geq M_V \geq 2 \text{ TeV} \quad (95\% \text{CL}). \quad (131)$$

Now the really important question is: why this vector TC meson is $m_{\rho_{TC}} \geq 2 \text{ TeV}$, despite the discovery of Higgs at 125 GeV. An answer to this question can originate from our crucial assumption that the mass spectrum of the TC dynamics is hierarchical due to the chiral dependence of the multifermionic bound states as suggested by the EMAC principle. We can assume that the vector TC meson is a multifermion bound state such as $\bar{T}_L T_L T_L B_L$ or $\bar{B}_L B_L T_L B_L$, and its mass is given by

$$m_{\rho_{TC}} \approx \Lambda_{TC} \exp(k_{TC} \Delta\chi_{TC}), \quad (132)$$

where $\Delta\chi_{TC} \geq 2$. Thus, the mass of the vector TC meson is chirally enhanced compared to the mass of the Higgs boson in the DTC paradigm.

7 Scaling relations and mass spectrum

The mass spectrum of the DTC paradigm can be determined through the scaling relations. We note that the TC, DTC, and DQCD-dynamics are rescaled replicas of the QCD dynamics. Therefore, we can write their scaling relations with respect to QCD using the 't Hooft large N limit [48, 49]. For instance, in the large N_{th} colours limit,

$$F_{th} \propto \sqrt{N_{th}} \Lambda_{th}, \quad (133)$$

where Λ_{th} is the scale of a generic non-Abelian strong gauge theory, and N_{th} are its number of colours. This allows us to write a generic scaling relation for decay constants,

$$F_{th} = \sqrt{\frac{N_{th}}{N_{QCD}}} \frac{\Lambda_{th}}{\Lambda_{QCD}} f_\pi. \quad (134)$$

where $f_\pi = 95.4 \text{ MeV}$ [40].

A similar scaling relation can be written for the mass of the pseudoscalar η_{th} [50],

$$m_{\eta_{th}} = \sqrt{\frac{2}{3}} \frac{F_{th}}{f_\pi} \frac{N_{QCD}}{N_{th}} m_{\eta_{QCD}}. \quad (135)$$

A scaling relation for the scalars of the DTC paradigm, for instance the TC scalar, i.e. the Higgs boson, can be written using equations 123 and 126, and given as,

$$m_H = \frac{M_{\text{dyn,TC}}}{m_{\text{dyn}}} m_\sigma \exp(k_{TC} \Delta\chi_{TC}). \quad (136)$$

We observe that the ration $m_\sigma/m_{\text{dyn}} \approx 2$, assuming $m_{\text{dyn}} \approx \Lambda_{QCD} \approx 250 \text{ MeV}$ [51] and $m_\sigma \approx 500 \text{ MeV}$ [40]. This results in,

$$m_H \approx 2M_{\text{dyn,TC}} \exp(k_{TC} \Delta\chi_{TC}). \quad (137)$$

Thus, the scaling relations of the DTC paradigm scalars with respect to QCD are trivial. Since the mass of the Higgs boson is now known, we can write the scaling relations of the unknown lowest-lying scalars of the DTC paradigm with respect to the TC dynamics. Thus, for the DTC scalar, using equation 126, we write,

$$m_{H_{DTC}} = \frac{M_{\text{dyn,DTC}}}{M_{\text{dyn,TC}}} m_H \exp(k_{DTC} \Delta\chi_{DTC} - k_{TC} \Delta\chi_{TC}). \quad (138)$$

Similarly, the other scalar mass is given as,

$$m_{H_D} = \frac{M_{\text{dyn,D}}}{M_{\text{dyn,TC}}} m_H \exp(k_D \Delta\chi_D - k_{TC} \Delta\chi_{TC}). \quad (139)$$

7.1 Mass spectrum when the SHVM is accommodated within the DTC-paradigm

In the scenario where the SHVM is the low-energy effective limit of the DTC paradigm, we use the fit results obtained in sub-section 4.2. These are obtained for three scenarios given as $\Lambda_{\text{DTC}} \approx \Lambda$, $\Lambda_{\text{DTC}} < \Lambda$, and $\Lambda_{\text{DTC}} > \Lambda$ with three choices of multifermionic condensates, namely $N_2 : \{n_1, n_2, n_3, n_4, n_5, n_6, n_7\} = \{2, 4, 6, 2, 2, 4, 2\}$, $N_4 : \{n_1, n_2, n_3, n_4, n_5, n_6, n_7\} = \{4, 6, 8, 4, 4, 6, 2\}$, and $N_6 : \{n_1, n_2, n_3, n_4, n_5, n_6, n_7\} = \{6, 8, 10, 6, 6, 8, 2\}$. The number of colors allowed for these three scenarios is shown in tables 3-5.

$\Lambda \approx \Lambda_{\text{DTC}}$	N_{TC}	N_{DTC}	N_{D}
N_2	16	17	17
N_4	9	9	9
N_6	2	2	3

Table 3: Number of colours determined from the fit in the three cases: N_2 , N_4 and N_6 for the scenario $\Lambda \approx \Lambda_{\text{DTC}}$ in the SHVM mechanism.

$\Lambda > \Lambda_{\text{DTC}}$	N_{TC}	N_{DTC}	N_{D}
N_2	10	18	3
N_4	10	18	4
N_6	12	17	15

Table 4: Number of colours determined from the fit in the three cases: N_2 , N_4 and N_6 for the scenario $\Lambda > \Lambda_{\text{DTC}}$ in the SHVM mechanism.

$\Lambda < \Lambda_{\text{DTC}}$	N_{TC}	N_{DTC}	N_{D}
N_2	16	12	8
N_4	14	6	12
N_6	8	4	9

Table 5: Number of colours determined from the fit in the three cases: N_2 , N_4 and N_6 for the scenario $\Lambda < \Lambda_{\text{DTC}}$ in the SHVM mechanism.

We assume $M_{\text{dyn,TC}} \approx \Lambda_{\text{TC}}$, $M_{\text{dyn,DTC}} \approx \Lambda_{\text{DTC}}$, and $M_{\text{dyn,D}} \approx \Lambda$. The masses of the lowest-lying pseudo-scalars are obtained using the scaling relation 135, and are given in tables 6-8.

N_2	$\Lambda \approx \Lambda_{\text{DTC}}$	$\Lambda > \Lambda_{\text{DTC}}$	$\Lambda < \Lambda_{\text{DTC}}$
$m_{\eta_{\text{TC}}}$ [GeV]	998	1823	977
$m_{\eta_{\text{DTC}}}$ [GeV]	782	760	1862
$m_{\eta_{\text{D}}}$ [GeV]	782	3225	1140

Table 6: Masses $m_{\eta_{\text{TC,DTC,D}}}$ [GeV] of $\eta_{\text{TC,DTC,D}}$ in the SHVM for the scenario N_2 .

N_4	$\Lambda \approx \Lambda_{\text{DTC}}$	$\Lambda > \Lambda_{\text{DTC}}$	$\Lambda < \Lambda_{\text{DTC}}$
$m_{\eta_{\text{TC}}}$ [GeV]	1178	1309	884
$m_{\eta_{\text{DTC}}}$ [GeV]	1075	760	2633
$m_{\eta_{\text{D}}}$ [GeV]	1075	3225	931

Table 7: Masses $m_{\eta_{\text{TC,DTC,D}}}$ [GeV] of $\eta_{\text{TC,DTC,D}}$ in the SHVM for the scenario N_4 .

N_6	$\Lambda \approx \Lambda_{DTC}$	$\Lambda > \Lambda_{DTC}$	$\Lambda < \Lambda_{DTC}$
$m_{\eta_{TC}}$ [GeV]	2412	551	962
$m_{\eta_{DTC}}$ [GeV]	2280	782	3225
m_{η_D} [GeV]	1862	1665	1075

Table 8: Masses $m_{\eta_{TC,DTC,D}}$ [GeV] of $\eta_{TC,DTC,D}$ in the SHVM for the scenario N_6 .

We use the scaling relation given in equations 138 and 139 to obtain the masses of lowest-lying scalars. They are given in tables 9- 11.

$\Delta\chi_{DTC,D}$	$\Lambda \approx \Lambda_{DTC}$		$\Lambda > \Lambda_{DTC}$		$\Lambda < \Lambda_{DTC}$	
	+2	-2	+2	-2	+2	-2
$m_{H_{DTC}}$ [GeV]	1157	878	1376	726	2778	1464
m_{H_D} [GeV]	$4.5 \cdot 10^{-8}$	$2.2 \cdot 10^{-3}$	$6.6 \cdot 10^8$	$1.5 \cdot 10^{-3}$	$4.0 \cdot 10^8$	$2.5 \cdot 10^{-3}$

Table 9: Masses [GeV] of scalars of the DTC and DQCD sectors in the SHVM for $\Delta\chi_{DTC,D} = \pm 2$ for the scenario N_2 .

$\Delta\chi_{DTC,D}$	$\Lambda \approx \Lambda_{DTC}$		$\Lambda > \Lambda_{DTC}$		$\Lambda < \Lambda_{DTC}$	
	+2	-2	+2	-2	+2	-2
$m_{H_{DTC}}$ [GeV]	1182	828	1209	844	2377	1665
m_{H_D} [GeV]	$6.3 \cdot 10^8$	$1.5 \cdot 10^{-3}$	$5.0 \cdot 10^8$	$2.0 \cdot 10^{-3}$	$2.5 \cdot 10^8$	$4.0 \cdot 10^{-3}$

Table 10: Masses [GeV] of scalars of the DTC and DQCD sectors in the SHVM for $\Delta\chi_{DTC,D} = \pm 2$ for the scenario N_4 .

$\Delta\chi_{DTC,D}$	$\Lambda \approx \Lambda_{DTC}$		$\Lambda > \Lambda_{DTC}$		$\Lambda < \Lambda_{DTC}$	
	+2	-2	+2	-2	+2	-2
$m_{H_{DTC}}$ [GeV]	1276	790	1067	909	2419	1621
m_{H_D} [GeV]	$1.7 \cdot 10^9$	$5.9 \cdot 10^{-4}$	$9.1 \cdot 10^8$	$1.0 \cdot 10^{-3}$	$3.7 \cdot 10^8$	$2.7 \cdot 10^{-3}$

Table 11: Masses [GeV] of scalars of the DTC and DQCD sectors in the SHVM for $\Delta\chi_{DTC,D} = \pm 2$ for the scenario N_6 .

The masses of TC vector mesons in different scenarios are obtained using equation 132 for $\Delta\chi_{TC} = 2$, and are given in table 12.

	$\Lambda_F \approx \Lambda_{DTC}$	$\Lambda_F > \Lambda_{DTC}$	$\Lambda_F < \Lambda_{DTC}$
N_2	6169	12781	5923
N_4	4748	6665	4189
N_6	4497	1381	2821

Table 12: Masses $m_{\rho_{TC}}$ [GeV] in the SHVM for the scenarios N_2 , N_4 , and N_6 .

We notice that the masses satisfy the bounds of the S parameter given in equation 131 except for the scenario denoted by N_6 and $\Lambda > \Lambda_{DTC}$. Even this bound can be evaded if we assume $\Delta\chi_{TC} = 4$.

7.2 Mass spectrum when the FN mechanism is built within the DTC-paradigm

In the scenario when the FN mechanism is the effective low energy limit of the DTC paradigm, the flavon field is assumed to be in a two-fermion bound state, and the corresponding number of colours for three scenarios given as $\Lambda_{DTC} \approx \Lambda$, $\Lambda_{DTC} < \Lambda$, and $\Lambda_{DTC} > \Lambda$, is quoted in Table 13.

	N_{TC}	N_{DTC}	N_D
$\Lambda \approx \Lambda_{DTC}$	4	3	2
$\Lambda > \Lambda_{DTC}$	3	5	2
$\Lambda < \Lambda_{DTC}$	2	3	2

Table 13: Number of colours determined from the fit for the scenarios $\Lambda_{DTC} \approx \Lambda$, $\Lambda_{DTC} < \Lambda$, and $\Lambda_{DTC} > \Lambda$ in the FN mechanism.

The masses of the lowest-lying scalars and pseudoscalar mesons are given in tables 14 and 15.

	$\Lambda_F \approx \Lambda_{DTC}$	$\Lambda_F > \Lambda_{DTC}$	$\Lambda_F < \Lambda_{DTC}$
$m_{\eta_{TC}}$ [GeV]	17415	21971	24628
$m_{\eta_{DTC}}$ [GeV]	1862	1442	3724
m_{η_D} [GeV]	2280	4561	2280

Table 14: Masses $m_{\eta_{TC,DTC,D}}$ [GeV] of $\eta_{TC,DTC,D}$ in the FN mechanism.

$\Delta\chi_{DTC,D}$	$\Lambda_F \approx \Lambda_{DTC}$		$\Lambda_F > \Lambda_{DTC}$		$\Lambda_F < \Lambda_{DTC}$	
	+2	-2	+2	-2	+2	-2
$m_{H_{DTC}}$ [GeV]	1009	993	1075	916	2002	2002
m_{H_D} [GeV]	7397	135	14667	269	7397	135

Table 15: Masses [GeV] of scalars of the DTC and DQCD sectors in the FN mechanism for $\Delta\chi_{DTC,D} = \pm 2$, where for m_{H_D} we have assumed $k_D = 1$.

We show the masses of TC vector-mesons in different scenarios in table 16 for $\Delta\chi_{TC} = 2$.

	$\Lambda_F \approx \Lambda_{DTC}$	$\Lambda_F > \Lambda_{DTC}$	$\Lambda_F < \Lambda_{DTC}$
$m_{\rho_{TC}}$ [GeV]	$4.67 \cdot 10^5$	$5.53 \cdot 10^5$	$4.67 \cdot 10^5$

Table 16: Masses $m_{\rho_{TC}}$ [GeV] in the FN mechanism.

8 Collider phenomenology of the DTC-paradigm

In this section, we investigate the collider signatures of the DTC paradigm at the HL-LHC, the HE-LHC, and a future 100 TeV collider. For this purpose, we assume that the TC sector has only one fermionic doublet, that is, only two flavours, T and B . Our main interest is to investigate the lowest-lying scalars and pseudoscalars of the TC, DTC, and DQCD spectrum. This will be done by studying the production sensitivities of the pions, etas, and scalars.

We assume that the interactions between the TC and DTC, and between the TC and DQCD are negligible. This results in effectively zero mixing between the Higgs and χ_i fields of the SHVM, and the Higgs and the flavon field χ in the FN mechanism. The LHC searches for low-mass scalars [52] will not be able to constrain

this scenario. Moreover, decays of composite scalars and pseudoscalars to WW and ZZ now occur at the one-loop level, and are much suppressed. We notice that the LHC searches for scalars in WW and ZZ modes place bounds on masses above 300 GeV from ATLAS [53] and 200 GeV from CMS [54]. The searches in the di-photon channel limit the masses of scalars above 200 GeV from ATLAS [55] and above 500 GeV from the CMS [56].

Our main signatures for collider physics are inclusive channels where pions, etas, and scalars of the DTC paradigm are produced, and further decay to specific channels, given by

$$pp \rightarrow \Pi_{\text{DTC,D}}/\eta_{\text{TC,DTC,D}}/H_{\text{DTC,D}} \rightarrow f_i f_j / \gamma\gamma \quad (140)$$

where f_i represents an SM fermion.

8.1 Current and future sensitivities

The sensitivities of the production cross-sections of a heavy and a light pseudoscalar in different modes for the HL-LHC, the HE-LHC, and a 100 TeV hadron collider are estimated in reference [38], and are given in tables 17 and 18.

m [GeV]	HL-LHC [14 TeV, 3 ab ⁻¹]		HE-LHC [27 TeV, 15 ab ⁻¹]		100 TeV, 30 ab ⁻¹	
	500	1000	500	1000	500	1000
$\tau\tau$ [pb]	$7 \cdot 10^{-3}$	$1 \cdot 10^{-3}$	$4 \cdot 10^{-3}$	$7 \cdot 10^{-4}$	$5 \cdot 10^{-3}$	$8 \cdot 10^{-4}$
$ee, \mu\mu$ [pb]	$2 \cdot 10^{-4}$	$4 \cdot 10^{-5}$	$1 \cdot 10^{-4}$	$3 \cdot 10^{-5}$	$1 \cdot 10^{-4}$	$3 \cdot 10^{-5}$
$\gamma\gamma$ [pb]	$1 \cdot 10^{-4}$	$2 \cdot 10^{-5}$	$6 \cdot 10^{-5}$	$1 \cdot 10^{-5}$	$7 \cdot 10^{-5}$	$1 \cdot 10^{-5}$
$b\bar{b}$ [pb]		$9 \cdot 10^{-3}$		$5 \cdot 10^{-3}$		$7 \cdot 10^{-3}$
$t\bar{t}$ [pb]	4	$5 \cdot 10^{-2}$	3	$4 \cdot 10^{-2}$	8	0.1

Table 17: Projected reach $\sigma \times \text{BR}$ for high-mass scalar or pseudoscalar resonance searches through inclusive production channels at the HL-LHC, the HE-LHC, and a future 100 TeV collider.

m [GeV]	HL-LHC [14 TeV, 3 ab ⁻¹]		HE-LHC [27 TeV, 15 ab ⁻¹]		100 TeV, 30 ab ⁻¹	
	20	60	20	60	20	60
$\tau\tau$ [pb]		0.9		0.5		0.6
$\gamma\gamma$ [pb]	1.3	1.5	0.7	0.8	0.8	0.9

Table 18: Projected reach $\sigma \times \text{BR}$ for low-mass scalar or pseudoscalar resonance searches through inclusive production channels at the HL-LHC, the HE-LHC, and a future 100 TeV collider.

In addition to the above sensitivities of masses, the mass spectrum of the DTC paradigm contains other different masses of etas and scalars. The sensitivities of these masses are not given in reference [38]. To estimate the sensitivities of these masses in the HL-LHC, the HE-LHC, and a future 100 TeV collider, we use the prescription discussed in reference [38]. For this purpose, we use square root scaling of the luminosity of the LHC by,

$$\mathcal{S} \simeq \frac{S}{\sqrt{B}} \simeq \sqrt{\mathcal{L}} \frac{\sigma_s}{\sqrt{\sigma_B}}, \quad (141)$$

where S denotes the number of signal events, B is the background events, σ_s stands for the signal cross-section, and σ_B shows the background cross-section.

As discussed in reference [38], a conservative estimate of the sensitivities of the HL-LHC, the HE-LHC and 100 TeV collider can be made with the following assumptions:

1. The significance $\mathcal{S} \simeq \frac{S}{\sqrt{B}}$ does not change among colliders.
2. The reconstruction efficiencies and background rejection remain constant among colliders.

These assumptions are also used in the ‘‘Collider Reach’’ tool, which is capable of providing an estimate of the mass of a BSM physics at the LHC and a future collider [57].

Thus, the sensitivity of a signal of scalar mass at a future collider (FC) is given by

$$\sigma_s^{\text{FC}} = \sqrt{\frac{\mathcal{L}_{\text{LHC}}}{\mathcal{L}_{\text{FC}}}} \sqrt{\frac{\sigma_B^{\text{FC}}}{\sigma_B^{\text{LHC}}}} \sigma_s^{\text{LHC}}, \quad (142)$$

where FC= HL-LHC, HE-LHC, and a 100 TeV collider. As observed in reference [38], σ_B^{FC} and σ_B^{LHC} turn out to be $\sigma_B^{\text{HE-LHC}} \leq 2\sigma_B^{\text{LHC}}$ and $\sigma_B^{100\text{TeV}} \leq 10\sigma_B^{\text{LHC}}$, and σ_s^{LHC} represents the current limits given in tables 19-22.

m [GeV]	$\mathcal{L}[fb^{-1}]$ [References]		ATLAS 13 TeV				CMS 13 TeV			
	ATLAS	CMS	135	269	551	782	135	269	551	782
$\tau\tau$ [pb]	36.1 [58]	35.9 [59]		0.2	$6 \cdot 10^{-2}$	$2 \cdot 10^{-2}$	3.4	0.4	$5 \cdot 10^{-2}$	$2 \cdot 10^{-2}$
$ee, \mu\mu$ [pb]	139 [60]	140 [61]		$2 \cdot 10^{-3}$	$7 \cdot 10^{-4}$	$4 \cdot 10^{-4}$		$6 \cdot 10^{-3}$	$1 \cdot 10^{-3}$	$6 \cdot 10^{-4}$
$\gamma\gamma$ [pb]	139 [55]	35.9 [56]		$2 \cdot 10^{-3}$	$5 \cdot 10^{-4}$	$2 \cdot 10^{-4}$			$2 \cdot 10^{-3}$	$9 \cdot 10^{-4}$
$t\bar{t}$ [pb]	36.1 [62, 63]	35.9 [64]			40	3.7			14	0.94

Table 19: Current limits on production cross-section times branching ratio ($\sigma \times BR$) at 13 TeV LHC from ATLAS and CMS resonance searches for scalars or pseudoscalars.

m [GeV]	$\mathcal{L}[fb^{-1}]$ [References]		ATLAS 13 TeV				CMS 13 TeV			
	ATLAS	CMS	909	1067	1276	1442	909	1067	1276	1442
$\tau\tau$ [pb]	36.1 [58]	35.9 [59]	$1 \cdot 10^{-2}$	$9 \cdot 10^{-3}$	$7 \cdot 10^{-3}$	$6 \cdot 10^{-3}$	$2 \cdot 10^{-2}$	$1 \cdot 10^{-2}$	$8 \cdot 10^{-3}$	$7 \cdot 10^{-3}$
$ee, \mu\mu$ [pb]	139 [60]	140 [61]	$2 \cdot 10^{-4}$	$2 \cdot 10^{-4}$	$2 \cdot 10^{-4}$	$1 \cdot 10^{-4}$	$4 \cdot 10^{-4}$	$2 \cdot 10^{-4}$	$2 \cdot 10^{-4}$	$2 \cdot 10^{-4}$
$\gamma\gamma$ [pb]	139 [55]	35.9 [56]	$2 \cdot 10^{-4}$	$2 \cdot 10^{-4}$	$7 \cdot 10^{-5}$	$8 \cdot 10^{-5}$	$9 \cdot 10^{-4}$	$6 \cdot 10^{-4}$	$7 \cdot 10^{-4}$	$4 \cdot 10^{-4}$
$b\bar{b}$ [pb]	36.1 [62, 63]	35.9 [64]		$5 \cdot 10^{-2}$	$3 \cdot 10^{-2}$	$4 \cdot 10^{-2}$				
$t\bar{t}$ [pb]	36.1 [62, 63]	35.9 [64]	2	2	2	1.3	0.56	0.35	0.3	0.1

Table 20: Current limits on $\sigma \times BR$ at 13 TeV LHC from ATLAS and CMS resonance searches for scalars or pseudoscalars.

m [GeV]	$\mathcal{L}[fb^{-1}]$ [References]		ATLAS 13 TeV				CMS 13 TeV			
	ATLAS	CMS	1665	1862	2280	2412	1665	1862	2280	2412
$\tau\tau$ [pb]	36.1 [58]	35.9 [59]	$6 \cdot 10^{-3}$	$6 \cdot 10^{-3}$	$6 \cdot 10^{-3}$		$5 \cdot 10^{-3}$	$4 \cdot 10^{-3}$	$4 \cdot 10^{-3}$	$4 \cdot 10^{-3}$
$ee, \mu\mu$ [pb]	139 [60]	140 [61]	$1 \cdot 10^{-4}$	$5 \cdot 10^{-5}$	$6 \cdot 10^{-5}$	$6 \cdot 10^{-5}$	$9 \cdot 10^{-5}$	$1 \cdot 10^{-4}$	$8 \cdot 10^{-5}$	$5 \cdot 10^{-5}$
$\gamma\gamma$ [pb]	139 [55]	35.9 [56]	$8 \cdot 10^{-5}$	$4 \cdot 10^{-5}$	$6 \cdot 10^{-5}$	$3 \cdot 10^{-5}$	$1 \cdot 10^{-4}$	$3 \cdot 10^{-4}$	$1 \cdot 10^{-4}$	$1 \cdot 10^{-4}$
$b\bar{b}$ [pb]	36.1 [62, 63]	35.9 [64]	$2 \cdot 10^{-2}$	$1 \cdot 10^{-2}$	$1 \cdot 10^{-2}$	$1 \cdot 10^{-2}$		$3 \cdot 10^{-2}$	$2 \cdot 10^{-2}$	$2 \cdot 10^{-2}$
$t\bar{t}$ [pb]	36.1 [62, 63]	35.9 [64]	2	0.2	$4 \cdot 10^{-2}$	$4 \cdot 10^{-2}$	$6 \cdot 10^{-2}$	$3 \cdot 10^{-2}$	$2 \cdot 10^{-2}$	$2 \cdot 10^{-2}$

Table 21: Current limits on $\sigma \times BR$ at 13 TeV LHC from ATLAS and CMS high-mass resonance searches for scalars or pseudoscalars.

m [GeV]	$\mathcal{L}[fb^{-1}]$ [References]		ATLAS 13 TeV				CMS 13 TeV			
	ATLAS	CMS	3225	3724	4561	7397	3225	3724	4561	7397
$\tau\tau$ [pb]	36.1 [58]	35.9 [59]					$3 \cdot 10^{-3}$			
$ee, \mu\mu$ [pb]	139 [60]	140 [61]	$2 \cdot 10^{-5}$	$1 \cdot 10^{-5}$	$1 \cdot 10^{-5}$	$1 \cdot 10^{-5}$	$3 \cdot 10^{-5}$	$2 \cdot 10^{-5}$	$2 \cdot 10^{-5}$	
$\gamma\gamma$ [pb]	139 [55]	35.9 [56]	$3 \cdot 10^{-5}$				$9 \cdot 10^{-5}$	$9 \cdot 10^{-5}$	$9 \cdot 10^{-5}$	
$b\bar{b}$ [pb]	36.1 [62, 63]	35.9 [64]	$2 \cdot 10^{-3}$	$2 \cdot 10^{-3}$	$7 \cdot 10^{-4}$	$1 \cdot 10^{-4}$	$2 \cdot 10^{-2}$	$9 \cdot 10^{-3}$	$4 \cdot 10^{-3}$	$4 \cdot 10^{-4}$
$t\bar{t}$ [pb]	36.1 [62, 63]	35.9 [64]	$2 \cdot 10^{-2}$	$2 \cdot 10^{-2}$	$2 \cdot 10^{-2}$		$4 \cdot 10^{-3}$	$4 \cdot 10^{-3}$	$3 \cdot 10^{-3}$	$1 \cdot 10^{-3}$

Table 22: Current limits on $\sigma \times BR$ at 13 TeV LHC from ATLAS and CMS high-mass resonance searches for scalars or pseudoscalars.

Our estimate of the sensitivities of the masses given in tables 19-22 at the HL-LHC, the HE-LHC, and a future 100 TeV collider are given in tables 23-28.

m [GeV]	135	269	551	782	909	1067	1276	1442
$\tau\tau$ [pb]	$4 \cdot 10^{-1}$	$2 \cdot 10^{-2}$	$5 \cdot 10^{-3}$	$2 \cdot 10^{-3}$	$1 \cdot 10^{-3}$	$9 \cdot 10^{-4}$	$7 \cdot 10^{-4}$	$6 \cdot 10^{-4}$
$\mu\mu, ee$ [pb]		$4 \cdot 10^{-4}$	$1 \cdot 10^{-4}$	$8 \cdot 10^{-5}$	$4 \cdot 10^{-5}$	$4 \cdot 10^{-5}$	$2 \cdot 10^{-6}$	$2 \cdot 10^{-5}$
$\gamma\gamma$ [pb]		$4 \cdot 10^{-4}$	$1 \cdot 10^{-4}$	$4 \cdot 10^{-5}$	$4 \cdot 10^{-5}$	$4 \cdot 10^{-5}$	$1 \cdot 10^{-5}$	$2 \cdot 10^{-5}$
$b\bar{b}$ [pb]						$8 \cdot 10^{-3}$	$6 \cdot 10^{-3}$	$8 \cdot 10^{-3}$
$t\bar{t}$ [pb]			1.5	0.1	$6 \cdot 10^{-2}$	$4 \cdot 10^{-2}$	$3 \cdot 10^{-2}$	$1 \cdot 10^{-2}$

Table 23: Estimated reach $\sigma \times BR$ for scalar or pseudoscalar resonance searches through various inclusive production channels at the HL-LHC.

m [GeV]	1862	2280	2412	3225	3724	4561	7397
$\tau\tau$ [pb]	$4 \cdot 10^{-4}$	$4 \cdot 10^{-4}$	$4 \cdot 10^{-4}$	$3 \cdot 10^{-4}$			
$\mu\mu, ee$ [pb]	$1 \cdot 10^{-5}$	$1 \cdot 10^{-5}$	$1 \cdot 10^{-5}$	$4 \cdot 10^{-6}$	$2 \cdot 10^{-6}$	$2 \cdot 10^{-6}$	$2 \cdot 10^{-6}$
$\gamma\gamma$ [pb]	$9 \cdot 10^{-6}$	$1 \cdot 10^{-5}$	$6 \cdot 10^{-6}$	$6 \cdot 10^{-6}$	$1 \cdot 10^{-5}$	$1 \cdot 10^{-5}$	
$b\bar{b}$ [pb]	$2 \cdot 10^{-3}$	$2 \cdot 10^{-3}$	$2 \cdot 10^{-3}$	$4 \cdot 10^{-4}$	$4 \cdot 10^{-4}$	$1 \cdot 10^{-4}$	$8 \cdot 10^{-5}$
$t\bar{t}$ [pb]	$3 \cdot 10^{-3}$	$2 \cdot 10^{-3}$	$2 \cdot 10^{-3}$	$4 \cdot 10^{-4}$	$4 \cdot 10^{-4}$	$3 \cdot 10^{-4}$	$1 \cdot 10^{-4}$

Table 24: Estimated reach $\sigma \times BR$ for scalar or pseudoscalar resonance searches through various inclusive production channels at the HL-LHC.

m [GeV]	135	269	551	782	909	1067	1276	1442	1665
$\tau\tau$ [pb]	$2 \cdot 10^{-1}$	$1 \cdot 10^{-2}$	$3 \cdot 10^{-3}$	$1 \cdot 10^{-3}$	$7 \cdot 10^{-4}$	$6 \cdot 10^{-4}$	$5 \cdot 10^{-4}$	$4 \cdot 10^{-4}$	$3 \cdot 10^{-4}$
$\mu\mu, ee$ [pb]		$3 \cdot 10^{-4}$	$9 \cdot 10^{-5}$	$5 \cdot 10^{-5}$	$3 \cdot 10^{-5}$	$3 \cdot 10^{-5}$	$3 \cdot 10^{-5}$	$1 \cdot 10^{-5}$	$1 \cdot 10^{-5}$
$\gamma\gamma$ [pb]		$3 \cdot 10^{-4}$	$6 \cdot 10^{-5}$	$3 \cdot 10^{-5}$	$3 \cdot 10^{-5}$	$3 \cdot 10^{-5}$	$9 \cdot 10^{-6}$	$1 \cdot 10^{-5}$	$1 \cdot 10^{-5}$
$b\bar{b}$ [pb]						$5 \cdot 10^{-3}$	$4 \cdot 10^{-3}$	$5 \cdot 10^{-3}$	$3 \cdot 10^{-3}$
$t\bar{t}$ [pb]			0.9	$6 \cdot 10^{-2}$	$4 \cdot 10^{-2}$	$2 \cdot 10^{-2}$	$2 \cdot 10^{-2}$	$7 \cdot 10^{-3}$	$4 \cdot 10^{-3}$

Table 25: Estimated reach $\sigma \times BR$ for scalar or pseudoscalar resonance searches through various inclusive production channels at the HE-LHC.

m [GeV]	1862	2280	2412	3225	3724	4561	7397
$\tau\tau$ [pb]	$3 \cdot 10^{-4}$	$3 \cdot 10^{-4}$	$3 \cdot 10^{-4}$	$2 \cdot 10^{-4}$			
$\mu\mu, ee$ [pb]	$7 \cdot 10^{-6}$	$8 \cdot 10^{-6}$	$7 \cdot 10^{-6}$	$3 \cdot 10^{-6}$	$1 \cdot 10^{-6}$	$1 \cdot 10^{-6}$	$1 \cdot 10^{-6}$
$\gamma\gamma$ [pb]	$5 \cdot 10^{-6}$	$8 \cdot 10^{-6}$	$4 \cdot 10^{-6}$	$4 \cdot 10^{-6}$	$6 \cdot 10^{-6}$	$6 \cdot 10^{-6}$	
$b\bar{b}$ [pb]	$1 \cdot 10^{-3}$	$1 \cdot 10^{-3}$	$1 \cdot 10^{-3}$	$3 \cdot 10^{-4}$	$3 \cdot 10^{-4}$	$9 \cdot 10^{-5}$	$5 \cdot 10^{-5}$
$t\bar{t}$ [pb]	$2 \cdot 10^{-3}$	$1 \cdot 10^{-3}$	$1 \cdot 10^{-3}$	$3 \cdot 10^{-4}$	$3 \cdot 10^{-4}$	$2 \cdot 10^{-4}$	$7 \cdot 10^{-5}$

Table 26: Estimated reach $\sigma \times \text{BR}$ for scalar or pseudoscalar resonance searches through various inclusive production channels at the HE-LHC.

m [GeV]	135	269	551	782	909	1067	1276	1442	1665
$\tau\tau$ [pb]	$4 \cdot 10^{-1}$	$2 \cdot 10^{-2}$	$5 \cdot 10^{-3}$	$2 \cdot 10^{-3}$	$1 \cdot 10^{-3}$	$9 \cdot 10^{-4}$	$8 \cdot 10^{-4}$	$7 \cdot 10^{-4}$	$5 \cdot 10^{-4}$
$\mu\mu, ee$ [pb]		$4 \cdot 10^{-4}$	$1 \cdot 10^{-4}$	$9 \cdot 10^{-5}$	$4 \cdot 10^{-5}$	$4 \cdot 10^{-5}$	$4 \cdot 10^{-5}$	$2 \cdot 10^{-5}$	$2 \cdot 10^{-5}$
$\gamma\gamma$ [pb]		$4 \cdot 10^{-4}$	$1 \cdot 10^{-4}$	$4 \cdot 10^{-5}$	$4 \cdot 10^{-5}$	$4 \cdot 10^{-5}$	$1 \cdot 10^{-5}$	$2 \cdot 10^{-5}$	$2 \cdot 10^{-5}$
$b\bar{b}$ [pb]						$8 \cdot 10^{-3}$	$6 \cdot 10^{-3}$	$8 \cdot 10^{-3}$	$4 \cdot 10^{-3}$
$t\bar{t}$ [pb]			1.5	0.1	$6 \cdot 10^{-2}$	$4 \cdot 10^{-2}$	$3 \cdot 10^{-2}$	$1 \cdot 10^{-2}$	$6 \cdot 10^{-3}$

Table 27: Estimated reach $\sigma \times \text{BR}$ for scalar or pseudoscalar resonance searches through various inclusive production channels at a 100 TeV collider.

m [GeV]	1862	2280	2412	3225	3724	4561	7397
$\tau\tau$ [pb]	$4 \cdot 10^{-4}$	$4 \cdot 10^{-4}$	$4 \cdot 10^{-4}$	$3 \cdot 10^{-4}$			
$\mu\mu, ee$ [pb]	$1 \cdot 10^{-5}$	$1 \cdot 10^{-5}$	$1 \cdot 10^{-5}$	$4 \cdot 10^{-6}$	$2 \cdot 10^{-6}$	$2 \cdot 10^{-6}$	$2 \cdot 10^{-6}$
$\gamma\gamma$ [pb]	$9 \cdot 10^{-6}$	$1 \cdot 10^{-5}$	$6 \cdot 10^{-6}$	$6 \cdot 10^{-6}$	$1 \cdot 10^{-5}$	$1 \cdot 10^{-5}$	
$b\bar{b}$ [pb]	$2 \cdot 10^{-3}$	$2 \cdot 10^{-3}$	$2 \cdot 10^{-3}$	$4 \cdot 10^{-4}$	$4 \cdot 10^{-4}$	$1 \cdot 10^{-4}$	$8 \cdot 10^{-5}$
$t\bar{t}$ [pb]	$3 \cdot 10^{-3}$	$2 \cdot 10^{-3}$	$2 \cdot 10^{-3}$	$4 \cdot 10^{-4}$	$4 \cdot 10^{-4}$	$3 \cdot 10^{-4}$	$1 \cdot 10^{-4}$

Table 28: Estimated reach $\sigma \times \text{BR}$ for scalar or pseudoscalar resonance searches through various inclusive production channels at a 100 TeV collider.

For certain mass points, specifically 790, 916, 962, 993, 1009, 1075, 1621, and 2002 GeV, the projected sensitivities are not explicitly calculated, as they lie close to masses for which detailed estimates are already provided in tables 23, 25 and 27. Given the expected smooth behavior of the collider sensitivity with respect to mass, the projected reach at these points is not expected to differ significantly from neighboring masses. In addition, the masses 14667, 17415, 21971, and 24628 GeV are not included in sensitivity estimates, as they lie well beyond the current reach of the 13 TeV LHC.

8.2 Lagrangian for scalar and pseudoscalar mesons

To investigate the spectrum of the DTC paradigm, we write the following Lagrangian defining the interactions of different scalar states,

$$\mathcal{L} = - \sum_f \lambda_f \frac{m_f}{F_{th}} \bar{\psi}_f \psi_f \Phi, \quad (143)$$

where F_{th} represents a decay constant of a generic non-Abelian strong dynamics, λ_f are dimensionless constants, and Φ is a generic composite scalar of the strong gauge dynamics. For a generic composite pseudoscalar

η ,

$$\mathcal{L} = -i \sum_f \lambda_f \frac{m_f}{F_{th}} \bar{\psi}_f \gamma_5 \psi_f \eta. \quad (144)$$

We use $\lambda_f = 4\pi$ for producing collider signatures in this work. Moreover, we assume that the scalar and pseudoscalar mesons strongly couple to the $t\bar{t}$, $b\bar{b}$, and $\tau\tau$ modes. This is assumed to produce maximum sensitive signatures for the HL-LHC, HE-LHC, and a future 100 TeV collider, which is not possible with $\lambda_f = 1$. The accessible modes for the HL-LHC, HE-LHC, and a 100 TeV collider are marked within the box (\square) in this work.

The production cross section for a scalar or pseudoscalar resonance $\phi = \phi_S$ (scalar), ϕ_P (pseudoscalar) of mass M and decaying to a final state X is given by [65],

$$\sigma(pp \rightarrow \phi \rightarrow X) = \frac{1}{M_s} C_{gg} \Gamma(\phi \rightarrow gg) BR(\phi \rightarrow X), \quad (145)$$

where C_{gg} is the weight factor accounting for the PDFs of the proton and the color factors, and s denotes the squared center of mass energy. The values of the C_{gg} are determined from the PDFs as follows [65],

$$C_{gg} = \frac{\pi^2}{8} \int_{M^2/s}^1 \frac{dx}{x} g(x) g\left(\frac{M^2}{sx}\right). \quad (146)$$

We use the MSTW2008 PDF [66] to generate the production cross-sections of these particles through various modes.

The partial decay widths to $f\bar{f}$ are given by [65],

$$\Gamma(\phi_S \rightarrow f\bar{f}) = \frac{N_C^f g_{sff}^2 m_f^2(M) M}{8\pi v^2} \left(1 - \frac{4m_f^2}{M^2}\right)^{3/2}, \quad (147)$$

$$\Gamma(\phi_P \rightarrow f\bar{f}) = \frac{N_C^f g_{pff}^2 m_f^2(M) M}{8\pi v^2} \left(1 - \frac{4m_f^2}{M^2}\right)^{1/2}, \quad (148)$$

where g_{sff} , g_{pff} are the ratios between the quark coupling to the spin-0 particle and the SM Yukawa couplings and the color factor $N_C^f = 3$ for quarks and 1 for leptons.

The partial decay widths to gg and $\gamma\gamma$ are expressed as [65],

$$\Gamma(\phi_S \rightarrow gg) = \frac{\alpha_s^2 M^3}{32\pi^3 v^2} \left| \sum_f g_{sff} F_S \left(\frac{M^2}{4m_f^2}\right) \right|^2, \quad (149)$$

$$\Gamma(\phi_P \rightarrow gg) = \frac{\alpha_s^2 M^3}{32\pi^3 v^2} \left| \sum_f g_{pff} F_P \left(\frac{M^2}{4m_f^2}\right) \right|^2, \quad (150)$$

$$\Gamma(\phi_S \rightarrow \gamma\gamma) = \frac{\alpha^2 M^3}{256\pi^3 v^2} \left| \sum_f 2N_C^f Q_f^2 g_{sff} F_S \left(\frac{M^2}{4m_f^2}\right) \right|^2, \quad (151)$$

$$\Gamma(\phi_P \rightarrow \gamma\gamma) = \frac{\alpha^2 M^3}{256\pi^3 v^2} \left| \sum_f 2N_C^f Q_f^2 g_{pff} F_P \left(\frac{M^2}{4m_f^2}\right) \right|^2. \quad (152)$$

The form factors $F_S(x)$ and $F_P(x)$ can be written as,

$$F_S(x) = x^{-1} (1 + (1 - x^{-1})f(x)), \quad (153)$$

$$F_P(x) = x^{-1} f(x). \quad (154)$$

where,

$$f(x) = \begin{cases} \arcsin^2(\sqrt{x}), & x \leq 1 \\ -\frac{1}{4} \left(\log \left(\frac{\sqrt{x} + \sqrt{x-1}}{\sqrt{x} - \sqrt{x-1}} \right) - i\pi \right)^2, & x > 1 \end{cases}$$

and $x = \frac{M^2}{4m_f^2}$.

8.3 Signatures of the DTC-paradigm when the SHVM is accommodated within its framework

We apply the fit results from sub-section 4.2 in the case when the SHVM is accommodated within the DTC paradigm. These are obtained for three scenarios given, as $\Lambda_{\text{DTC}} \approx \Lambda$, $\Lambda_{\text{DTC}} < \Lambda$, and $\Lambda_{\text{DTC}} > \Lambda$ with three choices of multifermionic condensates, denoted by N_2 , N_4 , and N_6 .

In this instance, N_6 , $\Lambda_{\text{DTC}} = 500 \text{ GeV}$, $\Lambda = 500 \text{ GeV}$ yield the minimum number of colours, $N_{\text{TC}} = 2, N_{\text{DTC}} = 2, N_{\text{D}} = 3$. We observe that as $\Lambda_{\text{DTC}} = \Lambda$, and number of colours are also almost same, there is no difference between the signatures of the scalars and pseudoscalars of the DTC and DQCD-dynamics. The variations of cross-sections of the DTC-pions Π_{DTC} for N_4 and N_6 , are shown in figure 7.

The benchmark predictions for the production of DTC-pion and DQCD-pion for $\Lambda_{\text{DTC}} = \Lambda$ for heavy and low masses are shown in tables 29 and 30 at the HL-LHC for the scenarios N_4 and N_6 . Moreover, the same results are shown in tables 31-34 for the HE-LHC and a 100 TeV collider such as the FCC-h.

$m_{\Pi_{\text{DTC},\text{D}}} [\text{GeV}]$	$N_{\text{DTC},\text{D}} = 9$		$N_{\text{DTC}} = 2$		$N_{\text{D}} = 3$	
	500	1000	500	1000	500	1000
$\tau\tau$ [pb]	0.2	$1.1 \cdot 10^{-3}$	0.8	$4.9 \cdot 10^{-3}$	0.5	$3.3 \cdot 10^{-3}$
$\mu\mu$ [pb]	$6.1 \cdot 10^{-4}$	$3.8 \cdot 10^{-6}$	$2.7 \cdot 10^{-3}$	$1.7 \cdot 10^{-5}$	$1.8 \cdot 10^{-3}$	$1.1 \cdot 10^{-5}$
ee [pb]	$1.4 \cdot 10^{-8}$	$9.0 \cdot 10^{-11}$	$6.4 \cdot 10^{-8}$	$4.0 \cdot 10^{-10}$	$4.3 \cdot 10^{-8}$	$2.7 \cdot 10^{-10}$
$\gamma\gamma$ [pb]	0.7	$1.1 \cdot 10^{-3}$	3.2	$5.0 \cdot 10^{-3}$	2.1	$3.3 \cdot 10^{-3}$
$b\bar{b}$ [pb]	2.9	$1.8 \cdot 10^{-2}$	13	$8.1 \cdot 10^{-2}$	8.6	$5.4 \cdot 10^{-2}$
$t\bar{t}$ [pb]	3901	29	17554	132	11703	88

Table 29: Benchmark points for inclusive Π_{DTC} and Π_{D} production channels for high mass $m_{\Pi_{\text{DTC},\text{D}}}$ at the 14 TeV HL-LHC for $N_{\text{DTC}} = 9, 2$, $\Lambda_{\text{DTC}} = 500 \text{ GeV}$ and $N_{\text{D}} = 9, 3$, $\Lambda = 500 \text{ GeV}$.

$m_{\Pi_{\text{DTC},\text{D}}} [\text{GeV}]$	$N_{\text{DTC},\text{D}} = 9$		$N_{\text{DTC}} = 2$		$N_{\text{D}} = 3$	
	20	60	20	60	20	60
$\tau\tau$ [pb]	9716	252	43721	1132	29148	755
$\gamma\gamma$ [pb]	3.8	0.2	17.2	0.9	11	0.6

Table 30: Benchmark points for inclusive Π_{DTC} and Π_{D} production channels at the 14 TeV HL-LHC for low mass $m_{\Pi_{\text{DTC},\text{D}}}$ for $N_{\text{DTC}} = 9, 2$, $\Lambda_{\text{DTC}} = 500 \text{ GeV}$ and $N_{\text{D}} = 9, 3$, $\Lambda = 500 \text{ GeV}$.

8.3.1 Case $\Lambda_{\text{DTC}} \approx \Lambda$

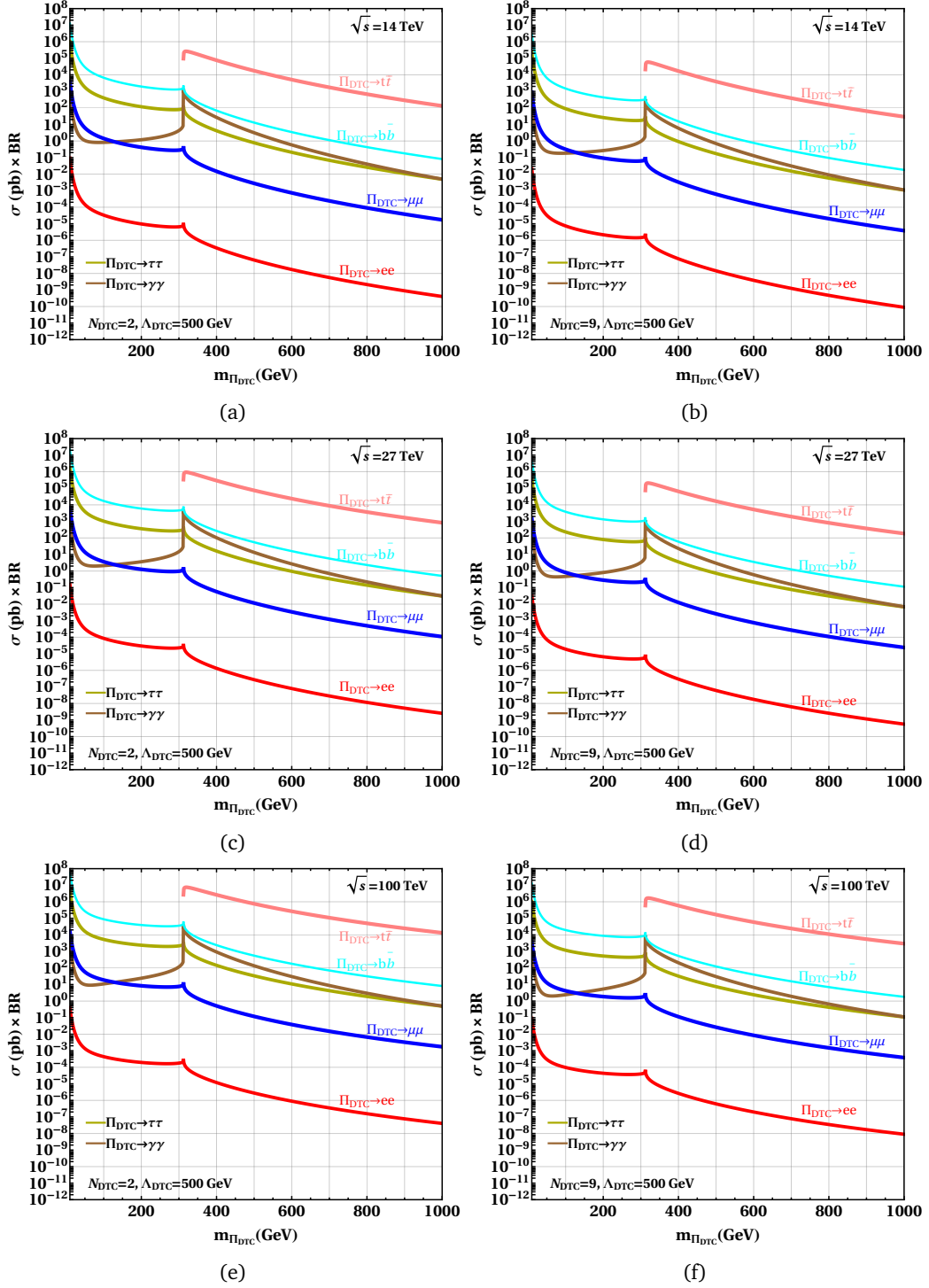


Figure 7: $\sigma \times \text{BR}$ of the various possible decay modes of the Π_{DTC} into photons, quark pairs and lepton pairs in the SHVM mechanism for $\Lambda_{\text{DTC}} = 500$ GeV at the 14 TeV HL-LHC for (7a) $N_{\text{DTC}} = 2$ (7b) $N_{\text{DTC}} = 9$, the 27 TeV HE-LHC for (7c) $N_{\text{DTC}} = 2$ (7d) $N_{\text{DTC}} = 9$, and a 100 TeV future collider for (7e) $N_{\text{DTC}} = 2$ (7f) $N_{\text{DTC}} = 9$.

$m_{\Pi_{\text{DTC},D}}$ [GeV]	$N_{\text{DTC},D} = 9$		$N_{\text{DTC}} = 2$		$N_D = 3$	
	500	1000	500	1000	500	1000
$\tau\tau$ [pb]	0.7	$6.8 \cdot 10^{-3}$	3.3	$3.1 \cdot 10^{-2}$	2.2	$2.0 \cdot 10^{-2}$
$\mu\mu$ [pb]	$2.6 \cdot 10^{-3}$	$2.4 \cdot 10^{-5}$	$1.1 \cdot 10^{-2}$	$1.1 \cdot 10^{-4}$	$7.8 \cdot 10^{-3}$	$7.2 \cdot 10^{-5}$
ee [pb]	$6.1 \cdot 10^{-8}$	$5.6 \cdot 10^{-10}$	$2.7 \cdot 10^{-7}$	$2.5 \cdot 10^{-9}$	$1.8 \cdot 10^{-7}$	$1.7 \cdot 10^{-9}$
$\gamma\gamma$ [pb]	3.0	$7.0 \cdot 10^{-3}$	13.4	$3.1 \cdot 10^{-2}$	8.9	$2.1 \cdot 10^{-2}$
$b\bar{b}$ [pb]	12.2	0.1	55	0.5	37	0.3
$t\bar{t}$ [pb]	16561	185	74526	831	49684	554

Table 31: Benchmark points for inclusive Π_{DTC} and Π_D production channels for high mass $m_{\Pi_{\text{DTC},D}}$ at the 27 TeV HE-LHC for $N_{\text{DTC}} = 9, 2$, $\Lambda_{\text{DTC}} = 500$ GeV and $N_D = 9, 3$, $\Lambda = 500$ GeV.

$m_{\Pi_{\text{DTC},D}}$ [GeV]	$N_{\text{DTC},D} = 9$		$N_{\text{DTC}} = 2$		$N_D = 3$	
	20	60	20	60	20	60
$\tau\tau$ [pb]	18530	582	83387	2618	55591	1745
$\gamma\gamma$ [pb]	7.3	0.5	33	2.1	22	1.4

Table 32: Benchmark points for inclusive Π_{DTC} and Π_D production channels at the 27 TeV HE-LHC for low mass $m_{\Pi_{\text{DTC},D}}$ for $N_{\text{DTC}} = 9, 2$, $\Lambda_{\text{DTC}} = 500$ GeV and $N_D = 9, 3$, $\Lambda = 500$ GeV.

$m_{\Pi_{\text{DTC},D}}$ [GeV]	$N_{\text{DTC},D} = 9$		$N_{\text{DTC}} = 2$		$N_D = 3$	
	500	1000	500	1000	500	1000
$\tau\tau$ [pb]	7.4	0.1	33	0.5	22.3	0.3
$\mu\mu$ [pb]	$2.6 \cdot 10^{-2}$	$3.9 \cdot 10^{-4}$	0.1	$1.7 \cdot 10^{-3}$	$7.9 \cdot 10^{-2}$	$1.2 \cdot 10^{-3}$
ee [pb]	$6.2 \cdot 10^{-7}$	$9.0 \cdot 10^{-9}$	$2.8 \cdot 10^{-6}$	$4.1 \cdot 10^{-8}$	$1.8 \cdot 10^{-6}$	$2.7 \cdot 10^{-8}$
$\gamma\gamma$ [pb]	30	0.1	136	0.5	90	0.3
$b\bar{b}$ [pb]	123	1.8	556	8.1	371	5.4
$t\bar{t}$ [pb]	$1.7 \cdot 10^5$	2952	$7.5 \cdot 10^5$	13282	$5.0 \cdot 10^5$	8855

Table 33: Benchmark points for inclusive Π_{DTC} and Π_D production channels for high mass $m_{\Pi_{\text{DTC},D}}$ at a 100 TeV collider for $N_{\text{DTC}} = 9, 2$, $\Lambda_{\text{DTC}} = 500$ GeV and $N_D = 9, 3$, $\Lambda = 500$ GeV.

$m_{\Pi_{\text{DTC},D}}$ [GeV]	$N_{\text{DTC},D} = 9$		$N_{\text{DTC}} = 2$		$N_D = 3$	
	20	60	20	60	20	60
$\tau\tau$ [pb]	59007	2541	$2.7 \cdot 10^5$	11433	$1.8 \cdot 10^5$	7622
$\gamma\gamma$ [pb]	23	2.0	104	9.2	67	6.1

Table 34: Benchmark points for inclusive Π_{DTC} and Π_D production channels at the 100 TeV collider for low mass $m_{\Pi_{\text{DTC},D}}$ for $N_{\text{DTC}} = 9, 2$, $\Lambda_{\text{DTC}} = 500$ GeV and $N_D = 9, 3$, $\Lambda = 500$ GeV.

The benchmark values of the signatures of production of TC-eta, DTC-eta and DQCD-eta at the HL-LHC are shown in table 35, and the same results for the HE-LHC and a future 100 TeV collider are recorded in tables 36-37. We notice that the masses of the TC-eta, DTC-eta and DQCD-eta are exactly predicted by the scaling relations. Therefore, we do not show the variation of corresponding cross-sections for the TC-eta, DTC-eta and DQCD-eta.

$m_{\eta_{\text{TC,DTC,D}}} [\text{GeV}]$	$N_{\text{TC}} = 2, \Lambda_{\text{TC}} = 529 \text{ GeV}$ 2412	$N_{\text{DTC}} = 2, \Lambda_{\text{DTC}} = 500 \text{ GeV}$ 2280	$N_{\text{D}} = 3, \Lambda = 500 \text{ GeV}$ 1862
$\tau\tau$ [pb]	$3.0 \cdot 10^{-6}$	$5.6 \cdot 10^{-6}$	$2.2 \cdot 10^{-5}$
$\mu\mu$ [pb]	$1.0 \cdot 10^{-8}$	$2.0 \cdot 10^{-8}$	$7.9 \cdot 10^{-8}$
ee [pb]	$2.4 \cdot 10^{-13}$	$4.6 \cdot 10^{-13}$	$1.9 \cdot 10^{-12}$
$\gamma\gamma$ [pb]	$5.7 \cdot 10^{-7}$	$1.2 \cdot 10^{-6}$	$7.0 \cdot 10^{-6}$
$b\bar{b}$ [pb]	$4.9 \cdot 10^{-5}$	$9.2 \cdot 10^{-5}$	$3.7 \cdot 10^{-4}$
$t\bar{t}$ [pb]	$8.3 \cdot 10^{-2}$	0.2	0.6

Table 35: Benchmark points for $\eta_{\text{TC,DTC,D}}$ production channels at the 14 TeV HL-LHC for $N_{\text{TC}} = 2, \Lambda_{\text{TC}} = 529 \text{ GeV}$, $N_{\text{DTC}} = 2, \Lambda_{\text{DTC}} = 500 \text{ GeV}$ and $N_{\text{D}} = 3, \Lambda = 500 \text{ GeV}$.

$m_{\eta_{\text{TC,DTC,D}}} [\text{GeV}]$	$N_{\text{TC}} = 2, \Lambda_{\text{TC}} = 529 \text{ GeV}$ 2412	$N_{\text{DTC}} = 2, \Lambda_{\text{DTC}} = 500 \text{ GeV}$ 2280	$N_{\text{D}} = 3, \Lambda = 500 \text{ GeV}$ 1862
$\tau\tau$ [pb]	$4.6 \cdot 10^{-5}$	$8.1 \cdot 10^{-5}$	$2.5 \cdot 10^{-4}$
$\mu\mu$ [pb]	$1.7 \cdot 10^{-7}$	$2.9 \cdot 10^{-7}$	$8.8 \cdot 10^{-7}$
ee [pb]	$3.9 \cdot 10^{-12}$	$6.7 \cdot 10^{-12}$	$2.1 \cdot 10^{-11}$
$\gamma\gamma$ [pb]	$9.0 \cdot 10^{-6}$	$1.7 \cdot 10^{-5}$	$7.8 \cdot 10^{-5}$
$b\bar{b}$ [pb]	$7.8 \cdot 10^{-4}$	$1.3 \cdot 10^{-3}$	$4.1 \cdot 10^{-3}$
$t\bar{t}$ [pb]	1.3	2.3	7.0

Table 36: Benchmark points for $\eta_{\text{TC,DTC,D}}$ production channels at the 27 TeV HE-LHC for $N_{\text{TC}} = 2, \Lambda_{\text{TC}} = 529 \text{ GeV}$, $N_{\text{DTC}} = 2, \Lambda_{\text{DTC}} = 500 \text{ GeV}$ and $N_{\text{D}} = 3, \Lambda = 500 \text{ GeV}$.

$m_{\eta_{\text{TC,DTC,D}}} [\text{GeV}]$	$N_{\text{TC}} = 2, \Lambda_{\text{TC}} = 529 \text{ GeV}$ 2412	$N_{\text{DTC}} = 2, \Lambda_{\text{DTC}} = 500 \text{ GeV}$ 2280	$N_{\text{D}} = 3, \Lambda = 500 \text{ GeV}$ 1862
$\tau\tau$ [pb]	$1.9 \cdot 10^{-3}$	$3.0 \cdot 10^{-3}$	$7.2 \cdot 10^{-3}$
$\mu\mu$ [pb]	$6.6 \cdot 10^{-6}$	$1.1 \cdot 10^{-5}$	$2.5 \cdot 10^{-5}$
ee [pb]	$1.5 \cdot 10^{-10}$	$2.5 \cdot 10^{-10}$	$5.9 \cdot 10^{-10}$
$\gamma\gamma$ [pb]	$3.6 \cdot 10^{-4}$	$6.4 \cdot 10^{-4}$	$2.2 \cdot 10^{-3}$
$b\bar{b}$ [pb]	$3.1 \cdot 10^{-2}$	$5.0 \cdot 10^{-2}$	0.1
$t\bar{t}$ [pb]	52	84	200

Table 37: Benchmark points for $\eta_{\text{TC,DTC,D}}$ production channels at a 100 TeV collider for $N_{\text{TC}} = 2, \Lambda_{\text{TC}} = 529 \text{ GeV}$, $N_{\text{DTC}} = 2, \Lambda_{\text{DTC}} = 500 \text{ GeV}$ and $N_{\text{D}} = 3, \Lambda = 500 \text{ GeV}$.

Our benchmark predictions for the scalars of the DTC paradigm are shown in table 38 at the HL-LHC, HE-LHC, and a 100 TeV future collider. The lowest scalar, the dark-Higgs, corresponding to the DQCD-dynamics for $\Delta\chi_{\text{D}} = 2$, is too heavy to be produced at any collider, as seen in table 11. This is a generic feature of the SHVM. On the other side for $\Delta\chi_{\text{D}} = -2$, the dark-Higgs corresponding to the DQCD-dynamics, is very light, and maybe a dark-matter candidate.

$\Delta\chi_{DTC}$ $m_{H_{DTC}}$ [GeV]	HL-LHC [14 TeV, 3 ab ⁻¹]		HE-LHC [27 TeV, 15 ab ⁻¹]		100 TeV, 30 ab ⁻¹	
	+2	-2	+2	-2	+2	-2
$\tau\tau$ [pb]	$7.5 \cdot 10^{-4}$	$2.6 \cdot 10^{-2}$	$5.7 \cdot 10^{-3}$	0.1	0.1	1.9
$\mu\mu$ [pb]	$2.6 \cdot 10^{-6}$	$9.2 \cdot 10^{-5}$	$2.0 \cdot 10^{-5}$	$5.0 \cdot 10^{-4}$	$3.9 \cdot 10^{-4}$	$6.7 \cdot 10^{-3}$
ee [pb]	$6.2 \cdot 10^{-11}$	$2.2 \cdot 10^{-9}$	$4.7 \cdot 10^{-10}$	$1.2 \cdot 10^{-8}$	$9.2 \cdot 10^{-9}$	$1.6 \cdot 10^{-7}$
$\gamma\gamma$ [pb]	$4.5 \cdot 10^{-4}$	$3.4 \cdot 10^{-2}$	$3.4 \cdot 10^{-3}$	0.2	$6.7 \cdot 10^{-2}$	2.4
$b\bar{b}$ [pb]	$1.2 \cdot 10^{-2}$	0.4	$9.4 \cdot 10^{-2}$	2.3	1.8	31
$t\bar{t}$ [pb]	20	590	148	3176	2910	42690

Table 38: Benchmark points for H_{DTC} production channels at the 14 TeV HL-LHC, 27 TeV HE-LHC and the 100 TeV collider for $N_{DTC} = 2$, $\Lambda_{DTC} = 500$ GeV for the scenario N_6 .

8.3.2 $\Lambda > \Lambda_{DTC}$

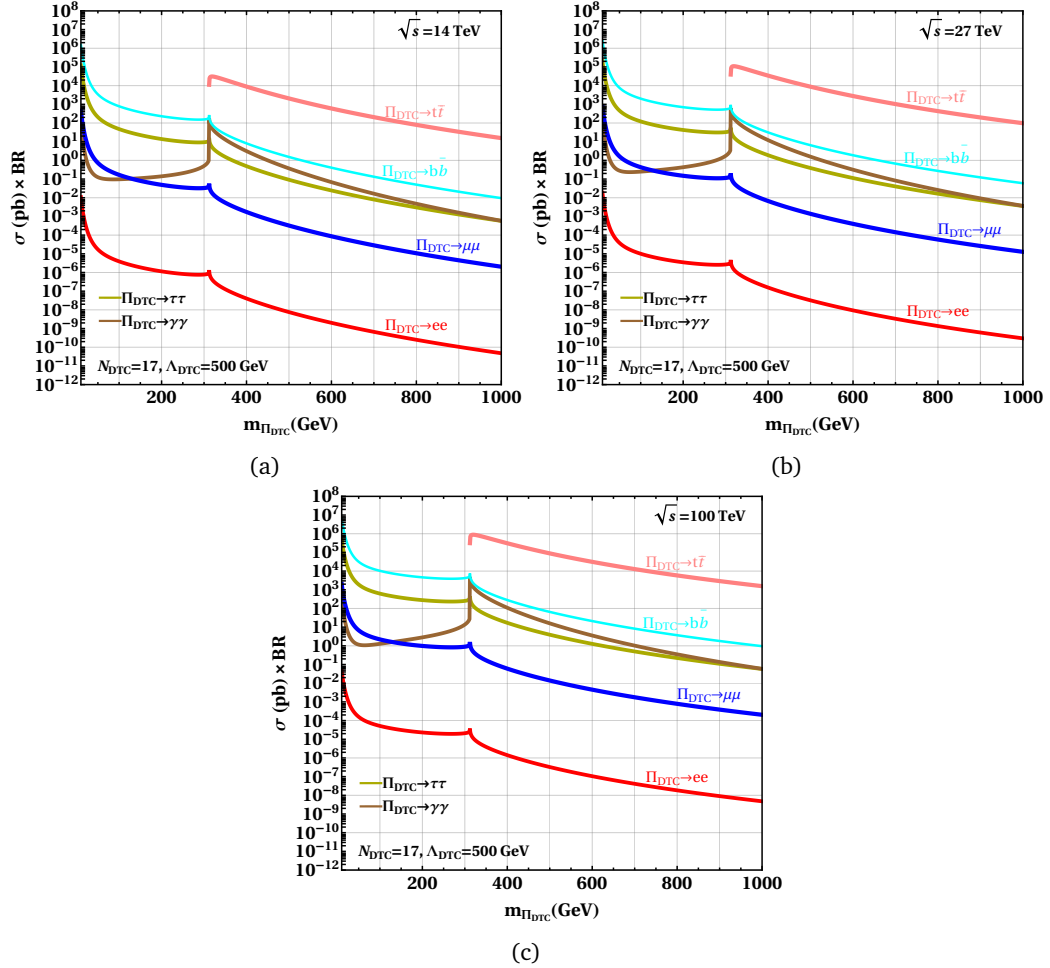


Figure 8: $\sigma \times BR$ of the various possible decay modes of the Π_{DTC} into photons, quark pairs and lepton pairs for $N_{DTC} = 17$, $\Lambda_{DTC} = 500$ GeV at the (8a) 14 TeV HL-LHC, (8b) 27 TeV HE-LHC, and (8c) a 100 TeV collider.

We present the collider signatures for the scenario N_6 , which is given by,

$$N_{\text{TC}} = 12, N_{\text{DTC}} = 17, N_{\text{D}} = 15, \Lambda_{\text{TC}} = 296 \text{ GeV}, \Lambda_{\text{DTC}} = 500 \text{ GeV}, \Lambda = 1 \text{ TeV}. \quad (155)$$

The production cross sections of DTC-pion for various modes are shown in figure 8 for the HL-LHC, HE-LHC, and a 100 TeV future collider. The same is shown in figure 9 for DQCD-pion. The benchmark predictions for signatures of the DTC- and DQCD-pion are shown in table 39 for the HL-LHC. For low masses of DTC and DQCD-pions, the benchmark predictions for the signatures are given in table 40. We show the same benchmark predictions for signatures of DTC and DQCD-pions for the HE-LHC and a future 100 TeV collider in tables 41-44. For signatures for DTC eta and DQCD-eta in different modes, our predictions for the HL-LHC, HE-LHC, and a future 100 TeV collider are given in tables 45-47. Our benchmark predictions for the signatures of the lowest lying DTC-scalar, i.e., the DTC-Higgs are given in table 48.

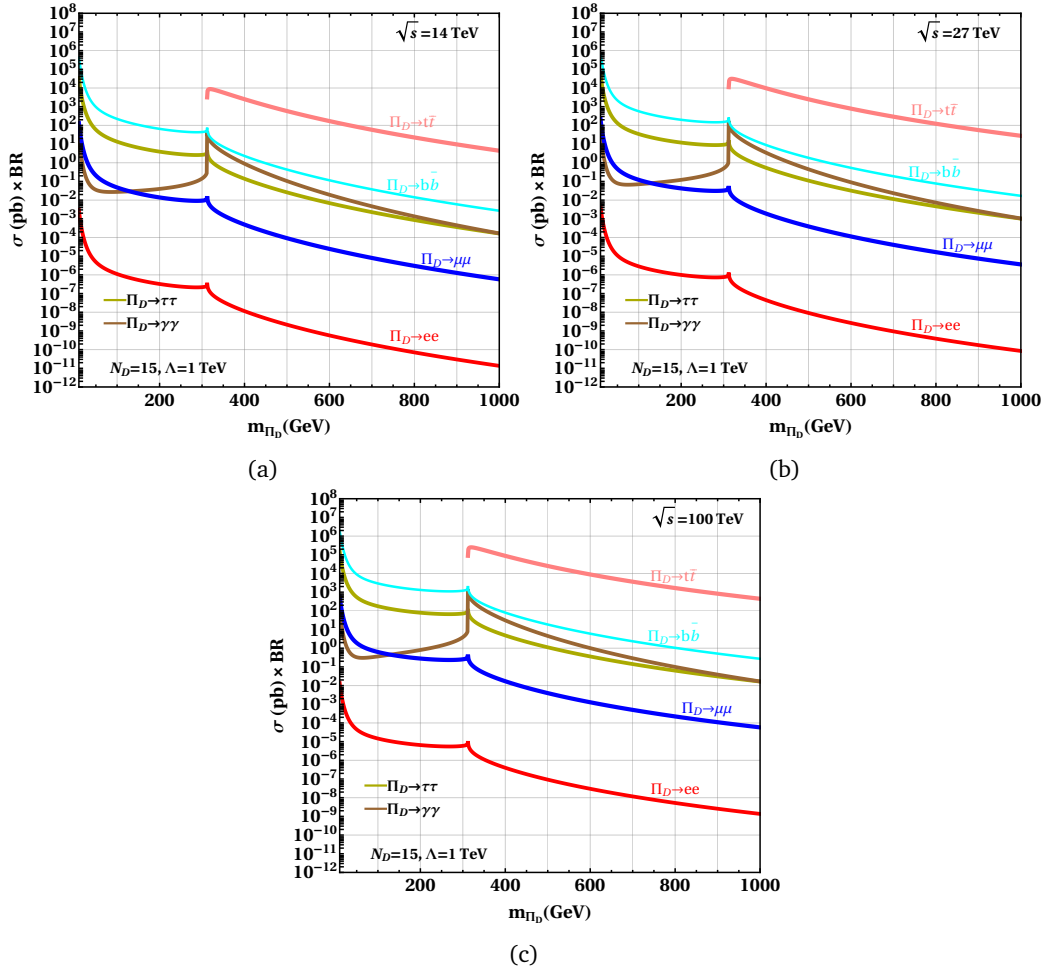


Figure 9: $\sigma \times \text{BR}$ of the various possible decay modes of the Π_{D} into photons, quark pairs, and lepton pairs for $N_{\text{D}} = 15, \Lambda = 1 \text{ TeV}$ at the (9a) 14 TeV HL-LHC, (9b) 27 TeV HE-LHC, and (9c) a 100 TeV collider.

$m_{\Pi_{\text{DTC},D}}$ [GeV]	$N_{\text{DTC}} = 17, \Lambda_{\text{DTC}} = 500 \text{ GeV}$		$N_D = 15, \Lambda = 1 \text{ TeV}$	
	500	1000	500	1000
$\tau\tau$ [pb]	$9.2 \cdot 10^{-2}$	$5.8 \cdot 10^{-4}$	$2.6 \cdot 10^{-2}$	$1.6 \cdot 10^{-4}$
$\mu\mu$ [pb]	$3.2 \cdot 10^{-4}$	$2.0 \cdot 10^{-6}$	$9.2 \cdot 10^{-5}$	$5.8 \cdot 10^{-7}$
ee [pb]	$7.6 \cdot 10^{-9}$	$4.8 \cdot 10^{-11}$	$2.1 \cdot 10^{-9}$	$1.3 \cdot 10^{-11}$
$\gamma\gamma$ [pb]	0.4	$5.9 \cdot 10^{-4}$	0.1	$1.7 \cdot 10^{-4}$
$b\bar{b}$ [pb]	1.5	$9.6 \cdot 10^{-3}$	0.4	$2.7 \cdot 10^{-3}$
$t\bar{t}$ [pb]	2065	16	585	4.4

Table 39: Benchmark points for $\Pi_{\text{DTC},D}$ production channels for high mass $m_{\Pi_{\text{DTC},D}}$ at the 14 TeV HL-LHC for $N_{\text{DTC}} = 17, \Lambda_{\text{DTC}} = 500 \text{ GeV}$ and $N_D = 15, \Lambda = 1 \text{ TeV}$.

$m_{\Pi_{\text{DTC},D}}$ [GeV]	$N_{\text{DTC}} = 17, \Lambda_{\text{DTC}} = 500 \text{ GeV}$		$N_D = 15, \Lambda = 1 \text{ TeV}$	
	20	60	20	60
$\tau\tau$ [pb]	5144	133	1457	38
$\gamma\gamma$ [pb]	2.0	0.1	0.6	$3.0 \cdot 10^{-2}$

Table 40: Benchmark points for inclusive $\Pi_{\text{DTC},D}$ production channel at the 14 TeV HL-LHC for low mass $m_{\Pi_{\text{DTC},D}}$ for $N_{\text{DTC}} = 17, \Lambda_{\text{DTC}} = 500 \text{ GeV}$ and $N_D = 15, \Lambda = 1 \text{ TeV}$.

$m_{\Pi_{\text{DTC},D}}$ [GeV]	$N_{\text{DTC}} = 17, \Lambda_{\text{DTC}} = 500 \text{ GeV}$		$N_D = 15, \Lambda = 1 \text{ TeV}$	
	500	1000	500	1000
$\tau\tau$ [pb]	0.4	$3.6 \cdot 10^{-3}$	0.1	$1.0 \cdot 10^{-3}$
$\mu\mu$ [pb]	$1.4 \cdot 10^{-3}$	$1.3 \cdot 10^{-5}$	$3.9 \cdot 10^{-4}$	$3.6 \cdot 10^{-6}$
ee [pb]	$3.2 \cdot 10^{-8}$	$3.0 \cdot 10^{-10}$	$9.1 \cdot 10^{-9}$	$8.5 \cdot 10^{-11}$
$\gamma\gamma$ [pb]	1.6	$3.7 \cdot 10^{-3}$	0.4	$1.0 \cdot 10^{-3}$
$b\bar{b}$ [pb]	6.5	$6.0 \cdot 10^{-2}$	1.8	$1.7 \cdot 10^{-2}$
$t\bar{t}$ [pb]	8768	98	2484	28

Table 41: Benchmark points for $\Pi_{\text{DTC},D}$ production channels for high mass $m_{\Pi_{\text{DTC},D}}$ at the 27 TeV HE-LHC for $N_{\text{DTC}} = 17, \Lambda_{\text{DTC}} = 500 \text{ GeV}$ and $N_D = 15, \Lambda = 1 \text{ TeV}$.

$m_{\Pi_{\text{DTC},D}}$ [GeV]	$N_{\text{DTC}} = 17, \Lambda_{\text{DTC}} = 500 \text{ GeV}$		$N_D = 15, \Lambda = 1 \text{ TeV}$	
	20	60	20	60
$\tau\tau$ [pb]	9810	308	2780	87
$\gamma\gamma$ [pb]	3.9	0.2	1.1	$7.0 \cdot 10^{-2}$

Table 42: Benchmark points for inclusive $\Pi_{\text{DTC},D}$ production channel at the 27 TeV HE-LHC for low mass $m_{\Pi_{\text{DTC},D}}$ for $N_{\text{DTC}} = 17, \Lambda_{\text{DTC}} = 500 \text{ GeV}$ and $N_D = 15, \Lambda = 1 \text{ TeV}$.

$m_{\Pi_{\text{DTC},\text{D}}} [\text{GeV}]$	$N_{\text{DTC}} = 17, \Lambda_{\text{DTC}} = 500 \text{ GeV}$		$N_{\text{D}} = 15, \Lambda = 1 \text{ TeV}$	
	500	1000	500	1000
$\tau\tau$ [pb]	3.9	$5.8 \cdot 10^{-3}$	1.1	$1.6 \cdot 10^{-2}$
$\mu\mu$ [pb]	$1.4 \cdot 10^{-2}$	$2.0 \cdot 10^{-4}$	$3.9 \cdot 10^{-3}$	$5.8 \cdot 10^{-5}$
ee [pb]	$3.3 \cdot 10^{-7}$	$4.8 \cdot 10^{-9}$	$9.2 \cdot 10^{-8}$	$1.4 \cdot 10^{-9}$
$\gamma\gamma$ [pb]	16	$5.9 \cdot 10^{-2}$	4.5	$1.7 \cdot 10^{-2}$
$b\bar{b}$ [pb]	65.4	1.0	19	0.3
$t\bar{t}$ [pb]	88737	1563	25142	443

Table 43: Benchmark points for $\Pi_{\text{DTC},\text{D}}$ production channels for high mass $m_{\Pi_{\text{DTC},\text{D}}}$ at a 100 TeV collider for $N_{\text{DTC}} = 17, \Lambda_{\text{DTC}} = 500 \text{ GeV}$ and $N_{\text{D}} = 15, \Lambda = 1 \text{ TeV}$.

$m_{\Pi_{\text{DTC},\text{D}}} [\text{GeV}]$	$N_{\text{DTC}} = 17, \Lambda_{\text{DTC}} = 500 \text{ GeV}$		$N_{\text{D}} = 15, \Lambda = 1 \text{ TeV}$	
	20	60	20	60
$\tau\tau$ [pb]	31239	1345	8851	381
$\gamma\gamma$ [pb]	12	1.1	3.5	0.3

Table 44: Benchmark points for inclusive $\Pi_{\text{DTC},\text{D}}$ production channel at a 100 TeV collider for low mass $m_{\Pi_{\text{DTC},\text{D}}}$ for $N_{\text{DTC}} = 17, \Lambda_{\text{DTC}} = 500 \text{ GeV}$ and $N_{\text{D}} = 15, \Lambda = 1 \text{ TeV}$.

$m_{\eta_{\text{TC},\text{DTC},\text{D}}} [\text{GeV}]$	$N_{\text{TC}} = 12, \Lambda_{\text{TC}} = 296 \text{ GeV}$	$N_{\text{DTC}} = 17, \Lambda_{\text{DTC}} = 500 \text{ GeV}$	$N_{\text{D}} = 15, \Lambda = 1 \text{ TeV}$
	551	782	1665
$\tau\tau$ [pb]	0.2	$3.6 \cdot 10^{-3}$	$2.9 \cdot 10^{-6}$
$\mu\mu$ [pb]	$6.4 \cdot 10^{-4}$	$1.3 \cdot 10^{-5}$	$1.0 \cdot 10^{-8}$
ee [pb]	$1.5 \cdot 10^{-8}$	$2.9 \cdot 10^{-10}$	$2.4 \cdot 10^{-13}$
$\gamma\gamma$ [pb]	0.6	$5.9 \cdot 10^{-3}$	$1.1 \cdot 10^{-6}$
$b\bar{b}$ [pb]	3.0	$5.9 \cdot 10^{-2}$	$4.8 \cdot 10^{-5}$
$t\bar{t}$ [pb]	4334	94	$8.0 \cdot 10^{-2}$

Table 45: Benchmark points for $\eta_{\text{TC},\text{DTC},\text{D}}$ production channels at the 14 TeV HL-LHC for $N_{\text{TC}} = 12, \Lambda_{\text{TC}} = 296 \text{ GeV}$, $N_{\text{DTC}} = 17, \Lambda_{\text{DTC}} = 500 \text{ GeV}$ and $N_{\text{D}} = 15, \Lambda = 1 \text{ TeV}$.

$m_{\eta_{\text{TC},\text{DTC},\text{D}}} [\text{GeV}]$	$N_{\text{TC}} = 12, \Lambda_{\text{TC}} = 296 \text{ GeV}$	$N_{\text{DTC}} = 17, \Lambda_{\text{DTC}} = 500 \text{ GeV}$	$N_{\text{D}} = 15, \Lambda = 1 \text{ TeV}$
	551	782	1665
$\tau\tau$ [pb]	0.8	$1.9 \cdot 10^{-2}$	$2.8 \cdot 10^{-5}$
$\mu\mu$ [pb]	$2.9 \cdot 10^{-3}$	$6.8 \cdot 10^{-5}$	$1.0 \cdot 10^{-7}$
ee [pb]	$6.7 \cdot 10^{-8}$	$1.6 \cdot 10^{-9}$	$2.4 \cdot 10^{-12}$
$\gamma\gamma$ [pb]	2.7	$3.1 \cdot 10^{-2}$	$1.1 \cdot 10^{-5}$
$b\bar{b}$ [pb]	14	0.3	$4.7 \cdot 10^{-4}$
$t\bar{t}$ [pb]	19251	501	0.8

Table 46: Benchmark points for $\eta_{\text{TC},\text{DTC},\text{D}}$ production channels at the 27 TeV HE-LHC for $N_{\text{TC}} = 12, \Lambda_{\text{TC}} = 296 \text{ GeV}$, $N_{\text{DTC}} = 17, \Lambda_{\text{DTC}} = 500 \text{ GeV}$ and $N_{\text{D}} = 15, \Lambda = 1 \text{ TeV}$.

$m_{\eta_{\text{TC,DTC,D}}} [\text{GeV}]$	$N_{\text{TC}} = 12, \Lambda_{\text{TC}} = 296 \text{ GeV}$ 551	$N_{\text{DTC}} = 17, \Lambda_{\text{DTC}} = 500 \text{ GeV}$ 782	$N_{\text{D}} = 15, \Lambda = 1 \text{ TeV}$ 1665
$\tau\tau$ [pb]	8.7	0.3	$7.2 \cdot 10^{-4}$
$\mu\mu$ [pb]	$3.1 \cdot 10^{-2}$	$9.0 \cdot 10^{-4}$	$2.5 \cdot 10^{-6}$
ee [pb]	$7.2 \cdot 10^{-7}$	$2.1 \cdot 10^{-8}$	$5.9 \cdot 10^{-11}$
$\gamma\gamma$ [pb]	29	0.4	$2.8 \cdot 10^{-4}$
$b\bar{b}$ [pb]	144	4.2	$1.2 \cdot 10^{-2}$
$t\bar{t}$ [pb]	$2.1 \cdot 10^5$	6685	20

Table 47: Benchmark points for $\eta_{\text{TC,DTC,D}}$ production channels at the 100 TeV collider for $N_{\text{TC}} = 12, \Lambda_{\text{TC}} = 296 \text{ GeV}, N_{\text{DTC}} = 17, \Lambda_{\text{DTC}} = 500 \text{ GeV}$ and $N_{\text{D}} = 15, \Lambda = 1 \text{ TeV}$.

$\Delta\chi_{\text{DTC}}$ $m_{H_{\text{DTC}}} [\text{GeV}]$	HL-LHC [14 TeV, 3 ab^{-1}]		HE-LHC [27 TeV, 15 ab^{-1}]		100 TeV, 30 ab^{-1}	
	+2	-2	+2	-2	+2	-2
$\tau\tau$ [pb]	$3.4 \cdot 10^{-4}$	$1.1 \cdot 10^{-3}$	$2.3 \cdot 10^{-3}$	$6.6 \cdot 10^{-3}$	$3.8 \cdot 10^{-2}$	$9.8 \cdot 10^{-2}$
$\mu\mu$ [pb]	$1.2 \cdot 10^{-6}$	$4.0 \cdot 10^{-6}$	$8.0 \cdot 10^{-6}$	$2.3 \cdot 10^{-5}$	$1.4 \cdot 10^{-4}$	$3.5 \cdot 10^{-4}$
ee [pb]	$2.9 \cdot 10^{-11}$	$9.3 \cdot 10^{-11}$	$1.9 \cdot 10^{-10}$	$5.4 \cdot 10^{-10}$	$3.2 \cdot 10^{-9}$	$8.1 \cdot 10^{-9}$
$\gamma\gamma$ [pb]	$2.8 \cdot 10^{-4}$	$1.2 \cdot 10^{-3}$	$1.9 \cdot 10^{-3}$	$7.0 \cdot 10^{-3}$	$3.1 \cdot 10^{-2}$	0.1
$b\bar{b}$ [pb]	$5.7 \cdot 10^{-3}$	$1.8 \cdot 10^{-2}$	$3.8 \cdot 10^{-2}$	0.1	0.6	1.6
$t\bar{t}$ [pb]	8.7	27	57	159	964	2362

Table 48: Benchmark points for H_{DTC} production channels at the 14 TeV HL-LHC, 27 TeV HE-LHC and a 100 TeV collider for $N_{\text{DTC}} = 17, \Lambda_{\text{DTC}} = 500 \text{ GeV}$ for the scenario N_6 .

8.3.3 $\Lambda < \Lambda_{\text{DTC}}$

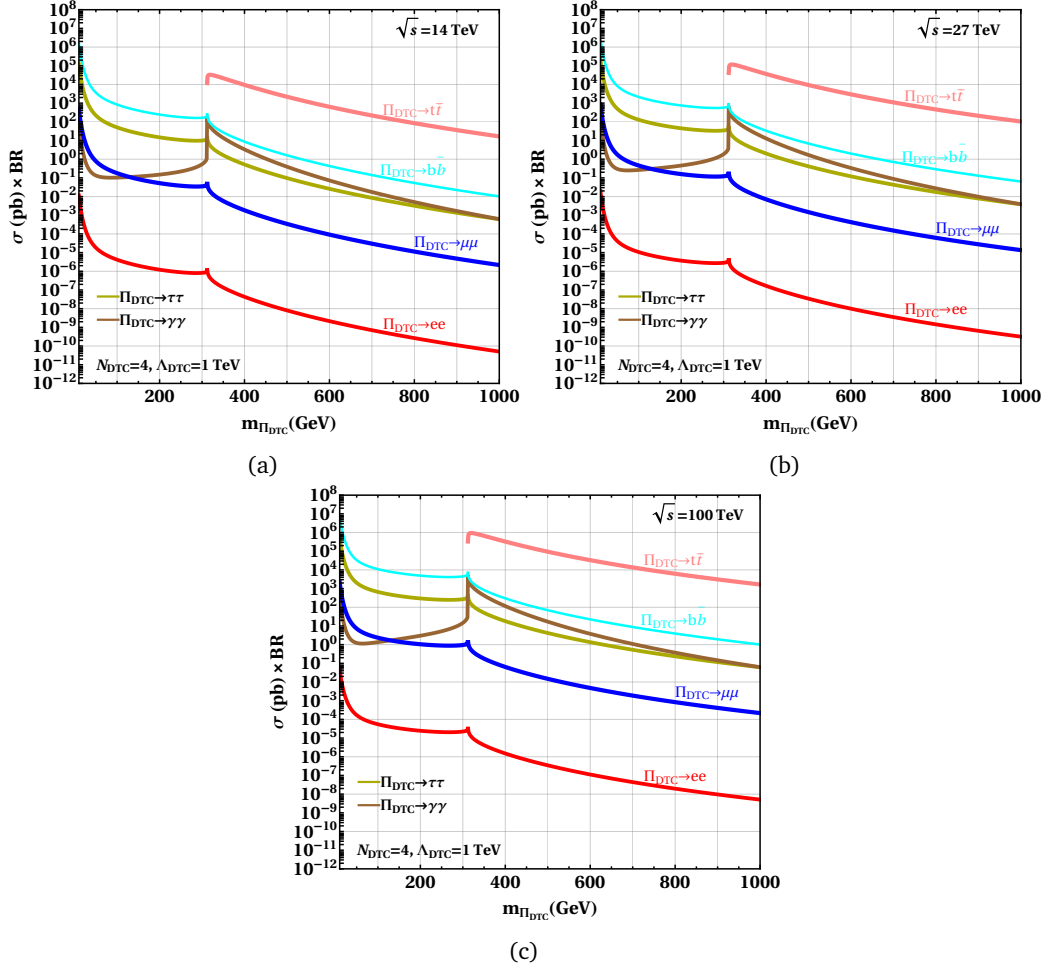


Figure 10: $\sigma \times \text{BR}$ of the various possible decay modes of the Π_{DTC} into photons, quark pairs and lepton pairs for $N_{\text{DTC}} = 4, \Lambda_{\text{DTC}} = 1 \text{ TeV}$ at the (10a) 14 TeV HL-LHC, (10b) 27 TeV HE-LHC, and (10c) a 100 TeV collider.

For $\Lambda < \Lambda_{\text{DTC}}$, we present collider signatures for the scenario N_6 corresponding to minimum number of colours, and given by,

$$N_{\text{TC}} = 8, N_{\text{DTC}} = 4, N_{\text{D}} = 9, \Lambda_{\text{TC}} = 422 \text{ GeV}, \Lambda_{\text{DTC}} = 1 \text{ TeV}, \Lambda = 500 \text{ GeV}. \quad (156)$$

We show the production cross-sections of DTC-pion for various channels in figure 10 at the HL-LHC, HE-LHC, and a 100 TeV future collider. The production cross-sections of DQCD-pion in various modes are shown in figure 11. Our benchmark predictions for the signatures of the DTC- and DQCD-pions in this scenario are given in tables 49-54 at the HL-LHC, HE-LHC, and a 100 TeV future collider. The same results for DTC-eta and DQCD-eta are given in tables 55-57. Predictions of signatures of the DTC-Higgs are given in table 58.

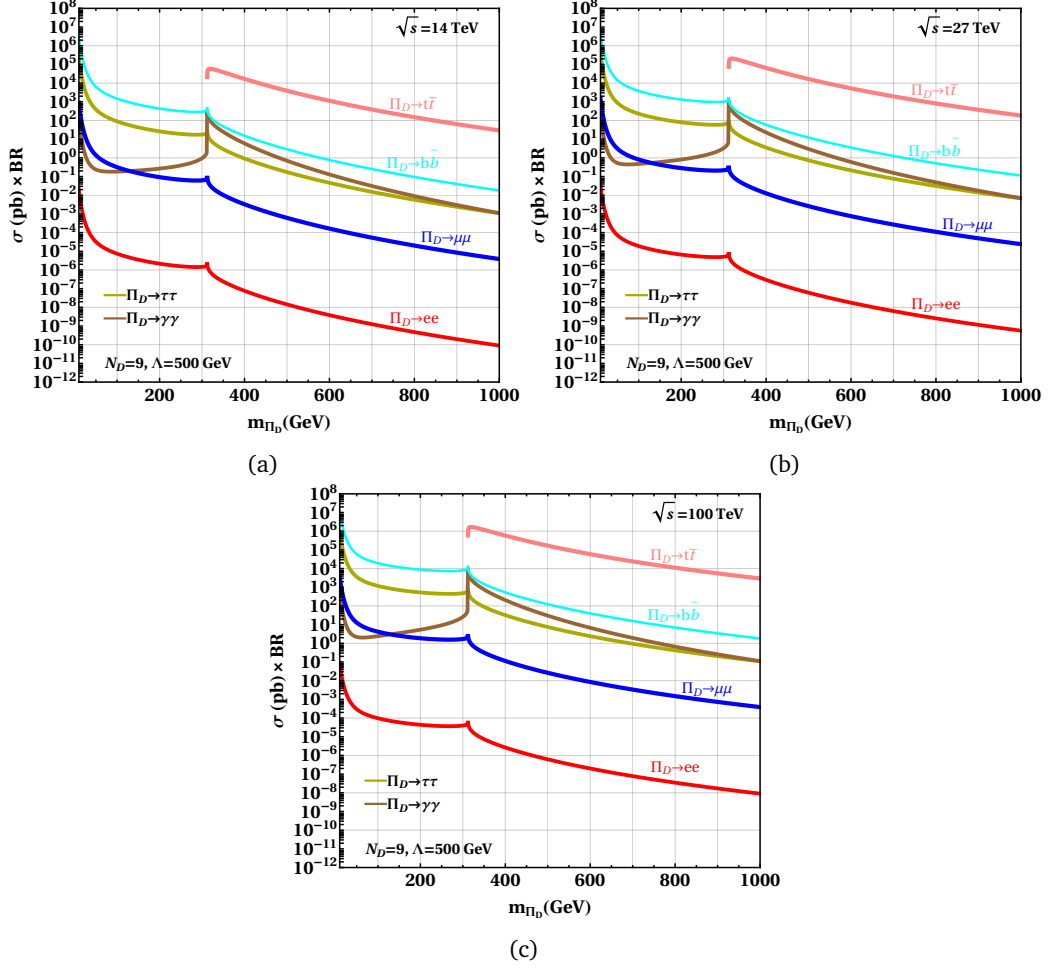


Figure 11: $\sigma \times \text{BR}$ of the various possible decay modes of the Π_D into photons, quark pairs and lepton pairs for $N_D = 9, \Lambda = 500$ GeV at the (11a) 14 TeV HL-LHC, (11b) 27 TeV HE-LHC, and (11c) a 100 TeV collider.

$m_{\Pi_{\text{DTC},D}}$ [GeV]	$N_{\text{DTC}} = 4, \Lambda_{\text{DTC}} = 1$ TeV		$N_D = 9, \Lambda = 500$ GeV	
	500	1000	500	1000
$\tau\tau$ [pb]	$9.7 \cdot 10^{-2}$	$6.1 \cdot 10^{-4}$	0.2	$1.0 \cdot 10^{-3}$
$\mu\mu$ [pb]	$3.4 \cdot 10^{-4}$	$2.2 \cdot 10^{-6}$	$6.1 \cdot 10^{-4}$	$3.8 \cdot 10^{-6}$
ee [pb]	$8.1 \cdot 10^{-9}$	$5.1 \cdot 10^{-11}$	$1.4 \cdot 10^{-8}$	$9.0 \cdot 10^{-11}$
$\gamma\gamma$ [pb]	0.4	$6.2 \cdot 10^{-4}$	0.7	$1.1 \cdot 10^{-3}$
$b\bar{b}$ [pb]	1.6	$1.0 \cdot 10^{-2}$	2.9	$1.8 \cdot 10^{-2}$
$t\bar{t}$ [pb]	2194	17	3901	29

Table 49: Benchmark points for $\Pi_{\text{DTC},D}$ production channels for high mass $m_{\Pi_{\text{DTC},D}}$ at the 14 TeV HL-LHC for $N_{\text{DTC}} = 4, \Lambda_{\text{DTC}} = 1$ TeV and $N_D = 9, \Lambda = 500$ GeV.

$m_{\Pi_{\text{DTC},\text{D}}} [\text{GeV}]$	$N_{\text{DTC}} = 4, \Lambda_{\text{DTC}} = 1 \text{ TeV}$		$N_{\text{D}} = 9, \Lambda = 500 \text{ GeV}$	
	20	60	20	60
$\tau\tau$ [pb]	5465	142	9716	252
$\gamma\gamma$ [pb]	2.1	0.1	3.8	0.2

Table 50: Benchmark points for inclusive $\Pi_{\text{DTC},\text{D}}$ production channel at the 14 TeV HL-LHC for low mass $m_{\Pi_{\text{DTC},\text{D}}}$ for $N_{\text{DTC}} = 4, \Lambda_{\text{DTC}} = 1 \text{ TeV}$ and $N_{\text{D}} = 9, \Lambda = 500 \text{ GeV}$.

$m_{\Pi_{\text{DTC},\text{D}}} [\text{GeV}]$	$N_{\text{DTC}} = 4, \Lambda_{\text{DTC}} = 1 \text{ TeV}$		$N_{\text{D}} = 9, \Lambda = 500 \text{ GeV}$	
	500	1000	500	1000
$\tau\tau$ [pb]	0.4	$3.8 \cdot 10^{-3}$	0.7	$6.8 \cdot 10^{-3}$
$\mu\mu$ [pb]	$1.4 \cdot 10^{-3}$	$1.4 \cdot 10^{-5}$	$2.6 \cdot 10^{-3}$	$2.4 \cdot 10^{-5}$
ee [pb]	$3.4 \cdot 10^{-8}$	$3.2 \cdot 10^{-10}$	$6.1 \cdot 10^{-8}$	$5.6 \cdot 10^{-10}$
$\gamma\gamma$ [pb]	1.7	$3.9 \cdot 10^{-3}$	3.0	$7.0 \cdot 10^{-3}$
$b\bar{b}$ [pb]	6.9	$6.4 \cdot 10^{-2}$	12	0.1
$t\bar{t}$ [pb]	9316	104	16561	185

Table 51: Benchmark points for $\Pi_{\text{DTC},\text{D}}$ production channels for high mass $m_{\Pi_{\text{DTC},\text{D}}}$ at the 27 TeV HE-LHC for $N_{\text{DTC}} = 4, \Lambda_{\text{DTC}} = 1 \text{ TeV}$ and $N_{\text{D}} = 9, \Lambda = 500 \text{ GeV}$.

$m_{\Pi_{\text{DTC},\text{D}}} [\text{GeV}]$	$N_{\text{DTC}} = 4, \Lambda_{\text{DTC}} = 1 \text{ TeV}$		$N_{\text{D}} = 9, \Lambda = 500 \text{ GeV}$	
	20	60	20	60
$\tau\tau$ [pb]	10423	327	18530	581
$\gamma\gamma$ [pb]	4.1	0.3	7.3	0.5

Table 52: Benchmark points for inclusive $\Pi_{\text{DTC},\text{D}}$ production channel at the 27 TeV HE-LHC for low mass $m_{\Pi_{\text{DTC},\text{D}}}$ for $N_{\text{DTC}} = 4, \Lambda_{\text{DTC}} = 1 \text{ TeV}$ and $N_{\text{D}} = 9, \Lambda = 500 \text{ GeV}$.

$m_{\Pi_{\text{DTC},\text{D}}} [\text{GeV}]$	$N_{\text{DTC}} = 4, \Lambda_{\text{DTC}} = 1 \text{ TeV}$		$N_{\text{D}} = 9, \Lambda = 500 \text{ GeV}$	
	500	1000	500	1000
$\tau\tau$ [pb]	4.2	$6.1 \cdot 10^{-2}$	7.4	0.1
$\mu\mu$ [pb]	$1.5 \cdot 10^{-2}$	$2.2 \cdot 10^{-4}$	$2.6 \cdot 10^{-2}$	$3.9 \cdot 10^{-4}$
ee [pb]	$3.4 \cdot 10^{-7}$	$5.1 \cdot 10^{-9}$	$6.2 \cdot 10^{-7}$	$9.0 \cdot 10^{-9}$
$\gamma\gamma$ [pb]	17	$6.2 \cdot 10^{-2}$	30	0.1
$b\bar{b}$ [pb]	70	1.0	123	1.8
$t\bar{t}$ [pb]	94282	1660	$1.7 \cdot 10^5$	2952

Table 53: Benchmark points for $\Pi_{\text{DTC},\text{D}}$ production channels for high mass $m_{\Pi_{\text{DTC},\text{D}}}$ at a 100 TeV collider for $N_{\text{DTC}} = 4, \Lambda_{\text{DTC}} = 1 \text{ TeV}$ and $N_{\text{D}} = 9, \Lambda = 500 \text{ GeV}$.

$m_{\Pi_{\text{DTC},\text{D}}} [\text{GeV}]$	$N_{\text{DTC}} = 4, \Lambda_{\text{DTC}} = 1 \text{ TeV}$		$N_{\text{D}} = 9, \Lambda = 500 \text{ GeV}$	
	20	60	20	60
$\tau\tau$ [pb]	33191	1429	59007	2541
$\gamma\gamma$ [pb]	13	1.1	23	2.0

Table 54: Benchmark points for inclusive $\Pi_{\text{DTC},\text{D}}$ production channel at a 100 TeV collider for low mass $m_{\Pi_{\text{DTC},\text{D}}}$ for $N_{\text{DTC}} = 4, \Lambda_{\text{DTC}} = 1 \text{ TeV}$ and $N_{\text{D}} = 9, \Lambda = 500 \text{ GeV}$.

$m_{\eta_{\text{TC},\text{DTC},\text{D}}} [\text{GeV}]$	$N_{\text{TC}} = 8, \Lambda_{\text{TC}} = 422 \text{ GeV}$	$N_{\text{DTC}} = 4, \Lambda_{\text{DTC}} = 1 \text{ TeV}$	$N_{\text{D}} = 9, \Lambda = 500 \text{ GeV}$
	962	3225	1075
$\tau\tau$ [pb]	$2.2 \cdot 10^{-3}$	$2.3 \cdot 10^{-8}$	$6.3 \cdot 10^{-4}$
$\mu\mu$ [pb]	$8.1 \cdot 10^{-6}$	$8.2 \cdot 10^{-11}$	$2.2 \cdot 10^{-6}$
ee [pb]	$1.9 \cdot 10^{-10}$	$1.9 \cdot 10^{-15}$	$5.2 \cdot 10^{-11}$
$\gamma\gamma$ [pb]	$2.5 \cdot 10^{-3}$	$2.6 \cdot 10^{-9}$	$5.5 \cdot 10^{-4}$
$b\bar{b}$ [pb]	$3.8 \cdot 10^{-2}$	$3.8 \cdot 10^{-7}$	$1.0 \cdot 10^{-2}$
$t\bar{t}$ [pb]	62	$6.6 \cdot 10^{-4}$	17

Table 55: Benchmark points for $\eta_{\text{TC},\text{DTC},\text{D}}$ production channels at the 14 TeV HL-LHC for $N_{\text{TC}} = 8, \Lambda_{\text{TC}} = 422 \text{ GeV}$, $N_{\text{DTC}} = 4, \Lambda_{\text{DTC}} = 1 \text{ TeV}$ and $N_{\text{D}} = 9, \Lambda = 500 \text{ GeV}$.

$m_{\eta_{\text{TC},\text{DTC},\text{D}}} [\text{GeV}]$	$N_{\text{TC}} = 8, \Lambda_{\text{TC}} = 422 \text{ GeV}$	$N_{\text{DTC}} = 4, \Lambda_{\text{DTC}} = 1 \text{ TeV}$	$N_{\text{D}} = 9, \Lambda = 500 \text{ GeV}$
	962	3225	1075
$\tau\tau$ [pb]	$1.4 \cdot 10^{-2}$	$6.4 \cdot 10^{-7}$	$4.1 \cdot 10^{-3}$
$\mu\mu$ [pb]	$4.9 \cdot 10^{-5}$	$2.2 \cdot 10^{-9}$	$1.5 \cdot 10^{-5}$
ee [pb]	$1.2 \cdot 10^{-9}$	$5.3 \cdot 10^{-14}$	$3.4 \cdot 10^{-10}$
$\gamma\gamma$ [pb]	$1.5 \cdot 10^{-2}$	$7.2 \cdot 10^{-8}$	$3.7 \cdot 10^{-3}$
$b\bar{b}$ [pb]	0.2	$1.1 \cdot 10^{-5}$	$6.9 \cdot 10^{-2}$
$t\bar{t}$ [pb]	378	$1.8 \cdot 10^{-2}$	113

Table 56: Benchmark points for $\eta_{\text{TC},\text{DTC},\text{D}}$ production channels at the 27 TeV HE-LHC for $N_{\text{TC}} = 8, \Lambda_{\text{TC}} = 422 \text{ GeV}$, $N_{\text{DTC}} = 4, \Lambda_{\text{DTC}} = 1 \text{ TeV}$ and $N_{\text{D}} = 9, \Lambda = 500 \text{ GeV}$.

$m_{\eta_{TC,DTC,D}}$ [GeV]	$N_{TC} = 8, \Lambda_{TC} = 422$ GeV 962	$N_{DTC} = 4, \Lambda_{DTC} = 1$ TeV 3225	$N_D = 9, \Lambda = 500$ GeV 1075
$\tau\tau$ [pb]	0.2	$3.9 \cdot 10^{-5}$	$7.0 \cdot 10^{-2}$
$\mu\mu$ [pb]	$7.7 \cdot 10^{-4}$	$1.4 \cdot 10^{-7}$	$2.5 \cdot 10^{-4}$
ee [pb]	$1.8 \cdot 10^{-8}$	$3.3 \cdot 10^{-12}$	$5.8 \cdot 10^{-9}$
$\gamma\gamma$ [pb]	0.2	$4.4 \cdot 10^{-6}$	$6.2 \cdot 10^{-2}$
$b\bar{b}$ [pb]	3.6	$6.6 \cdot 10^{-4}$	1.2
$t\bar{t}$ [pb]	5861	1.1	1916

Table 57: Benchmark points for $\eta_{TC,DTC,D}$ production channels at a 100 TeV collider for $N_{TC} = 8, \Lambda_{TC} = 422$ GeV, $N_{DTC} = 4, \Lambda_{DTC} = 1$ TeV and $N_D = 9, \Lambda = 500$ GeV.

$\Delta\chi_{DTC}$ $m_{H_{DTC}}$ [GeV]	HL-LHC [14 TeV, 3 ab ⁻¹]		HE-LHC [27 TeV, 15 ab ⁻¹]		100 TeV, 30 ab ⁻¹	
	+2	-2	+2	-2	+2	-2
$\tau\tau$ [pb]	$4.1 \cdot 10^{-7}$	$1.4 \cdot 10^{-5}$	$6.5 \cdot 10^{-6}$	$1.3 \cdot 10^{-4}$	$2.6 \cdot 10^{-4}$	$3.2 \cdot 10^{-3}$
$\mu\mu$ [pb]	$1.4 \cdot 10^{-9}$	$4.9 \cdot 10^{-8}$	$2.3 \cdot 10^{-8}$	$4.6 \cdot 10^{-7}$	$9.2 \cdot 10^{-7}$	$1.1 \cdot 10^{-5}$
ee [pb]	$3.4 \cdot 10^{-14}$	$1.1 \cdot 10^{-12}$	$5.4 \cdot 10^{-13}$	$1.1 \cdot 10^{-11}$	$2.2 \cdot 10^{-11}$	$2.7 \cdot 10^{-10}$
$\gamma\gamma$ [pb]	$7.9 \cdot 10^{-8}$	$5.4 \cdot 10^{-6}$	$1.3 \cdot 10^{-6}$	$5.2 \cdot 10^{-5}$	$5.0 \cdot 10^{-5}$	$1.3 \cdot 10^{-3}$
$b\bar{b}$ [pb]	$6.8 \cdot 10^{-6}$	$2.3 \cdot 10^{-4}$	$1.1 \cdot 10^{-4}$	$2.2 \cdot 10^{-3}$	$4.3 \cdot 10^{-3}$	$5.4 \cdot 10^{-2}$
$t\bar{t}$ [pb]	$1.1 \cdot 10^{-2}$	0.3	0.2	3.5	7.2	87

Table 58: Benchmark points for H_{DTC} production channels at the 14 TeV HL-LHC, 27 TeV HE-LHC and the 100 TeV collider for $N_{DTC} = 4, \Lambda_{DTC} = 1$ TeV for the scenario N_6 .

8.4 Signatures of the DTC-paradigm when the FN mechanism is implemented within its framework

In this section, we discuss the signatures of the DTC paradigm when the FN mechanism is accommodated within it.

8.4.1 $\Lambda \approx \Lambda_{DTC}$

From the fit results, it can be observed that for the case $\Lambda \approx \Lambda_{DTC}, N_{DTC}, N_D$ in the FN mechanism coincides with N_D, N_{DTC} respectively in the SHVM mechanism for the scenario represented by N_6 . Consequently, signatures in this case for DTC-pion, DQCD-pion, DTC and DQCD-etats are identical to the case $\Lambda \approx \Lambda_{DTC}$ corresponding to the SHVM, and are presented in section 8.3.1. We may have different signatures of the DTC and DQCD in this case with respect to the scenario denoted by N_2 , and when the flavon field is a composite state of more than two fermions.

For the technicolour sector, since the mass of TC-eta $m_{\eta_{TC}}$ is 17.4 TeV, no collider signatures are expected at the 14 TeV HL-LHC. Therefore, we present the collider signatures of the TC-eta for the 27 TeV HE-LHC and 100 TeV colliders in table 59.

	HE-LHC [27 TeV, 15 ab ⁻¹]	100 TeV, 30 ab ⁻¹
$\tau\tau$ [pb]	$2.8 \cdot 10^{-18}$	$3.8 \cdot 10^{-12}$
$\mu\mu$ [pb]	$9.9 \cdot 10^{-21}$	$1.4 \cdot 10^{-14}$
ee [pb]	$2.3 \cdot 10^{-25}$	$3.2 \cdot 10^{-19}$
$\gamma\gamma$ [pb]	$3.5 \cdot 10^{-20}$	$4.7 \cdot 10^{-14}$
$b\bar{b}$ [pb]	$4.6 \cdot 10^{-17}$	$6.4 \cdot 10^{-11}$
$t\bar{t}$ [pb]	$8.0 \cdot 10^{-14}$	$1.1 \cdot 10^{-7}$

Table 59: Benchmark points for η_{TC} production channels with mass $m_{\eta_{\text{TC}}} = 17.4$ TeV at the 27 TeV HE-LHC and 100 TeV collider for $N_{\text{TC}} = 4, \Lambda_{\text{TC}} = 5.4$ TeV .

We show the sensitivities of the signatures of the DTC-Higgs and DQCD-Higgs in different modes in tables 60-61 for the HL-LHC, HE-LHC, and a future 100 TeV collider.

$\Delta\chi_{DTC}$ $m_{H_{DTC}}$ [GeV]	HL-LHC [14 TeV, 3 ab ⁻¹]		HE-LHC [27 TeV, 15 ab ⁻¹]		100 TeV, 30 ab ⁻¹	
	+2	-2	+2	-2	+2	-2
$\tau\tau$ [pb]	$7.4 \cdot 10^{-4}$	$3.3 \cdot 10^{-3}$	$1.9 \cdot 10^{-2}$	$2.1 \cdot 10^{-2}$	0.3	0.3
$\mu\mu$ [pb]	$1.0 \cdot 10^{-5}$	$1.1 \cdot 10^{-5}$	$6.6 \cdot 10^{-5}$	$7.4 \cdot 10^{-5}$	$1.1 \cdot 10^{-3}$	$1.2 \cdot 10^{-3}$
ee [pb]	$2.5 \cdot 10^{-10}$	$2.8 \cdot 10^{-10}$	$1.5 \cdot 10^{-9}$	$1.7 \cdot 10^{-9}$	$2.5 \cdot 10^{-8}$	$2.7 \cdot 10^{-8}$
$\gamma\gamma$ [pb]	$2.6 \cdot 10^{-3}$	$3.1 \cdot 10^{-3}$	$1.7 \cdot 10^{-2}$	$1.9 \cdot 10^{-2}$	0.3	0.3
$b\bar{b}$ [pb]	$4.9 \cdot 10^{-2}$	$5.5 \cdot 10^{-2}$	0.3	0.3	5.5	5.5
$t\bar{t}$ [pb]	74	83	466	516	7493	8197

Table 60: Benchmark points for H_{DTC} production channels at the 14 TeV HL-LHC, 27 TeV HE-LHC and a 100 TeV collider for $N_{DTC} = 3, \Lambda_{DTC} = 500$ GeV .

$\Delta\chi_D$ m_{H_D} [GeV]	HL-LHC [14 TeV, 3 ab ⁻¹]		HE-LHC [27 TeV, 15 ab ⁻¹]		100 TeV, 30 ab ⁻¹	
	+2	-2	+2	-2	+2	-2
$\tau\tau$ [pb]	$1.3 \cdot 10^{-12}$	105	$1.7 \cdot 10^{-9}$	290	$9.7 \cdot 10^{-7}$	1648
$\mu\mu$ [pb]	$4.5 \cdot 10^{-15}$	0.4	$6.0 \cdot 10^{-12}$	1.0	$3.4 \cdot 10^{-9}$	5.8
ee [pb]	$1.0 \cdot 10^{-19}$	$8.7 \cdot 10^{-6}$	$1.4 \cdot 10^{-16}$	$2.2 \cdot 10^{-6}$	$8.0 \cdot 10^{-14}$	$1.4 \cdot 10^{-4}$
$\gamma\gamma$ [pb]	$3.2 \cdot 10^{-14}$	0.2	$4.3 \cdot 10^{-11}$	0.5	$2.5 \cdot 10^{-8}$	2.8
$b\bar{b}$ [pb]	$2.1 \cdot 10^{-11}$	1744	$2.8 \cdot 10^{-8}$	4805	$1.6 \cdot 10^{-5}$	27325
$t\bar{t}$ [pb]	$3.6 \cdot 10^{-8}$	0	$4.8 \cdot 10^{-5}$	0	$2.7 \cdot 10^{-2}$	0

Table 61: Benchmark points for H_D production channels at the 14 TeV HL-LHC, 27 TeV HE-LHC and the 100 TeV collider for $N_D = 2, \Lambda = 500$ GeV .

8.4.2 $\Lambda > \Lambda_{\text{DTC}}$

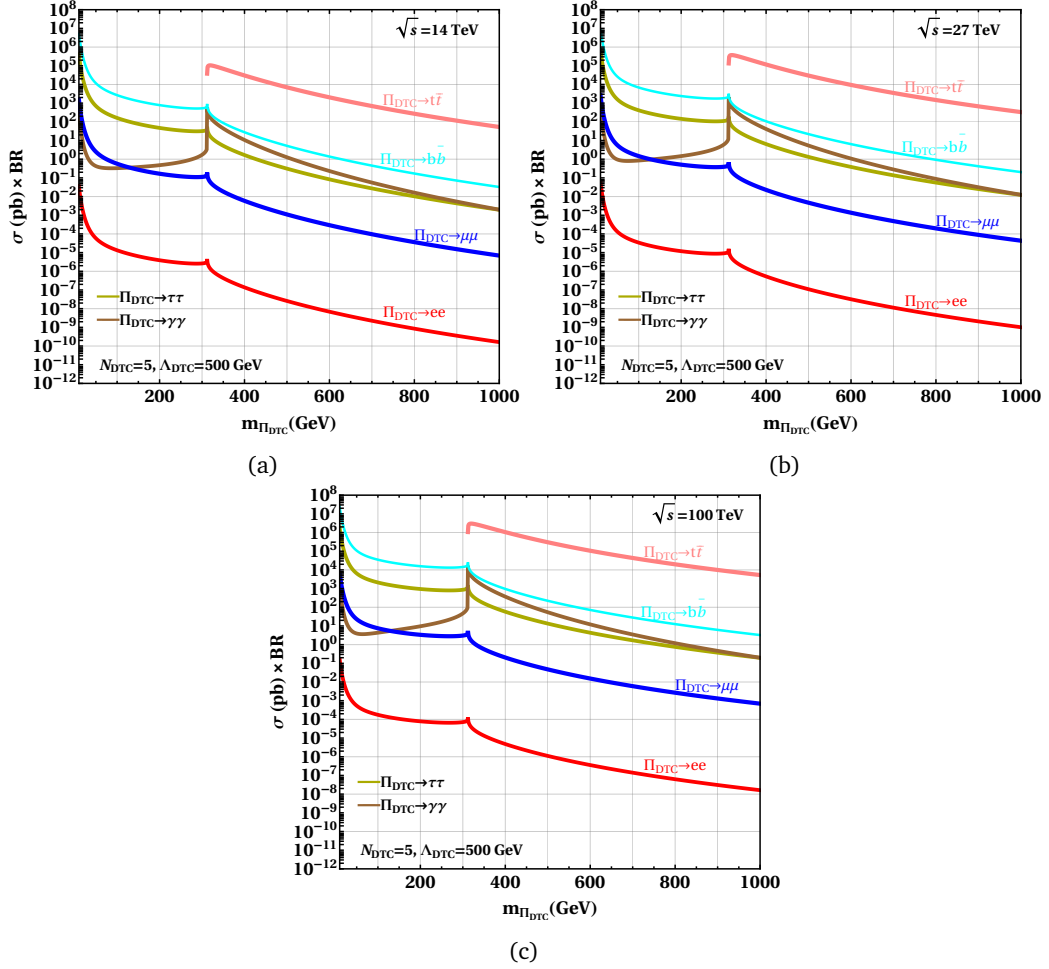


Figure 12: $\sigma \times \text{BR}$ of the various possible decay modes of the Π_{DTC} into photons, quark pairs and lepton pairs for $N_{\text{DTC}} = 5, \Lambda_{\text{DTC}} = 500 \text{ GeV}$ at the (12a) 14 TeV HL-LHC, (12b) 27 TeV HE-LHC, and (12c) a 100 TeV collider.

For the scenario $\Lambda > \Lambda_{\text{DTC}}$, we use the following numerical results from fits,

$$N_{\text{TC}} = 3, N_{\text{DTC}} = 5, N_{\text{D}} = 2, \Lambda_{\text{TC}} = 5.9 \text{ TeV}, \Lambda_{\text{DTC}} = 500 \text{ GeV}, \Lambda = 1 \text{ TeV}. \quad (157)$$

We show the production cross-sections of DTC and DQCD-pions in different modes in figures 12-13 at the HL-LHC, HE-LHC, and a 100 TeV future collider. The benchmark predictions of the signatures of heavy and low DTC and DQCD-pion masses, in this case, are given in tables 62-67 for the HL-LHC, HE-LHC, and a 100 TeV future collider.

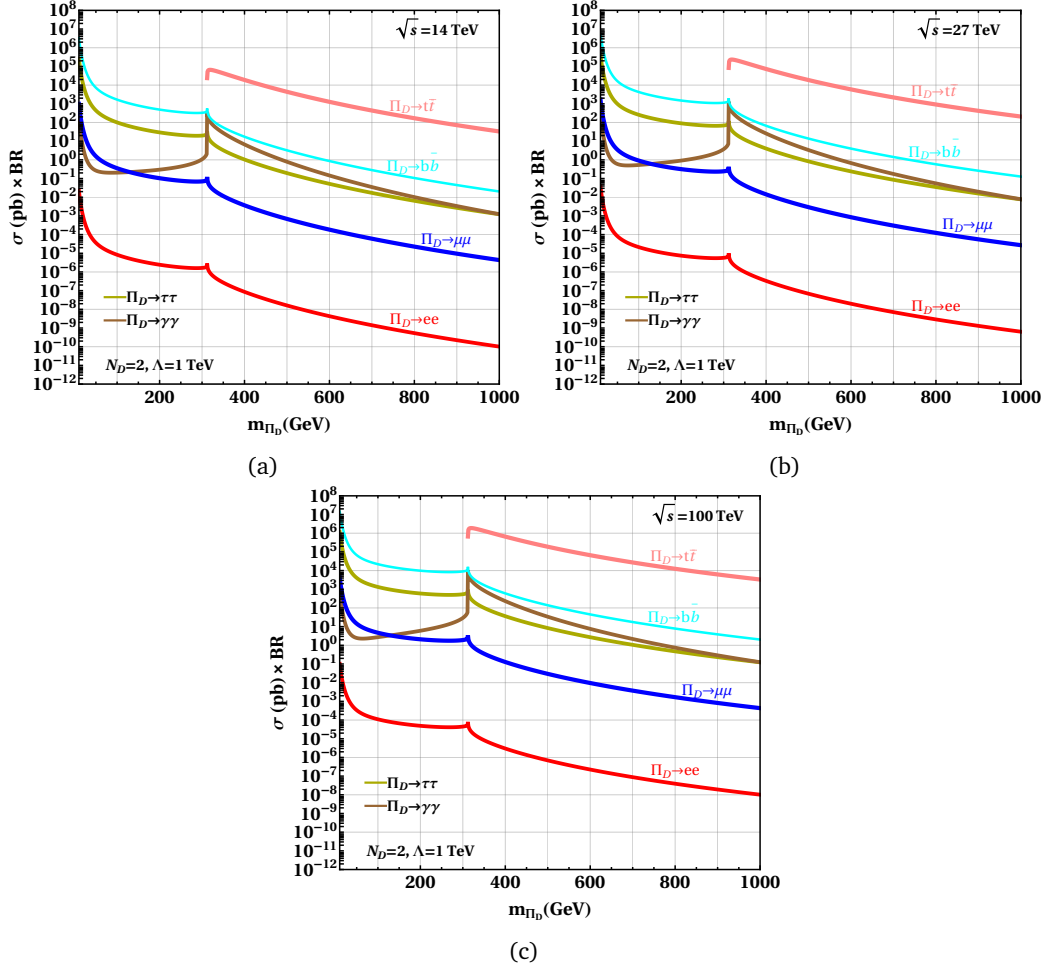


Figure 13: $\sigma \times \text{BR}$ of the various possible decay modes of the Π_D into photons, quark pairs, and lepton pairs for $N_D = 2, \Lambda = 1 \text{ TeV}$ at the (13a) 14 TeV HL-LHC, (13b) 27 TeV HE-LHC, and (13c) a 100 TeV collider.

$m_{\Pi_{\text{DTC},D}} [\text{GeV}]$	$N_{\text{DTC}} = 5, \Lambda_{\text{DTC}} = 500 \text{ GeV}$		$N_D = 2, \Lambda = 1 \text{ TeV}$	
	500	1000	500	1000
$\tau\tau$ [pb]	0.3	$2.0 \cdot 10^{-3}$	0.2	$1.2 \cdot 10^{-3}$
$\mu\mu$ [pb]	$1.1 \cdot 10^{-3}$	$6.9 \cdot 10^{-6}$	$6.9 \cdot 10^{-4}$	$4.3 \cdot 10^{-6}$
ee [pb]	$2.6 \cdot 10^{-8}$	$1.6 \cdot 10^{-10}$	$1.6 \cdot 10^{-8}$	$1.0 \cdot 10^{-10}$
$\gamma\gamma$ [pb]	1.3	$2.0 \cdot 10^{-3}$	0.8	$1.2 \cdot 10^{-3}$
$b\bar{b}$ [pb]	5.2	$3.3 \cdot 10^{-2}$	3.2	$2.0 \cdot 10^{-2}$
$t\bar{t}$ [pb]	7022	53	4389	330

Table 62: Benchmark points for $\Pi_{\text{DTC},D}$ production channels for high mass $m_{\Pi_{\text{DTC},D}}$ at the 14 TeV HL-LHC for $N_{\text{DTC}} = 5, \Lambda_{\text{DTC}} = 500 \text{ GeV}$ and $N_D = 2, \Lambda = 1 \text{ TeV}$.

$m_{\Pi_{\text{DTC},D}}$ [GeV]	$N_{\text{DTC}} = 5, \Lambda_{\text{DTC}} = 500$ GeV		$N_D = 2, \Lambda = 1$ TeV	
	20	60	20	60
$\tau\tau$ [pb]	17489	453	10930	283
$\gamma\gamma$ [pb]	6.9	0.4	4.3	0.2

Table 63: Benchmark points for inclusive $\Pi_{\text{DTC},D}$ production channel at the 14 TeV HL-LHC for low mass $m_{\Pi_{\text{DTC},D}}$ for $N_{\text{DTC}} = 5, \Lambda_{\text{DTC}} = 500$ GeV and $N_D = 2, \Lambda = 1$ TeV.

$m_{\Pi_{\text{DTC},D}}$ [GeV]	$N_{\text{DTC}} = 5, \Lambda_{\text{DTC}} = 500$ GeV		$N_D = 2, \Lambda = 1$ TeV	
	500	1000	500	1000
$\tau\tau$ [pb]	1.3	$1.2 \cdot 10^{-2}$	0.8	$7.7 \cdot 10^{-3}$
$\mu\mu$ [pb]	$4.7 \cdot 10^{-3}$	$4.3 \cdot 10^{-5}$	$2.9 \cdot 10^{-3}$	$2.7 \cdot 10^{-5}$
ee [pb]	$1.1 \cdot 10^{-7}$	$1.0 \cdot 10^{-9}$	$6.8 \cdot 10^{-8}$	$6.4 \cdot 10^{-10}$
$\gamma\gamma$ [pb]	5.5	$1.3 \cdot 10^{-2}$	3.3	$7.8 \cdot 10^{-3}$
$b\bar{b}$ [pb]	22	0.2	13.7	0.1
$t\bar{t}$ [pb]	2981	332	18632	208

Table 64: Benchmark points for $\Pi_{\text{DTC},D}$ production channels for high mass $m_{\Pi_{\text{DTC},D}}$ at the 27 TeV HE-LHC for $N_{\text{DTC}} = 5, \Lambda_{\text{DTC}} = 500$ GeV and $N_D = 2, \Lambda = 1$ TeV.

$m_{\Pi_{\text{DTC},D}}$ [GeV]	$N_{\text{DTC}} = 5, \Lambda_{\text{DTC}} = 500$ GeV		$N_D = 2, \Lambda = 1$ TeV	
	20	60	20	60
$\tau\tau$ [pb]	33355	1047	20847	654
$\gamma\gamma$ [pb]	13	0.8	8.2	0.5

Table 65: Benchmark points for inclusive $\Pi_{\text{DTC},D}$ production channel at the 27 TeV HE-LHC for low mass $m_{\Pi_{\text{DTC},D}}$ for $N_{\text{DTC}} = 5, \Lambda_{\text{DTC}} = 500$ GeV and $N_D = 2, \Lambda = 1$ TeV.

$m_{\Pi_{\text{DTC},D}}$ [GeV]	$N_{\text{DTC}} = 5, \Lambda_{\text{DTC}} = 500$ GeV		$N_D = 2, \Lambda = 1$ TeV	
	500	1000	500	1000
$\tau\tau$ [pb]	13.4	0.2	8.4	0.1
$\mu\mu$ [pb]	$4.7 \cdot 10^{-2}$	$6.9 \cdot 10^{-4}$	$3.0 \cdot 10^{-2}$	$4.3 \cdot 10^{-4}$
ee [pb]	$1.1 \cdot 10^{-6}$	$1.6 \cdot 10^{-8}$	$6.9 \cdot 10^{-7}$	$1.0 \cdot 10^{-8}$
$\gamma\gamma$ [pb]	54	0.2	34	0.1
$b\bar{b}$ [pb]	222	3.3	140	2.0
$t\bar{t}$ [pb]	$3.0 \cdot 10^5$	5313	$1.9 \cdot 10^5$	3320

Table 66: Benchmark points for $\Pi_{\text{DTC},D}$ production channels for high mass $m_{\Pi_{\text{DTC},D}}$ at a 100 TeV collider for $N_{\text{DTC}} = 5, \Lambda_{\text{DTC}} = 500$ GeV and $N_D = 2, \Lambda = 1$ TeV.

$m_{\Pi_{\text{DTC},\text{D}}} [\text{GeV}]$	$N_{\text{DTC}} = 5, \Lambda_{\text{DTC}} = 500 \text{ GeV}$		$N_{\text{D}} = 2, \Lambda = 1 \text{ TeV}$	
	20	60	20	60
$\tau\tau$ [pb]	$1.1 \cdot 10^5$	4573	$6.6 \cdot 10^5$	2852
$\gamma\gamma$ [pb]	42	3.7	26	2.3

Table 67: Benchmark points for inclusive $\Pi_{\text{DTC},\text{D}}$ production channel at a 100 TeV collider for low mass $m_{\Pi_{\text{DTC},\text{D}}}$ for $N_{\text{DTC}} = 5, \Lambda_{\text{DTC}} = 500 \text{ GeV}$ and $N_{\text{D}} = 2, \Lambda = 1 \text{ TeV}$.

We show the benchmark values of the signatures of TC, DTC and DQCD-eta at the HL-LHC, HE-LHC, and a future 100 TeV collider in tables 68-70. The mass of the TC-eta is $m_{\eta_{\text{TC}}} = 21.9 \text{ TeV}$. Therefore, it is out of the reach of the HL-LHC.

$m_{\eta_{\text{DTC},\text{D}}} [\text{GeV}]$	$N_{\text{DTC}} = 5, \Lambda_{\text{DTC}} = 500 \text{ GeV}$	$N_{\text{D}} = 2, \Lambda = 1 \text{ TeV}$
	1442	4561
$\tau\tau$ [pb]	$1.1 \cdot 10^{-4}$	$8.2 \cdot 10^{-10}$
$\mu\mu$ [pb]	$4.0 \cdot 10^{-7}$	$2.9 \cdot 10^{-12}$
ee [pb]	$9.3 \cdot 10^{-12}$	$6.8 \cdot 10^{-17}$
$\gamma\gamma$ [pb]	5.7 · 10 ⁻⁵	$4.9 \cdot 10^{-11}$
$b\bar{b}$ [pb]	$1.8 \cdot 10^{-3}$	$1.4 \cdot 10^{-8}$
$t\bar{t}$ [pb]	3.1	$2.3 \cdot 10^{-5}$

Table 68: Benchmark points for $\eta_{\text{DTC},\text{D}}$ production channels at the 14 TeV HL-LHC for $N_{\text{DTC}} = 5, \Lambda_{\text{DTC}} = 500 \text{ GeV}$ and $N_{\text{D}} = 2, \Lambda = 1 \text{ TeV}$.

$m_{\eta_{\text{TC},\text{DTC},\text{D}}} [\text{GeV}]$	$N_{\text{TC}} = 3, \Lambda_{\text{TC}} = 5.9 \text{ TeV}$	$N_{\text{DTC}} = 5, \Lambda_{\text{DTC}} = 500 \text{ GeV}$	$N_{\text{D}} = 2, \Lambda = 1 \text{ TeV}$
	21971	1442	4561
$\tau\tau$ [pb]	$2.3 \cdot 10^{-21}$	$9.6 \cdot 10^{-5}$	$6.1 \cdot 10^{-8}$
$\mu\mu$ [pb]	$8.2 \cdot 10^{-24}$	$3.4 \cdot 10^{-6}$	$2.2 \cdot 10^{-10}$
ee [pb]	$1.9 \cdot 10^{-28}$	$7.9 \cdot 10^{-11}$	$5.0 \cdot 10^{-15}$
$\gamma\gamma$ [pb]	$8.6 \cdot 10^{-24}$	4.8 · 10 ⁻⁴	$3.7 \cdot 10^{-9}$
$b\bar{b}$ [pb]	$3.4 \cdot 10^{-20}$	1.6 · 10 ⁻²	$1.0 \cdot 10^{-6}$
$t\bar{t}$ [pb]	$6.6 \cdot 10^{-17}$	27	1.7 · 10 ⁻³

Table 69: Benchmark points for $\eta_{\text{TC},\text{DTC},\text{D}}$ production channels at the 27 TeV HE-LHC for $N_{\text{TC}} = 3, \Lambda_{\text{TC}} = 5.9 \text{ TeV}$, $N_{\text{DTC}} = 5, \Lambda_{\text{DTC}} = 500 \text{ GeV}$ and $N_{\text{D}} = 2, \Lambda = 1 \text{ TeV}$.

$m_{\eta_{TC,DTC,D}}$ [GeV]	$N_{TC} = 3, \Lambda_{TC} = 5.9$ TeV 21971	$N_{DTC} = 5, \Lambda_{DTC} = 500$ GeV 1442	$N_D = 2, \Lambda = 1$ TeV 4561
$\tau\tau$ [pb]	$3.8 \cdot 10^{-13}$	$2.1 \cdot 10^{-2}$	$7.6 \cdot 10^{-4}$
$\mu\mu$ [pb]	$1.3 \cdot 10^{-15}$	$7.4 \cdot 10^{-5}$	$2.7 \cdot 10^{-8}$
ee [pb]	$3.1 \cdot 10^{-20}$	$1.7 \cdot 10^{-9}$	$6.3 \cdot 10^{-13}$
$\gamma\gamma$ [pb]	$1.4 \cdot 10^{-15}$	$1.1 \cdot 10^{-2}$	$4.6 \cdot 10^{-7}$
$b\bar{b}$ [pb]	$6.3 \cdot 10^{-12}$	0.3	$1.3 \cdot 10^{-4}$
$t\bar{t}$ [pb]	$1.1 \cdot 10^{-8}$	583	0.2

Table 70: Benchmark points for $\eta_{TC,DTC,D}$ production channels at a 100 TeV collider for $N_{TC} = 3, \Lambda_{TC} = 5.9$ TeV, $N_{DTC} = 5, \Lambda_{DTC} = 500$ GeV and $N_D = 2, \Lambda = 1$ TeV.

The sensitivities of the signatures of the DTC-Higgs and DQCD-Higgs in different modes are shown in tables 71-72 for the HL-LHC, HE-LHC, and a future 100 TeV collider.

$\Delta\chi_{DTC}$ $m_{H_{DTC}}$ [GeV]	HL-LHC [14 TeV, 3 ab ⁻¹]		HE-LHC [27 TeV, 15 ab ⁻¹]		100 TeV, 30 ab ⁻¹	
	+2	-2	+2	-2	+2	-2
$\tau\tau$ [pb]	$1.1 \cdot 10^{-3}$	$3.6 \cdot 10^{-3}$	$7.3 \cdot 10^{-3}$	$2.1 \cdot 10^{-2}$	0.1	0.3
$\mu\mu$ [pb]	$3.9 \cdot 10^{-6}$	$1.3 \cdot 10^{-5}$	$2.6 \cdot 10^{-5}$	$7.6 \cdot 10^{-5}$	$4.4 \cdot 10^{-4}$	$1.1 \cdot 10^{-3}$
ee [pb]	$9.2 \cdot 10^{-11}$	$3.0 \cdot 10^{-10}$	$6.1 \cdot 10^{-10}$	$1.8 \cdot 10^{-9}$	$1.0 \cdot 10^{-8}$	$2.6 \cdot 10^{-8}$
$\gamma\gamma$ [pb]	$8.9 \cdot 10^{-4}$	$3.8 \cdot 10^{-3}$	$5.9 \cdot 10^{-3}$	$2.2 \cdot 10^{-2}$	0.1	0.3
$b\bar{b}$ [pb]	$1.8 \cdot 10^{-2}$	$6.0 \cdot 10^{-2}$	0.1	0.4	2.1	5.3
$t\bar{t}$ [pb]	28	87	185	515	3140	7700

Table 71: Benchmark points for H_{DTC} production channels at the 14 TeV HL-LHC, 27 TeV HE-LHC and a 100 TeV collider for $N_{DTC} = 5, \Lambda_{DTC} = 500$ GeV .

$\Delta\chi_D$ m_{H_D} [GeV]	HL-LHC [14 TeV, 3 ab ⁻¹]		HE-LHC [27 TeV, 15 ab ⁻¹]		100 TeV, 30 ab ⁻¹	
	+2	-2	+2	-2	+2	-2
$\tau\tau$ [pb]		8.1	$1.0 \cdot 10^{-14}$	27	$9.5 \cdot 10^{10}$	203
$\mu\mu$ [pb]		$2.8 \cdot 10^{-2}$	$3.5 \cdot 10^{-17}$	$9.6 \cdot 10^{-5}$	$3.4 \cdot 10^{-12}$	0.7
ee [pb]		$6.7 \cdot 10^{-7}$	$8.3 \cdot 10^{-10}$	$2.2 \cdot 10^{-6}$	$7.9 \cdot 10^{-17}$	$1.7 \cdot 10^{-5}$
$\gamma\gamma$ [pb]		$7.7 \cdot 10^{-2}$	$7.5 \cdot 10^{-17}$	$2.6 \cdot 10^{-2}$	$7.1 \cdot 10^{-12}$	1.9
$b\bar{b}$ [pb]		135	$1.7 \cdot 10^{-13}$	451	$1.6 \cdot 10^{-8}$	3363
$t\bar{t}$ [pb]		0	$2.8 \cdot 10^{-10}$	0	$2.7 \cdot 10^{-5}$	0

Table 72: Benchmark points for H_D production channels at the 14 TeV HL-LHC, 27 TeV HE-LHC and the 100 TeV collider for $N_D = 2, \Lambda = 1$ TeV .

8.4.3 $\Lambda < \Lambda_{DTC}$

In the scenario $\Lambda < \Lambda_{DTC}$, we use

$$N_{TC} = 2, N_{DTC} = 3, N_D = 2, \Lambda_{TC} = 5.4 \text{ TeV}, \Lambda_{DTC} = 1 \text{ TeV}, \Lambda = 500 \text{ GeV}. \quad (158)$$

We notice that in this scenario, $N_D = 2$, $\Lambda = 500$ GeV is identical to N_{DTC} , Λ_{DTC} for the case $\Lambda \approx \Lambda_{DTC}$ in the SHVM. Therefore, the sensitivities of signatures of the DQCD-pions are the same as in the case $\Lambda \approx \Lambda_{DTC}$ of the SHVM. We show variations of cross-sections of the signatures of the DTC-pions in figure 14.

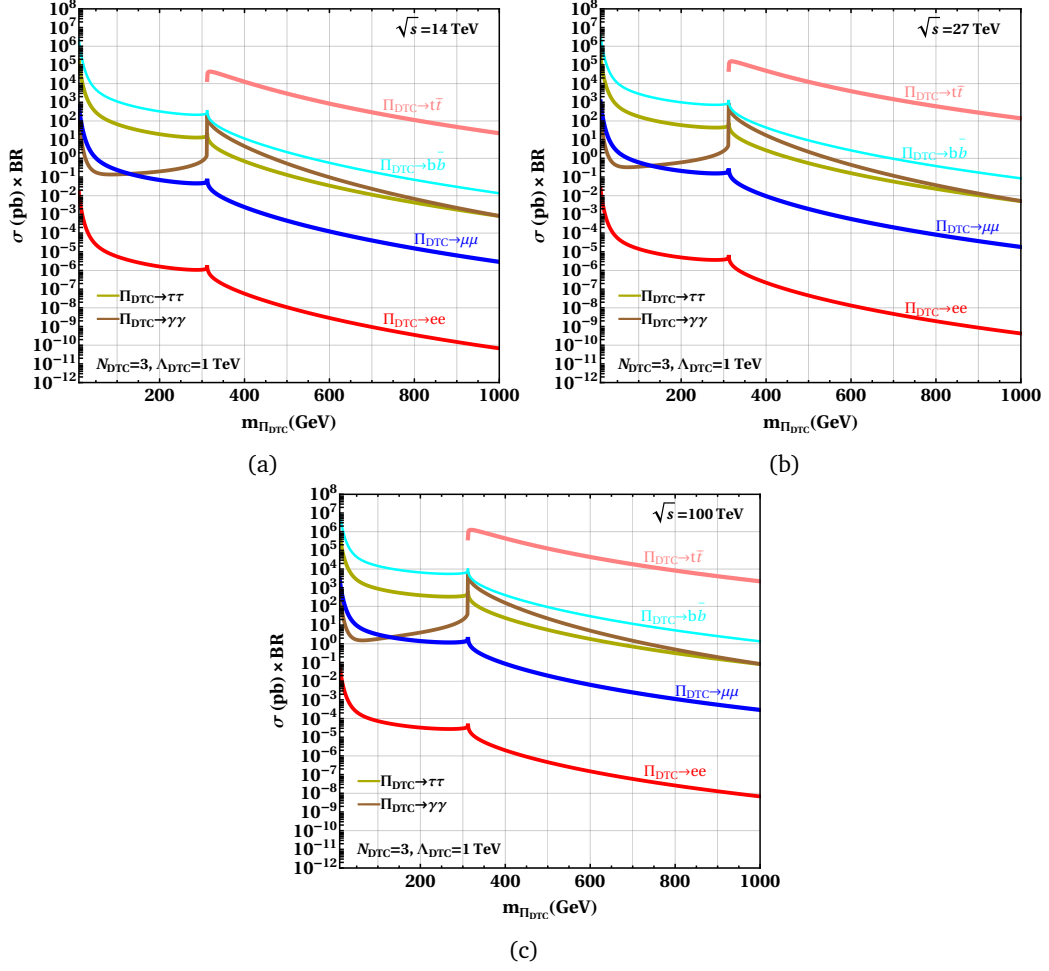


Figure 14: $\sigma \times \text{BR}$ of the various possible decay modes of the Π_{DTC} into photons, quark pairs and lepton pairs for $N_{DTC} = 3$, $\Lambda_{DTC} = 1$ TeV at the (14a) 14 TeV HL-LHC, (14b) 27 TeV HE-LHC, and (14c) a 100 TeV collider.

$m_{\Pi_{DTC}}$ [GeV]	HL-LHC [14 TeV, 3 ab^{-1}]		HE-LHC [27 TeV, 15 ab^{-1}]		100 TeV, 30 ab^{-1}	
	500	1000	500	1000	500	1000
$\tau\tau$ [pb]	0.1	$8.2 \cdot 10^{-4}$	0.6	$5.1 \cdot 10^{-3}$	5.6	$8.2 \cdot 10^{-2}$
$\mu\mu$ [pb]	$4.6 \cdot 10^{-4}$	$2.9 \cdot 10^{-6}$	$1.9 \cdot 10^{-3}$	$1.8 \cdot 10^{-5}$	$2.0 \cdot 10^{-2}$	$2.9 \cdot 10^{-4}$
ee [pb]	$1.1 \cdot 10^{-8}$	$6.7 \cdot 10^{-11}$	$4.6 \cdot 10^{-8}$	$4.2 \cdot 10^{-10}$	$4.6 \cdot 10^{-7}$	$6.8 \cdot 10^{-9}$
$\gamma\gamma$ [pb]	0.5	$8.3 \cdot 10^{-4}$	2.2	$5.2 \cdot 10^{-3}$	22.6	$8.3 \cdot 10^{-2}$
$b\bar{b}$ [pb]	2.2	$1.4 \cdot 10^{-2}$	9.2	$8.5 \cdot 10^{-2}$	93	1.4
$t\bar{t}$ [pb]	2926	220	12421	139	$1.3 \cdot 10^5$	2213

Table 73: Benchmark points for Π_{DTC} production channels for high mass $m_{\Pi_{DTC}}$ at the 14 TeV HL-LHC, 27 TeV HE-LHC and a 100 TeV collider for $N_{DTC} = 3$, $\Lambda_{DTC} = 1$ TeV .

We show the benchmark predictions for the signatures of the DTC-pion for high and low-mass values at the HL-LHC, HE-LHC, and a future 100 TeV collider in tables 73-74.

m [GeV]	HL-LHC [14 TeV, 3 ab ⁻¹]		HE-LHC [27 TeV, 15 ab ⁻¹]		100 TeV, 30 ab ⁻¹	
	20	60	20	60	20	60
$\tau\tau$ [pb]	7287	189	13989	436	44255	1906
$\gamma\gamma$ [pb]	2.9	0.2	5.5	0.3	17	1.5

Table 74: Benchmark points for inclusive Π_{DTC} production channel at a 100TeV collider for low mass for $N_{\text{DTC}} = 3, \Lambda_{\text{DTC}} = 1$ TeV .

We observe that the mass of the TC-eta is $m_{\eta_{\text{TC}}} = 24.6$ TeV for $N_{\text{TC}} = 2, \Lambda_{\text{TC}} = 5.4$ TeV, which is out of the reach of the HL-LHC. The benchmark predictions of the signatures of the TC-eta and DTC-eta in various modes are given in tables 75-76 for the HL-LHC, HE-LHC, and a future 100 TeV collider. The benchmark points for the signatures of the DTC-Higgs are presented in table 77. In this scenario, the mass of the DTC-Higgs is 2002 GeV for $\Delta\chi_{\text{DTC}} \pm 2$ as $k_{\text{DTC}} = 0$. Furthermore, since the number of colours in DQCD and the mass of the DQCD-Higgs coincide with those for the case $\Lambda \approx \Lambda_{\text{DTC}}$ in the FN mechanism, as can be seen in tables 13 and 15, their collider signatures are identical and are shown in table 61.

$m_{\eta_{\text{TC,DTC}}}$ [GeV]	HL-LHC [14 TeV, 3 ab ⁻¹]	HE-LHC [27 TeV, 15 ab ⁻¹]	
	$N_{\text{DTC}} = 3, \Lambda_{\text{DTC}} = 1$ TeV 3724	$N_{\text{TC}} = 2, \Lambda_{\text{TC}} = 5.4$ TeV 24629	$N_{\text{DTC}} = 3, \Lambda_{\text{DTC}} = 1$ TeV 3724
$\tau\tau$ [pb]	$6.4 \cdot 10^{-9}$	$8.0 \cdot 10^{-23}$	$2.5 \cdot 10^{-7}$
$\mu\mu$ [pb]	$2.3 \cdot 10^{-11}$	$2.8 \cdot 10^{-25}$	$8.8 \cdot 10^{-10}$
ee [pb]	$5.3 \cdot 10^{-16}$	$6.6 \cdot 10^{-30}$	$2.1 \cdot 10^{-14}$
$\gamma\gamma$ [pb]	$5.6 \cdot 10^{-10}$	$2.4 \cdot 10^{-25}$	$2.2 \cdot 10^{-8}$
$b\bar{b}$ [pb]	$1.1 \cdot 10^{-7}$	$1.3 \cdot 10^{-21}$	$4.2 \cdot 10^{-6}$
$t\bar{t}$ [pb]	$1.8 \cdot 10^{-4}$	$2.3 \cdot 10^{-18}$	$7.1 \cdot 10^{-3}$

Table 75: Benchmark points for $\eta_{\text{TC,DTC}}$ production channels at the 14 TeV HL-LHC and the 27 TeV HE-LHC collider for $N_{\text{TC}} = 2, \Lambda_{\text{TC}} = 5.4$ TeV and $N_{\text{DTC}} = 3, \Lambda_{\text{DTC}} = 1$ TeV.

$m_{\eta_{\text{TC,DTC}}}$ [GeV]	$N_{\text{TC}} = 2, \Lambda_{\text{TC}} = 5.4$ TeV 24629	$N_{\text{DTC}} = 3, \Lambda_{\text{DTC}} = 1$ TeV 3724
	$\tau\tau$ [pb]	$2.0 \cdot 10^{-13}$
$\mu\mu$ [pb]	$7.1 \cdot 10^{-16}$	$7.2 \cdot 10^{-8}$
ee [pb]	$1.7 \cdot 10^{-20}$	$1.7 \cdot 10^{-13}$
$\gamma\gamma$ [pb]	$6.0 \cdot 10^{-16}$	$1.7 \cdot 10^{-6}$
$b\bar{b}$ [pb]	$3.3 \cdot 10^{-12}$	$3.3 \cdot 10^{-4}$
$t\bar{t}$ [pb]	$5.6 \cdot 10^{-9}$	0.6

Table 76: Benchmark points for $\eta_{\text{TC,DTC}}$ production channels at a 100 TeV collider for $N_{\text{TC}} = 2, \Lambda_{\text{TC}} = 5.4$ TeV and $N_{\text{DTC}} = 3, \Lambda_{\text{DTC}} = 1$ TeV.

$m_{H_{\text{DTC}}} [\text{GeV}]$	HL-LHC [14 TeV, 3 ab ⁻¹] 2002	HE-LHC [27 TeV, 15 ab ⁻¹] 2002	100 TeV, 30 ab ⁻¹ 2002
$\tau\tau$ [pb]	$7.4 \cdot 10^{-4}$	$8.3 \cdot 10^{-4}$	$4.7 \cdot 10^{-3}$
$\mu\mu$ [pb]	$2.6 \cdot 10^{-6}$	$2.9 \cdot 10^{-6}$	$1.7 \cdot 10^{-5}$
ee [pb]	$6.1 \cdot 10^{-11}$	$6.9 \cdot 10^{-11}$	$3.9 \cdot 10^{-10}$
$\gamma\gamma$ [pb]	$6.6 \cdot 10^{-4}$	$7.6 \cdot 10^{-5}$	$4.2 \cdot 10^{-3}$
$b\bar{b}$ [pb]	$1.2 \cdot 10^{-2}$	$1.4 \cdot 10^{-2}$	$7.8 \cdot 10^{-2}$
$t\bar{t}$ [pb]	18	21	116

Table 77: Benchmark points for H_{DTC} production channels at the 14 TeV HL-LHC, 27 TeV HE-LHC and the 100 TeV collider for $N_{\text{DTC}} = 3$, $\Lambda_{\text{DTC}} = 1$ TeV .

9 The FN mechanism dark-Higgs as 95.4 GeV excess

We observed from table 15 that the dark-Higgs H_{D} of the DQCD, corresponding to the FN mechanism , can be as low as 100 GeV. This fact can be used to address a low-mass diphoton excess at $m_{\gamma\gamma} = 95.4$ GeV observed by the CMS collaboration with a local significance of 2.9σ [67]. The ATLAS collaboration has also reported similar results with a local significance of 1.7σ [68]. The combined signal strength becomes [69],

$$\mu_{\gamma\gamma}^{\text{exp}} = \mu_{\gamma\gamma}^{\text{ATLAS+CMS}} = \frac{\sigma(pp \rightarrow \phi \rightarrow \gamma\gamma)}{\sigma_{\text{SM}}(pp \rightarrow h_{95.4}^{\text{SM}} \rightarrow \gamma\gamma)} = 0.24^{+0.09}_{-0.08}, \quad (159)$$

with the local significance of 3.1σ , where ϕ is a non-SM scalar with a mass of 95.4 GeV, and the scalar $h_{95.4}^{\text{SM}}$ stands for a SM-like Higgs with the same mass. There are several proposals to address this observation [69]-[126].

To explain this excess, we assume that the dark-Higgs H_{D} dominantly couples to the top-quark, and coupling to other SM fermions are $\lambda_f = 1$. We vary the coupling λ_t in the range $1 - 4\pi$. In figure 15, we show the allowed parameter space in red colour that can accommodate the 95.4 GeV excess.

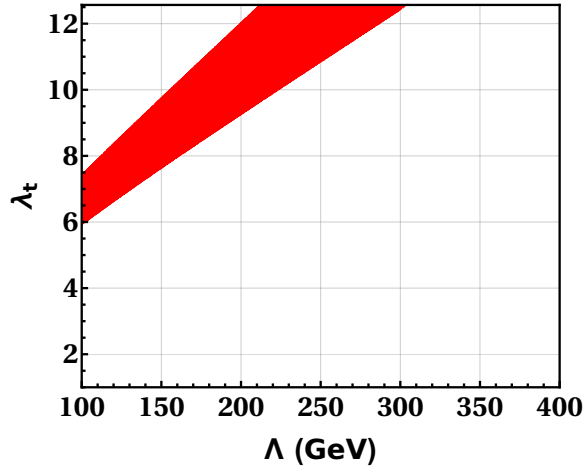


Figure 15: Allowed region (red) of dimensionless coupling λ_t and the scale Λ for which the dark-Higgs H_{D} of the FN mechanism accounts for the observed di-photon excess at $m_{\gamma\gamma} = 95.4$ GeV.

10 The chirality-dependent dark matter

When the SHVM is accommodated within the DTC paradigm, we observe from table 9-11, that the dark-Higgs H_D corresponding to DQCD may be very light due to chiral suppression caused by the proportionality factor k_D for the case when the chirality $\Delta\chi_D$ is negative. Thus, it may be possible that it becomes a novel chirality-dependent dark-matter. The mass of the dark-Higgs is given by,

$$M_{H_D} = 2M_{\text{dyn},D} \exp(k_D \Delta\chi_D), \quad (160)$$

where $M_{\text{dyn},D} \approx \Lambda$ is assumed.

We assume that the mass of the dark Higgs is $m_{H_D} < 2m_e$ such that it does not decay to a pair of electrons and positrons. Moreover, the decays of the dark-Higgs $H_D \rightarrow \gamma\gamma$ and $H_D \rightarrow \nu\nu$ limit the scale Λ and the mass of the dark-Higgs m_{H_D} . Thus, there are two allowed mass ranges where the dark-Higgs may act like a dark-matter particle:

1. For $m_{H_D} > 2m_\nu$, which requires at least $\Delta\chi_D = -6$.
2. In the mass range $m_{H_D} < 2m_\nu$ such that decay $H_D \rightarrow \nu\nu$ is kinematically forbidden allowing the scale Λ to be as low as the electroweak scale.

For both scenarios, the decays of the dark-Higgs to two photons should be highly suppressed. Moreover, we shall use the lower bound on the mass of dark-matter to be 10^{-19} eV, as reported in reference [127].

We notice that the dark-Higgs H_D may become a dark-matter particle through the misalignment mechanism [128, 129, 130]. This mechanism relies on the assumption that a scalar field may have a random initial state in the early universe, causing a misalignment when the field acquires a true vacuum after inflation. The cold dark-matter density of the coherent oscillation is produced when the Hubble expansion rate becomes less than the mass of the dark-Higgs H_D . The equation of motion of the dark-Higgs H_D in the expanding universe is,

$$\ddot{H}_D + 3H\dot{H}_D + m_{H_D}^2 H_D \approx 0. \quad (161)$$

This equation can be solved in two scenarios. The first scenario contains an epoch when $3H \gg m_{H_D}$ such that the oscillations of the field H_D are overdamped and frozen, leading to $\dot{H}_D = 0$. At a later time t_1 , defined by $3H(t_1) = m_{H_D}(t_1) \equiv m_1$, after inflation, the field rolls down to true vacuum, and begins to oscillate. For this scenario, the solution is given by [131],

$$H_D \simeq H_D^0 \left(\frac{m_1 a_1^3}{m_{H_D} a^3} \right)^{1/2}, \quad (162)$$

where H_D^0 is the initial value of the dark-Higgs field H_D upto the time t_1 .

This equation can be used to derive an upper bound on the present dark matter density, which is [131],

$$\rho_{H_D,0} < 1.17 \frac{\text{keV}}{\text{cm}^3} \times \frac{m_{H_D}}{\text{eV}} \left(\frac{H_D^0}{53\text{TeV}} \right)^2, \quad (163)$$

leading to the inequality

$$\frac{m_{H_D}}{\text{eV}} \left(\frac{H_D^0}{53\text{TeV}} \right)^2 > 1 \quad (164)$$

for the field H_D to act like a dark-matter candidate.

As discussed earlier, we assume that the decay rates $H_D \rightarrow \nu\bar{\nu}, \gamma\gamma$ are highly suppressed and are such that $\Gamma(H_D \rightarrow \nu\bar{\nu}, \gamma\gamma) < 10^{-50}$ GeV. We show the allowed parameter space, denoted by light-blue region, for the scenario $m_{H_D} > 2m_\nu$ in figure 16a where the dark Higgs can act like a dark matter candidate. The same is shown for the scenario $m_{H_D} < 2m_\nu$ in figure 16b. For $\Delta\chi_D = -6$, the proportionality factor k_D becomes $k_D = 6.5$ for the scenario $m_{H_D} < 2m_\nu$.

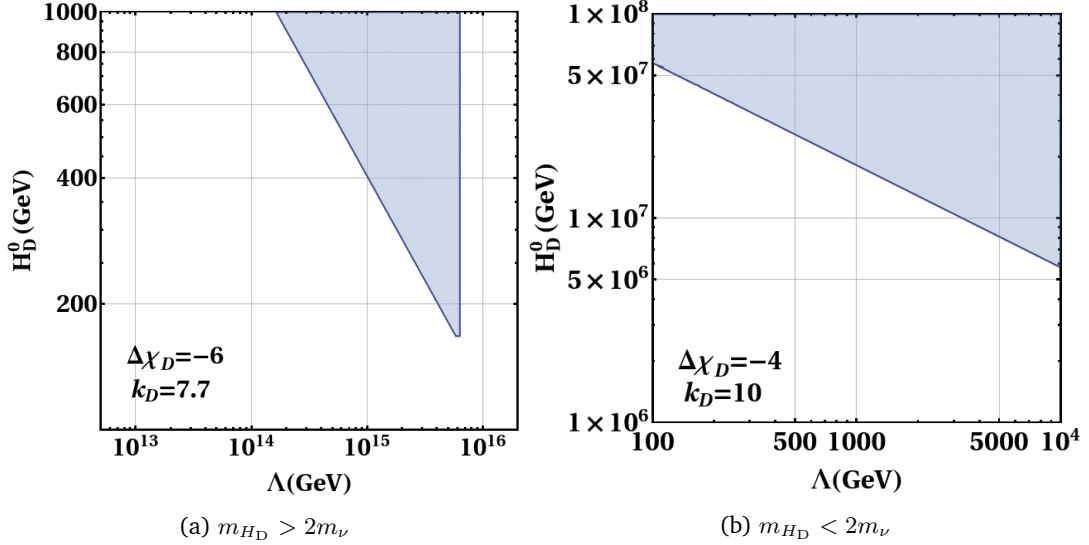


Figure 16: The parameter space, denoted by light-blue region, allowed by equation 164 and $\Gamma(H_D \rightarrow \nu\bar{\nu}, \gamma\gamma) < 10^{-50}$ GeV where the dark-Higgs H_D can play the role of the chirality dependent dark-matter.

From a phenomenological perspective, the scenario $m_{H_D} < 2m_\nu$ may be interesting due to the low values of the scale Λ . The signatures of the chirality-dependent dark-matter may emerge, for instance, via the Higgs portal through the term $\varphi^\dagger \varphi H_D^2$. However, this investigation is beyond the scope of this paper.

11 Summary

QCD-like TC models were invented to provide an elegant mechanism for the electroweak symmetry breaking, and provide a natural origin of mass through chiral symmetry breaking. However, QCD-like TC models failed to produce the fermionic mass spectrum of the SM. This happens because the FCNCs interactions push the ETC scale to 10^6 GeV, causing extreme suppression of all fermionic masses, and making them completely unrealistic. Moreover, QCD-like TC models predict a heavy mass of the Higgs boson, and are incompatible with the electroweak precision observables. Furthermore, in models based on strong dynamics, such as QCD-like TC models or walking-TC models, explaining the fermionic mass spectrum of the SM is a challenge. The usual approach assumes successive hierarchical breaking of a very large non-Abelian symmetry, resulting in hierarchical scales attributed to masses of different SM fermions. The implementation of this assumption is practically challenging, and a complete solution to the flavour problem defined by fermionic masses and their mixing is difficult to achieve.

In this work, we have discussed a dark-technicolour model, which is based on QCD-like dynamics. The SHVM and the FN mechanisms can both be accommodated in this framework. Thus, the DTC paradigm is capable of providing a complete solution of the flavour problem without introducing the assumption of the successive hierarchical breaking of a very large non-Abelian symmetry. Moreover, the DTC paradigm can produce the SM Higgs mass by exploiting the EMAC hypothesis. The incompatibility with the electroweak precision observables is overcome by having a very heavy TC-vector meson allowed by the EMAC mechanism.

From the phenomenological perspective, we present collider signatures of the DTC paradigm in the scenario, where the SHVM is accommodated within its framework, as well as, in the scenario where the FN mechanism is implemented within the DTC paradigm. Both scenarios can be differentiated through inclusive decay modes such as $\gamma\gamma$ and $t\bar{t}$ of the TC, DTC, and DQCD dynamics. Several of these inclusive channels are accessible at the HL-LHC in different mass ranges. Moreover, a detailed study of the collider signatures of the DTC paradigm is also presented for the HE-LHC and a 100 TeV future hadron collider.

In addition to a comprehensive collider investigation, we also show that the dark-Higgs of the DQCD-dynamics, corresponding to the scenario where the FN mechanism is implemented within the framework of

the DTC paradigm, can address the 95.4 GeV excess reported by the ATLAS and CMS experiment. Furthermore, the dark-Higgs emerging through the DQCD-dynamics, when the SHVM is accommodated within the DTC paradigm, becomes very light for the negative chirality, and can provide a new class of chirality dependent dark matter particles.

Acknowledgement

This work is supported by the Council of Science and Technology, Govt. of Uttar Pradesh, India through the project "A new paradigm for flavour problem" no. CST/D-1301, and Anusandhan National Research Foundation (SERB), Department of Science and Technology, Government of India through the project "Higgs Physics within and beyond the Standard Model" no. CRG/2022/003237.

Appendix

Outline of a possible extended technicolour and extended dark-technicolour

In this appendix, we present an outline of a possible extended and dark-extended technicolour scenario as discussed in reference [17]. For ETC model, the TC fermions, left-handed SM fermions, and F_R fermions are accommodated in an $SU(N_{TC} + 12)$ symmetry in the following way:

$$\psi_L^{\text{ETC}} \equiv \begin{pmatrix} T & B \\ T & B \\ T & B \\ \dots \\ \dots \\ T & B \\ u & d \\ u & d \\ u & d \\ \nu_e & e \\ c & s \\ c & s \\ c & s \\ \nu_\mu & \mu \\ t & b \\ t & b \\ t & b \\ \nu_\tau & \tau \end{pmatrix}_L, \psi_R^{\text{ETC}} \equiv \begin{pmatrix} T \\ T \\ \dots \\ \dots \\ T \\ U^1 \\ U^1 \\ U^1 \\ N^1 \\ U^2 \\ U^2 \\ U^2 \\ N^2 \\ U^3 \\ U^3 \\ U^3 \\ N^3 \end{pmatrix}_R, \psi_R^{\text{ETC}} \equiv \begin{pmatrix} B \\ B \\ B \\ \dots \\ \dots \\ B \\ D^1 \\ D^1 \\ D^1 \\ E^1 \\ D^2 \\ D^2 \\ D^2 \\ E^2 \\ D^3 \\ D^3 \\ D^3 \\ E^3 \end{pmatrix}_R. \quad (165)$$

The group $SU(N_{DTC} + 1)$ defines the EDTC where the first family quark-multiplet is given by:

$$\psi_{L,i}^{\text{EDTC,q}} \equiv \begin{pmatrix} c_i & c_i & c_i & c_i & \dots & U^i \\ s_i & s_i & s_i & s_i & \dots & D^i \end{pmatrix}_L, \psi_R^{\text{EDTC,q}} \equiv \begin{pmatrix} c_i & c_i & c_i & c_i & \dots & f_u \\ s_i & s_i & s_i & s_i & \dots & f_d \end{pmatrix}_R, \quad (166)$$

where $i = 1, 2, 3, \dots$ show the number of generations, and $f_u = u, c, t$ and $f_d = d, s, b$ stand for the right-handed quark SM fields.

The leptonic multiplet can be defined in a similar manner as,

$$\psi_{L,i}^{\text{EDTC,\ell}} \equiv \begin{pmatrix} e_i & e_i & e_i & e_i & \dots & N^i \\ n_i & n_i & n_i & n_i & \dots & E^i \end{pmatrix}_L, \psi_{R,i}^{\text{EDTC,\ell}} \equiv \begin{pmatrix} e_i & e_i & e_i & e_i & \dots & f_\nu \\ n_i & n_i & n_i & n_i & \dots & f_e \end{pmatrix}_R, \quad (167)$$

where $f_\nu = \nu_e, \nu_\mu, \nu_\tau$ and $f_e = e, \mu, \tau$ denote the right-handed leptonic SM fields.

We assume that ETC and DETC are further accommodated in GUT symmetry \mathcal{G}_{GUT} , which is broken as,

$$\mathcal{G}_{\text{GUT}} \rightarrow SU(N_{TC} + 12) \times SU(N_D) \times SU(N_{DTC} + 1) \rightarrow SU(3)_c \times SU(N_{TC}) \times SU(N_D) \times SU(N_{DTC}). \quad (168)$$

References

- [1] V. L. Ginzburg and L. D. Landau, Zh. Eksp. Teor. Fiz. **20**, 1064-1082 (1950) doi:10.1016/b978-0-08-010586-4.50078-x
- [2] J. Bardeen, L. N. Cooper and J. R. Schrieffer, Phys. Rev. **106**, 162 (1957) doi:10.1103/PhysRev.106.162
- [3] J. Bardeen, L. N. Cooper and J. R. Schrieffer, Phys. Rev. **108**, 1175-1204 (1957) doi:10.1103/PhysRev.108.1175
- [4] M. Gell-Mann and M. Levy, Nuovo Cim. **16**, 705 (1960) doi:10.1007/BF02859738
- [5] Y. Nambu and G. Jona-Lasinio, Phys. Rev. **122**, 345-358 (1961) doi:10.1103/PhysRev.122.345
- [6] Y. Nambu and G. Jona-Lasinio, Phys. Rev. **124**, 246-254 (1961) doi:10.1103/PhysRev.124.246
- [7] S. Weinberg, Phys. Rev. D **13**, 974-996 (1976) doi:10.1103/PhysRevD.19.1277
- [8] L. Susskind, Phys. Rev. D **20**, 2619-2625 (1979) doi:10.1103/PhysRevD.20.2619
- [9] C. T. Hill and E. H. Simmons, Phys. Rept. **381**, 235-402 (2003) [erratum: Phys. Rept. **390**, 553-554 (2004)] doi:10.1016/S0370-1573(03)00140-6 [arXiv:hep-ph/0203079 [hep-ph]].
- [10] B. Holdom, Phys. Rev. D **24**, 1441 (1981)
- [11] B. Holdom, Phys. Lett. **150B** (1985) 301;
- [12] T. Appelquist and L. C. R. Wijewardhana, Phys. Rev. D **35** (1987) 774.
- [13] T. W. Appelquist, D. Karabali and L. C. R. Wijewardhana, Phys. Rev. Lett. **57**, 957 (1986) doi:10.1103/PhysRevLett.57.957
- [14] T. Appelquist and L. C. R. Wijewardhana, Phys. Rev. D **36**, 568 (1987) doi:10.1103/PhysRevD.36.568
- [15] K. Yamawaki, M. Bando and K. i. Matumoto, Phys. Rev. Lett. **56**, 1335 (1986) doi:10.1103/PhysRevLett.56.1335
- [16] T. Akiba and T. Yanagida, Phys. Lett. B **169**, 432-435 (1986) doi:10.1016/0370-2693(86)90385-0
- [17] G. Abbas, R. Adhikari, E. J. Chun and N. Singh, Eur. Phys. J. Plus **140**, no.1, 73 (2025) doi:10.1140/epjp/s13360-025-06008-6 [arXiv:2308.14811 [hep-ph]].
- [18] G. Abbas, doi:10.31526/ACP.BSM-2023.3 [arXiv:2404.03232 [hep-ph]].
- [19] G. Abbas, Int. J. Mod. Phys. A **37**, no.11n12, 2250056 (2022) doi:10.1142/S0217751X22500567 [arXiv:2012.11283 [hep-ph]].
- [20] K. I. Aoki and M. Bando, Phys. Lett. B **126**, 101-105 (1983) doi:10.1016/0370-2693(83)90027-8
- [21] K. I. Aoki and M. Bando, Prog. Theor. Phys. **70**, 259 (1983) doi:10.1143/PTP.70.259
- [22] K. I. Aoki and M. Bando, Prog. Theor. Phys. **70**, 272 (1983) doi:10.1143/PTP.70.272
- [23] G. Abbas, Int. J. Mod. Phys. A **34**, no.20, 1950104 (2019) doi:10.1142/S0217751X19501045 [arXiv:1712.08052 [hep-ph]].
- [24] G. Abbas, Modern Physics Letters A **40** (2025) 2550056 [arXiv:2310.12915 [hep-ph]]. DOI: 10.1142/S0217732325500567
- [25] C. D. Froggatt and H. B. Nielsen, Nucl. Phys. B **147**, 277 (1979). doi:10.1016/0550-3213(79)90316-X

- [26] G. Abbas, *Int. J. Mod. Phys. A* **36**, 2150090 (2021) doi:10.1142/S0217751X21500901 [arXiv:1807.05683 [hep-ph]].
- [27] A. Abada *et al.* [FCC], *Eur. Phys. J. ST* **228**, no.5, 1109-1382 (2019) doi:10.1140/epjst/e2019-900088-6
- [28] A. Abada *et al.* [FCC], *Eur. Phys. J. C* **79**, no.6, 474 (2019) doi:10.1140/epjc/s10052-019-6904-3
- [29] H. Harari and N. Seiberg, *Phys. Lett. B* **102**, 263-266 (1981) doi:10.1016/0370-2693(81)90871-6
- [30] S. Raby, S. Dimopoulos and L. Susskind, *Nucl. Phys. B* **169**, 373-383 (1980) doi:10.1016/0550-3213(80)90093-0
- [31] G. Abbas and N. Singh, [arXiv:2412.08523 [hep-ph]].
- [32] V. A. Miransky,
- [33] Z. z. Xing, H. Zhang and S. Zhou, *Phys. Rev. D* **77**, 113016 (2008) doi:10.1103/PhysRevD.77.113016 [arXiv:0712.1419 [hep-ph]].
- [34] P.A. Zyla *et al.* (Particle Data Group), *Prog. Theor. Exp. Phys.* 2020, 083C01 (2020) and 2021 update
- [35] P. F. de Salas, D. V. Forero, S. Gariazzo, P. Martínez-Miravé, O. Mena, C. A. Ternes, M. Tórtola and J. W. F. Valle, *JHEP* **02** (2021), 071 doi:10.1007/JHEP02(2021)071 [arXiv:2006.11237 [hep-ph]].
- [36] G. Abbas, V. Singh, N. Singh and R. Sain, *Eur. Phys. J. C* **83**, no.4, 305 (2023) doi:10.1140/epjc/s10052-023-11471-5 [arXiv:2208.03733 [hep-ph]].
- [37] G. Abbas, R. Adhikari and E. J. Chun, [arXiv:2303.10125 [hep-ph]].
- [38] G. Abbas, A. K. Alok, N. R. S. Chundawat, N. Khan and N. Singh, *Phys. Rev. D* **110**, no.11, 115015 (2024) doi:10.1103/PhysRevD.110.115015 [arXiv:2407.09255 [hep-ph]].
- [39] R. Delbourgo and M. D. Scadron, *Phys. Rev. Lett.* **48**, 379 (1982).
- [40] S. Navas *et al.* (Particle Data Group), *Phys. Rev. D* 110, 030001 (2024)
- [41] V. Elias and M. D. Scadron, *Phys. Rev. Lett.* **53**, 1129 (1984) doi:10.1103/PhysRevLett.53.1129
- [42] ATLAS Collaboration, *Phys. Lett. B* **716**, 1 (2012).
- [43] CMS Collaboration, *Phys. Lett. B* **716**, 30 (2012).
- [44] M. E. Peskin and T. Takeuchi, *Phys. Rev. Lett.* **65**, 964-967 (1990) doi:10.1103/PhysRevLett.65.964
- [45] M. E. Peskin and T. Takeuchi, *Phys. Rev. D* **46**, 381-409 (1992) doi:10.1103/PhysRevD.46.381
- [46] A. Pich, I. Rosell and J. J. Sanz-Cillero, [arXiv:2503.05917 [hep-ph]].
- [47] A. Pich, I. Rosell and J. J. Sanz-Cillero, *JHEP* **01**, 157 (2014) doi:10.1007/JHEP01(2014)157 [arXiv:1310.3121 [hep-ph]].
- [48] G. 't Hooft, *Nucl. Phys. B* **72**, 461 (1974) doi:10.1016/0550-3213(74)90154-0
- [49] E. Witten, *Nucl. Phys. B* **160**, 57-115 (1979) doi:10.1016/0550-3213(79)90232-3
- [50] J. Tandean, *Phys. Rev. D* **52** (1995), 1398-1403 doi:10.1103/PhysRevD.52.1398 [arXiv:hep-ph/9505256 [hep-ph]].
- [51] S. Bethke, *Nucl. Phys. B Proc. Suppl.* **234**, 229-234 (2013) doi:10.1016/j.nuclphysbps.2012.12.020 [arXiv:1210.0325 [hep-ex]].
- [52] A. M. Sirunyan *et al.* [CMS], *JHEP* **06** (2018), 127 [erratum: *JHEP* **03** (2019), 128] doi:10.1007/JHEP06(2018)127 [arXiv:1804.01939 [hep-ex]].

- [53] G. Aad *et al.* [ATLAS], JHEP **07**, 200 (2023) doi:10.1007/JHEP07(2023)200 [arXiv:2211.02617 [hep-ex]].
- [54] A. M. Sirunyan *et al.* [CMS], JHEP **03**, 034 (2020) doi:10.1007/JHEP03(2020)034 [arXiv:1912.01594 [hep-ex]].
- [55] G. Aad *et al.* [ATLAS], Phys. Lett. B **822**, 136651 (2021) doi:10.1016/j.physletb.2021.136651 [arXiv:2102.13405 [hep-ex]].
- [56] A. M. Sirunyan *et al.* [CMS], Phys. Rev. D **98** (2018) no.9, 092001 doi:10.1103/PhysRevD.98.092001 [arXiv:1809.00327 [hep-ex]].
- [57] <https://indico.cern.ch/event/284800/contributions/1635340/attachments/527023/726700/collider-reach.pdf>
- [58] M. Aaboud *et al.* [ATLAS], JHEP **01**, 055 (2018) doi:10.1007/JHEP01(2018)055 [arXiv:1709.07242 [hep-ex]].
- [59] A. M. Sirunyan *et al.* [CMS], JHEP **09** (2018), 007 doi:10.1007/JHEP09(2018)007 [arXiv:1803.06553 [hep-ex]].
- [60] G. Aad *et al.* [ATLAS], Phys. Lett. B **796** (2019), 68-87 doi:10.1016/j.physletb.2019.07.016 [arXiv:1903.06248 [hep-ex]].
- [61] A. M. Sirunyan *et al.* [CMS], JHEP **07** (2021), 208 doi:10.1007/JHEP07(2021)208 [arXiv:2103.02708 [hep-ex]].
- [62] M. Aaboud *et al.* [ATLAS], Phys. Rev. D **99** (2019) no.9, 092004 doi:10.1103/PhysRevD.99.092004 [arXiv:1902.10077 [hep-ex]].
- [63] G. Aad *et al.* [ATLAS], JHEP **10** (2020), 061 doi:10.1007/JHEP10(2020)061 [arXiv:2005.05138 [hep-ex]].
- [64] A. M. Sirunyan *et al.* [CMS], JHEP **04** (2019), 031 doi:10.1007/JHEP04(2019)031 [arXiv:1810.05905 [hep-ex]].
- [65] G. Arcadi, G. Busoni, D. Cabo-Almeida and N. Krishnan, Phys. Rev. D **110** (2024) no.11, 11 doi:10.1103/PhysRevD.110.115028 [arXiv:2311.14486 [hep-ph]].
- [66] A. D. Martin, W. J. Stirling, R. S. Thorne and G. Watt, Eur. Phys. J. C **63**, 189-285 (2009) doi:10.1140/epjc/s10052-009-1072-5 [arXiv:0901.0002 [hep-ph]].
- [67] CMS collaboration, “Search for a standard model-like Higgs boson in the mass range between 70 and 110 GeV in the diphoton final state in proton-proton collisions at $\sqrt{s} = 13$ TeV,” CMS-PAS-HIG-20-002, 2023.
- [68] C. Arcangeletti. on behalf of ATLAS collaboration, LHC Seminar https://indico.cern.ch/event/1281604/attachments/2660420/4608571/LHCSeminarArcangeletti_final.pdf, 7th of June, 2023.
- [69] T. Biekötter, S. Heinemeyer and G. Weiglein, “95.4 GeV diphoton excess at ATLAS and CMS,” Phys. Rev. D **109** (2024), 3.
- [70] R. Barate *et al.* [LEP Working Group for Higgs boson searches, ALEPH, DELPHI, L3 and OPAL], “Search for the standard model Higgs boson at LEP,” Phys. Lett. B **565** (2003), 61-75.
- [71] J. Cao, X. Guo, Y. He, P. Wu and Y. Zhang, “Diphoton signal of the light Higgs boson in natural NMSSM,” Phys. Rev. D **95** (2017), 116001.
- [72] T. Biekötter, M. Chakraborti and S. Heinemeyer, “A 96 GeV Higgs boson in the N2HDM,” Eur. Phys. J. C **80** (2020), 2.

- [73] S. Heinemeyer, C. Li, F. Lika, G. Moortgat-Pick and S. Paasch, “Phenomenology of a 96 GeV Higgs boson in the 2HDM with an additional singlet,” *Phys. Rev. D* **106** (2022), 075003.
- [74] T. Biekötter, S. Heinemeyer and G. Weiglein, “Mounting evidence for a 95 GeV Higgs boson,” *JHEP* **08** (2022), 201.
- [75] J. A. Aguilar-Saavedra, H. B. Câmara, F. R. Joaquim and J. F. Seabra, “Confronting the 95 GeV excesses within the $U(1)$ -extended next-to-minimal 2HDM,” *Phys. Rev. D* **108** (2023), 075020.
- [76] K. Choi, S. H. Im, K. S. Jeong and C. B. Park, “Light Higgs bosons in the general NMSSM,” *Eur. Phys. J. C* **79** (2019), 956.
- [77] S. Ma, K. Wang and J. Zhu, “Higgs decay to light (pseudo)scalars in the semi-constrained NMSSM,” *Chin. Phys. C* **45** (2021), 023113.
- [78] W. Li, H. Qiao and J. Zhu, “Light Higgs boson in the NMSSM confronted with the CMS di-photon and di-tau excesses,” *Chin. Phys. C* **47** (2023), 123102.
- [79] U. Ellwanger and C. Hugonie, “Additional Higgs Bosons near 95 and 650 GeV in the NMSSM,” *Eur. Phys. J. C* **83** (2023), 1138.
- [80] P. S. B. Dev, R. N. Mohapatra and Y. Zhang, “Explanation of the 95 GeV $\gamma\gamma$ and $b\bar{b}$ excesses in the minimal left-right symmetric model,” *Phys. Lett. B* **849** (2024), 138481.
- [81] C. Bonilla, A. E. Carcamo Hernandez, S. Kovalenko, H. Lee, R. Pasechnik and I. Schmidt, “Fermion mass hierarchy in an extended left-right symmetric model,” *JHEP* **12** (2023), 075.
- [82] C. X. Liu, Y. Zhou, X. Y. Zheng, J. Ma, T. F. Feng and H. B. Zhang, “95 GeV excess in a CP-violating μ -from- ν SSM,” *Phys. Rev. D* **109** (2024), 056001.
- [83] W. Li, H. Qiao, K. Wang and J. Zhu, “Light dark matter confronted with the 95 GeV diphoton excess,” *arXiv:2312.17599*.
- [84] A. Ahriche, M. L. Bellilet, M. O. Khojali, M. Kumar and A. T. Mulaudzi, “The scale invariant scotogenic model: CDF-II W -boson mass and the 95 GeV excesses,” *arXiv:2311.08297*.
- [85] J. Cao, X. Jia, J. Lian and L. Meng, “95 GeV diphoton and $b\bar{b}$ excesses in the general next-to-minimal supersymmetric standard model,” *Phys. Rev. D* **109** (2024), 075001.
- [86] M. Maniatis and O. Nachtmann, “CMS results for the $\gamma\gamma$ production at the LHC: do they give a hint for a Higgs boson of the maximally CP symmetric two-Higgs-doublet model?,” *arXiv:2309.04869*.
- [87] A. Belyaev, R. Benbrik, M. Boukidi, M. Chakraborti, S. Moretti and S. Semlali, “Explanation of the hints for a 95 GeV Higgs boson within a 2-Higgs Doublet Model,” *JHEP* **05** (2024), 209.
- [88] D. Azevedo, T. Biekötter and P. M. Ferreira, “2HDM interpretations of the CMS diphoton excess at 95 GeV,” *JHEP* **11** (2023), 017.
- [89] D. Bhatia, N. Desai and S. Dwivedi, “Discovery prospects of a light charged Higgs near the fermiophobic region of Type-I 2HDM,” *JHEP* **06** (2023), 100.
- [90] T. K. Chen, C. W. Chiang, S. Heinemeyer and G. Weiglein, “95 GeV Higgs boson in the Georgi-Machacek model,” *Phys. Rev. D* **109** (2024), 075043.
- [91] A. Ahriche, “The 95 GeV Excess in the Georgi-Machacek Model: Single or Twin Peak Resonance,” *arXiv:2312.10484*.
- [92] D. Borah, S. Mahapatra, P. K. Paul and N. Sahu, “Scotogenic $U(1)_{L\mu-L\tau}$ origin of $(g-2)_\mu$, W -mass anomaly and 95 GeV excess,” *Phys. Rev. D* **109** (2024), 055021.

- [93] S. Banik, G. Coloretti, A. Crivellin and B. Mellado, “Uncovering New Higgses in the LHC Analyses of Differential $t\bar{t}$ Cross Sections,” arXiv:2308.07953.
- [94] J. Dutta, J. Lahiri, C. Li, G. Moortgat-Pick, S. F. Tabira and J. A. Ziegler, “Dark Matter Phenomenology in 2HDMs in light of the 95 GeV excess,” arXiv:2308.05653.
- [95] S. Bhattacharya, G. Coloretti, A. Crivellin, S. E. Dahbi, Y. Fang, M. Kumar and B. Mellado, “Growing Excesses of New Scalars at the Electroweak Scale,” arXiv:2306.17209.
- [96] S. Ashanujjaman, S. Banik, G. Coloretti, A. Crivellin, B. Mellado and A. T. Mulaudzi, “SU(2)_L triplet scalar as the origin of the 95 GeV excess?,” Phys. Rev. D **108** (2023), L091704.
- [97] P. Escribano, V. M. Lozano and A. Vicente, “Scotogenic explanation for the 95 GeV excesses,” Phys. Rev. D **108** (2023), 115001.
- [98] T. Biekötter, S. Heinemeyer and G. Weiglein, “The CMS di-photon excess at 95 GeV in view of the LHC Run 2 results,” Phys. Lett. B **846** (2023), 138217.
- [99] S. Banik, A. Crivellin, S. Iguro and T. Kitahara, “Asymmetric di-Higgs signals of the next-to-minimal 2HDM with a U(1) symmetry,” Phys. Rev. D **108** (2023), 075011.
- [100] G. Coloretti, A. Crivellin, S. Bhattacharya and B. Mellado, “Searching for low-mass resonances decaying into W bosons,” Phys. Rev. D **108** (2023), 035026.
- [101] A. Ahriche, “Constraining the Georgi-Machacek model with a light Higgs boson,” Phys. Rev. D **107** (2023), 015006.
- [102] R. Benbrik, M. Boukidi, S. Moretti and S. Semlali, “Explaining the 96 GeV Di-photon anomaly in a generic 2HDM Type-III,” Phys. Lett. B **832** (2022), 137245.
- [103] T. Biekötter, S. Heinemeyer and G. Weiglein, “Excesses in the low-mass Higgs-boson search and the W-boson mass measurement,” Eur. Phys. J. C **83** (2023), 450.
- [104] T. Biekötter, A. Grohsjean, S. Heinemeyer, C. Schwanenberger and G. Weiglein, “Possible indications for new Higgs bosons in the reach of the LHC: N2HDM and NMSSM interpretations,” Eur. Phys. J. C **82** (2022), 178.
- [105] A. A. Abdelalim, B. Das, S. Khalil and S. Moretti, “Di-photon decay of a light Higgs state in the BLSSM,” Nucl. Phys. B **985** (2022), 116013.
- [106] T. Biekötter, M. Chakraborti and S. Heinemeyer, “The “96 GeV excess” at the LHC,” Int. J. Mod. Phys. A **36** (2021), 2142018.
- [107] J. A. Aguilar-Saavedra and F. R. Joaquim, “Multiphoton signals of a (96 GeV?) stealth boson,” Eur. Phys. J. C **80** (2020), 403.
- [108] J. Cao, X. Jia, Y. Yue, H. Zhou and P. Zhu, “96 GeV diphoton excess in seesaw extensions of the natural NMSSM,” Phys. Rev. D **101** (2020), 055008.
- [109] A. Kundu, S. Maharana and P. Mondal, “A 96 GeV scalar tagged to dark matter models,” Nucl. Phys. B **955** (2020), 115057.
- [110] J. Cao, X. Jia and J. Lian, “Unified Interpretation of Muon g-2 anomaly, 95 GeV Diphoton, and $b\bar{b}$ Excesses in the General Next-to-Minimal Supersymmetric Standard Model,” arXiv:2402.15847.
- [111] J. Kalinowski and W. Kotlarski, “Interpreting 95 GeV di-photon/ $b\bar{b}$ excesses as a lightest Higgs boson of the MRSSM,” JHEP **07** (2024), 037.
- [112] U. Ellwanger, C. Hugonie, S. F. King and S. Moretti, “NMSSM Explanation for Excesses in the Search for Neutralinos and Charginos and a 95 GeV Higgs Boson,” arXiv:2404.19338.

- [113] R. Benbrik, M. Boukidi and S. Moretti, “Superposition of CP-Even and CP-Odd Higgs Resonances: Explaining the 95 GeV Excesses within a Two-Higgs Doublet Model,” arXiv:2405.02899.
- [114] J. Lian, “The 95GeV Excesses in the \mathbb{Z}_3 -symmetric Next-to Minimal Supersymmetric Standard Model,” arXiv:2406.10969.
- [115] J. L. Yang, M. H. Guo, W. H. Zhang, H. B. Zhang and T. F. Feng, “Explaining the possible 95 GeV excesses in the $B - L$ symmetric SSM,” arXiv:2406.01926.
- [116] K. Wang and J. Zhu, Chin. Phys. C **48**, no.7, 073105 (2024) doi:10.1088/1674-1137/ad4268 [arXiv:2402.11232 [hep-ph]].
- [117] J. Gao, J. Ma, L. Wang and H. Xu, [arXiv:2408.03705 [hep-ph]].
- [118] S. Yaser Ayazi, M. Hosseini, S. Paktinat Mehdiabadi and R. Rouzbehi, Phys. Rev. D **110**, no.5, 055004 (2024) doi:10.1103/PhysRevD.110.055004 [arXiv:2405.01132 [hep-ph]].
- [119] A. Khanna, S. Moretti and A. Sarkar, [arXiv:2409.02587 [hep-ph]].
- [120] B. Ait-Ouazghour, M. Chabab and K. Goure, [arXiv:2410.11140 [hep-ph]].
- [121] S. Baek, P. Ko, Y. Omura and C. Yu, [arXiv:2412.02178 [hep-ph]].
- [122] S. Banik, G. Coloretti, A. Crivellin and H. E. Haber, [arXiv:2412.00523 [hep-ph]].
- [123] T. Mondal, S. Moretti and P. Sanyal, [arXiv:2412.00474 [hep-ph]].
- [124] S. Gao, S. M. Zhao, L. Ruan, X. X. Dong and T. F. Feng, [arXiv:2411.13261 [hep-ph]].
- [125] A. Arhrib, K. H. Phan, V. Q. Tran and T. C. Yuan, [arXiv:2405.03127 [hep-ph]].
- [126] X. Du, H. Liu and Q. Chang, [arXiv:2502.06444 [hep-ph]].
- [127] M. A. Amin and M. Mirbabayi, Phys. Rev. Lett. **132**, no.22, 221004 (2024) doi:10.1103/PhysRevLett.132.221004 [arXiv:2211.09775 [hep-ph]].
- [128] J. Preskill, M. B. Wise and F. Wilczek, Phys. Lett. B **120**, 127-132 (1983) doi:10.1016/0370-2693(83)90637-8
- [129] L. F. Abbott and P. Sikivie, Phys. Lett. B **120**, 133-136 (1983) doi:10.1016/0370-2693(83)90638-X
- [130] M. Dine and W. Fischler, Phys. Lett. B **120**, 137-141 (1983) doi:10.1016/0370-2693(83)90639-1
- [131] P. Arias, D. Cadamuro, M. Goodsell, J. Jaeckel, J. Redondo and A. Ringwald, JCAP **06**, 013 (2012) doi:10.1088/1475-7516/2012/06/013 [arXiv:1201.5902 [hep-ph]].